Doctoral theses at NTNU, 2023:9

Magnus Kyrkjebø Vinnes

The actuator disk as a wind turbine model: An experimental assessment of the fluid dynamics

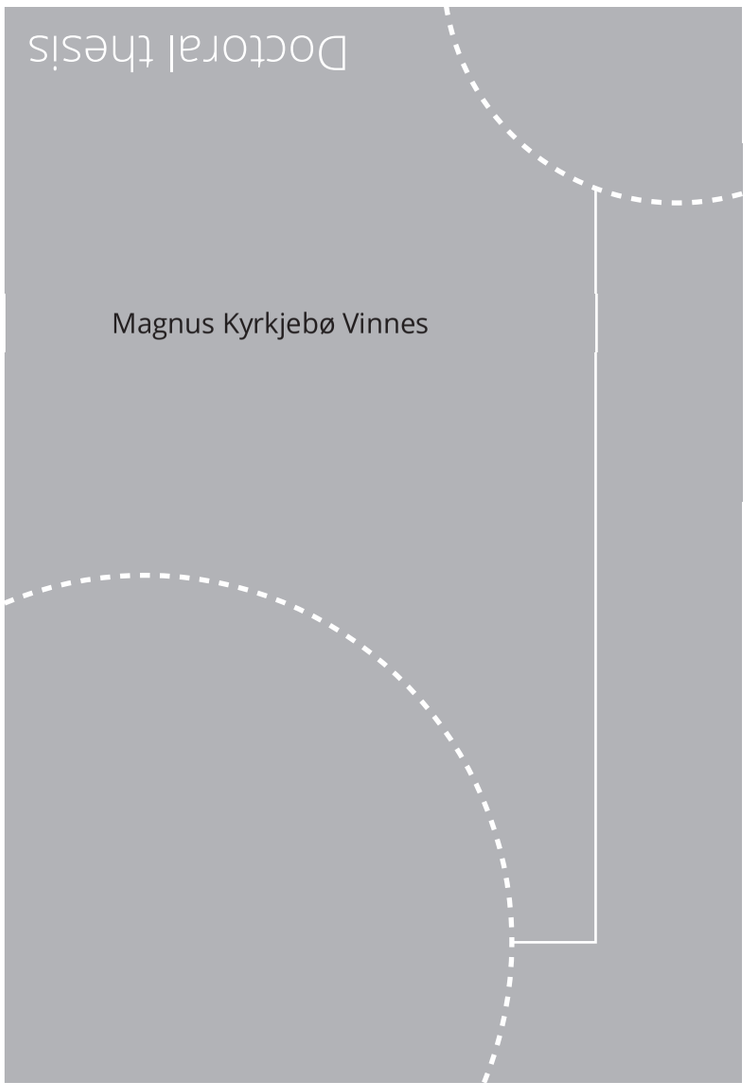

ISBN 978-82-326-5740-7 (printed ver.)
ISBN 978-82-326-5265-5 (electronic ver.)
ISSN 1503-8181 (printed ver.)
ISSN 2703-8084 (electronic ver.)

NTNU
Norwegian University of
Science and Technology

NTNU
Norwegian University of
Science and Technology
Thesis for the degree of
Philosophiae Doctor
Faculty of Engineering
Department of Energy and Process Engineering

Doctoral theses at NTNU, 2023:9

NTNU

Magnus Kyrkjebø Vinnes

The actuator disk as a wind turbine model: An experimental assessment of the fluid dynamics

Thesis for the degree of Philosophiae Doctor

Trondheim, January 2023

Norwegian University of Science and Technology
Faculty of Engineering
Department of Energy and Process Engineering

NTNU
Norwegian University of
Science and Technology

NTNU
Norwegian University of Science and Technology

Thesis for the degree of Philosophiae Doctor

Faculty of Engineering
Department of Energy and Process Engineering

ISBN 978-82-326-5740-7 (printed ver.)
ISBN 978-82-326-5265-5 (electronic ver.)
ISSN 1503-8181 (printed ver.)
ISSN 2703-8084 (electronic ver.)

Doctoral theses at NTNU, 2023:9

PRINTED IN NORWAY
NO - 1598

NORDIC SWAN ECOLABEL
Printed matter
2041 0731

Printed by Skipnes Kommunikasjon AS

Abstract

Climate change is one of the major challenges of our time. With ambitions to keep the average global temperature below 1.5° C above pre-industrial levels, significant efforts to transform the global energy production from fossil-based sources to renewable sources are required. There is, for example, steady growth in installed wind energy capacity. Typically, wind turbines are used as wind energy converters and are often grouped in wind farms. From a fluid mechanics perspective, it is interesting to study the interaction between the wakes of different turbines and the interaction between the wind farm flow and the atmospheric flow.

Much of the research on the topic is done numerically with actuator disks as wind turbine models. Actuator disks, in the form of porous disks, have also become a popular tool to simplify lab-scale experiments. However, there is no general agreement on the design of these devices, with very different designs found in the literature. Although the wakes of actuator disks and wind turbines have been compared for single wake generating objects, there is still a knowledge gap in understanding how actuator disks replicate the flow in a wind farm.

The first two projects in this thesis compare the flow around two different actuator disks, one with a uniform blockage and one with a non-uniform blockage. The wakes are measured through hot-wire anemometry at six streamwise positions, ranging from 3 to 30 diameters downstream of the objects. Neither disk can reproduce the asymmetry seen in a reference wind turbine wake in a laminar inflow. Moreover, the wakes of the two actuator disks are different. Firstly, the wake profiles differ in both velocity deficit and turbulence intensity. Secondly, the structures of the wake are different, with vortex shedding being observed only in the non-uniform disk wake, even though the total blockage ratio of the disks is the same. Increased ambient turbulence levels somewhat reduce these differences, but they are not elim-

inated. Lastly, there is a ring of highly intermittent flow around the actuator disk wakes, which has only been documented for a wind turbine wake earlier.

The third part of this thesis details a design process of an actuator disk. Several actuator disks are compared to a rotating wind turbine model. The thrust, or drag, of the wake generating objects is recorded with a force plate, and particle image velocimetry data of the near-wake is collected. The best design shows acceptable agreement in the mean quantities of the flow profiles between the wind turbine model and the actuator disk. Nevertheless, proper orthogonal decomposition and analysis of vortex structures show that instantaneous features of the flow are not matched.

For the last part of the thesis, the flow in the induction and entrance regions of wind farms is compared between actuator disks and rotating wind turbine models. Flow fields are captured through particle image velocimetry. It is shown that there are no measurable differences in the induction between farms consisting of rotating models and actuator disks, nor between different farm layouts and incoming flow angles. In the entrance region, the impact of instantaneous features in the wind turbine wakes is significantly reduced downstream of the second row of wind turbines, such that the flow downstream of the second row of actuator disks more closely resembles the flow downstream of the second row of turbine models.

In summary, the results show that it is possible to use actuator disks as static wind turbine models in lab-scale experiments, in particular when evaluating global features of the wind farm flow. Nevertheless, it is essential to consider the actuator disk design to replicate the wind turbine flow optimally. Furthermore, it is important to know that some features of the flow, in particular instantaneous vortex structures and asymmetries in the wind turbine flow, cannot easily be reproduced by actuator disks.

Preface

This thesis is submitted to the Norwegian University of Science and Technology (NTNU) for partial fulfillment of the requirements for the degree of Philosophiae Doctor. The doctoral work has been carried out in the Thermo Fluids Group at the Department of Energy and Process Engineering (EPT) from August 2018 to August 2022. The work has been supervised by associate professor R. Jason Hearst and co-supervised by professor Lars Sætran.

The research in this project was funded by NTNU.

The dissertation consists of four chapters and four scientific papers. The first three chapters introduce the field and review the literature, explain the theory, and demonstrate the experimental setup and methods. The research articles are summarized in Chapter 4 and are included in full text at the end of the thesis.

Article I
The far wake of porous disks and a model wind turbine: Similarities and differences assessed by hot-wire anemometry
Magnus K. Vinnes, Stefano Gambuzza, Bharathram Ganapathisubramani, and R. Jason Hearst
Journal of Renewable and Sustainable Energy, **14**, 023304, (2022)

Author contributions: MKV and SG performed the experiments. MKV analyzed the data and wrote the first draft of the manuscript. BG and RJH provided guidance and support. All authors contributed to editing the manuscript.

Article II

Characterizing porous disk wakes in different turbulent inflow conditions with higher-order statistics

Magnus K. Vinnes, Ingrid Neunaber, Hauk-Morten H. Lykke, and R. Jason Hearst

Under consideration for publication in Experiments in Fluids

Author contributions: MKV and HMHL performed the experiments. HMHL and MKV analyzed the data. HMHL wrote an early draft of the manuscript. MKV and IN revised the draft substantially. IN and RJH provided guidance and support. All authors contributed to editing the manuscript.

Article III

A comparison of lab-scale free rotating wind turbines and actuator disks

Sanne de Jong Helvig, Magnus K. Vinnes, Antonio Segalini, Nicholas A. Worth, and R. Jason Hearst

Journal of Wind Engineering and Industrial Aerodynamics, **209**, 104485, (2021)

Author contributions: SdJH performed the force measurements. MKV performed the PIV measurements. SdJH analyzed the data and wrote the first draft of the manuscript. MKV, AS, NAW, and RJH provided guidance and support. All authors contributed to editing the manuscript.

Article IV

The flow in the induction and entrance regions of lab-scale wind farms

Magnus K. Vinnes, Nicholas A. Worth, Antonio Segalini, and R. Jason Hearst

Under consideration for publication in Wind Energy

Author contributions: MKV performed the experiments, analyzed the data, and wrote the first draft of the manuscript. NAW, AS, and RJH provided guidance and support. All authors contributed to editing the manuscript.

Additional article, proceedings, and abstracts not formally included in this thesis:

Aerodynamics of an airfoil with leading-edge icing

Magnus K. Vinnes and R. Jason Hearst

Wind Energy, **24**(8), 795-811, (2021)

PIV of the flow over a NREL S826 airfoil subjected to different ice accretions

Magnus K. Vinnes, Leon Li, and R. Jason Hearst

Örlü, R., Talamelli, A., Peinke, J., Oberlack, M. (eds.), Progress in Turbulence VIII, iTi 2018, Springer Proceedings in Physics, **226**, 331–336, (2019)

Round-robin tests of porous disc models
Sandrine Aubrun et al.
Journal of Physics: Conference Series, Wake Conference 2019 22–24 May 2019, **1256**, 012004, (2019)

PIV of the aerodynamics of an airfoil subjected to icing
Magnus K. Vinnes, Leon Li, and R. Jason Hearst
71st American Physical Society Division of Fluid Dynamics Meeting, Atlanta, Georgia, Nov 19, 2018

High-order statistics of model wind turbine and actuator disk wakes
Magnus K. Vinnes, Stefano Gambuzza, Hauk-Morten H. Lykke, Bharathram Ganapathisubramani and R. Jason Hearst
Wind Energy Science Conference, Cork, Ireland, Jun 2019

The effect of turbulence on the near-field of porous disks
Magnus K. Vinnes, Hauk-Morten H. Lykke, and R. Jason Hearst
17th European Turbulence Conference, Turin, Italy, Sep 2019

Experimental assessment of the velocity field in a wind farm induction zone
Magnus K. Vinnes, Antonio Segalini, Nicholas A. Worth, and R. Jason Hearst
Wind Energy Science Conference, Hannover, Germany, May 2021

Acknowledgements

Even though this thesis only bears my name, many people are, in different ways, behind the work documented here. It is time for me to show gratitude to the people who have supported me over the last four years.

I can't see how I could have finished this thesis without the guidance and support from my supervisor, Associate Professor R. Jason Hearst. You have shown me the worlds of research and experiments, backed me up through conferences, and guided me through writing and analyzing. The effort and time you have put into my project are more than anyone could ever expect from a supervisor. Furthermore, I greatly appreciate the work and input from all my co-authors, without whom none of the papers within here would have been complete.

I have been lucky to be a part of the best research group I could imagine. To everyone in Jason's group and the rest of the Thermofluids group, thank you for the stimulating work environment and great social life. There has always been someone to help me in the lab, discuss results, and proofread everything I write. Even more important is all the fun we had together. My life has been enriched by short and long breaks (often involving ice cream or tea), Fluid Bowls (although I might skip the next go-kart session), trips, and other out-of-work activities.

I would also like to express my gratitude to my friends and family. You have kept me in touch with the world outside of the university. Thank you for keeping me company, supporting me, and being who you are.

Finally, I want to thank Malene and Johanne. Malene for enduring me not only through easy times but also in periods of long days in the lab, frustration, exhaustion, and lack of motivation. Johanne for bringing a bigger purpose. You are indeed my heroes and the most important people in my life.

Contents

Nomenclature

The following lists describes symbols and abbreviations used in this thesis. The symbols used in the individual journal articles will, in some cases, deviate from the ones given here.

Abbreviations

2D2C	Two-dimensional, two-component
ABL	Atmospheric boundary layer
AD	Actuator disk
CTA	Constant temperature anemometry
DC	Direct current
EPT	Department of Energy and Process engineering
HWA	Hot-wire anemometry
IBL	Internal boundary layer
LES	Large-eddy simulations
LiDAR	Laser imaging, detection, and ranging
MKE	Mean kinetic energy
MOSFET	Metal-oxide-semiconductor field-effect transistor
ND	Non-uniform disk

NHD	Non-uniform holes disk
NTNU	Norwegian University of Science and Technology
PDF	Probability density function
PID	Proportional integral derivative
PIV	Particle image velocimetry
PLA	Polylactic acid
POD	Proper orthogonal decomposition
RANS	Reynolds Averaged Navier-Stokes
SD	Solid disk
TI	Turbulence intensity
TSR	Tip-speed ratio
UD	Uniform disk
UHD	Uniform holes disk
VFD	Variable frequency drive
WGO	Wake generating object

Latin symbols

a_i^n	POD coefficient relating mode i to snapshot n
$\mathbf{A}$	Eigenvectors in POD analysis
A	Rotor swept area
a	Axial induction factor
C_P	Power coefficient
$\widetilde{\mathbf{C}}$	Autocovariance vector
$\widetilde{C_T}$	Modified thrust coefficient in linearized blockage model
C_T	Thrust coefficient
D	Diameter of wake generating object

E_{11}	Energy spectral density of streamwise velocity u
E	Voltage
F_T	Thrust force
F	Flatness
f	Function
I	Current
i	Number of POD mode
K_T	Proportionality constant
k_T	Thermal conductivity
k	Turbulent kinetic energy
M	Number of velocity vectors in snapshot for POD
N	Maximum count
n	Counter
P	Pressure
p	Probability function
Q_f	Torque lost to friction
Q_{sh}	Torque experienced by DC machine
S	Skewness
T	Temperature
t	Time
$\mathbf{u}'$	Vector containing all components of all velocity vectors in a snapshot for POD analysis
u'	Fluctuating streamwise velocity component
U_1	Velocity far upstream in AD-theory
U_2	Velocity at or just upstream of the rotor hub in AD-theory

U_∞	Freestream velocity
$\mathbf{U}$	Matrix of all velocity vectors from all snapshots $\mathbf{u}'$
$\vec{u}$	Instantaneous velocity vector
U	Time averaged velocity in the x-direction
u	Instantaneous streamwise velocity
v'	Second component of the fluctuating velocity
v	Second component of the instantaneous velocity
w'	Third component of the fluctuating velocity
w_s	Weighting applied in stitching of PIV-fields
w	Third component of the instantaneous velocity
$\vec{x}$	Position vector consisting of $[x, y, z]$
x	Streamwise coordinate originating at disk or turbine location
y	Second component of the position vector
z	Third component of the position vector

Greek symbols

α	Angle-of-attack
δu	Velocity increment
η	Kolmogorov length
θ	Geometrical pitch angle
$\lambda^2(\tau)$	Shape parameter
λ_i	Energy content of POD-mode i
λ	Signed swirling strength
ν	Kinematic viscosity
$\vec{\xi}_n$	Position of turbine n in linearized blockage model
ξ	x-component of $\vec{\xi}_n$

ρ	Density
σ	Standard deviation
τ	Time lag used in velocity increment
$\mathbf{\Phi}$	POD modes
ω_r	Rotational speed
$\vec{\omega}$	Vorticity vector
ω_z	Vorticity around z-axis

Chapter 1

Introduction

1.1 Motivation

To keep global warming well below 2° C, decision-makers worldwide increase their ambitions and efforts to reduce greenhouse gas emissions (UNFCCC 2015). To meet these targets, power sources for electricity generation, heating, and transport must change from mainly fossil to a large share of renewables. There are several renewable electricity sources, of which wind and solar energy are the most common. The share of worldwide electricity generation by these two sources is predicted to rise from 8% in 2019 to 30% in 2030 (IEA 2020), and they are in many locations the cheapest options for new power plants (IEA 2021). In 2020, wind energy alone accounted for 24% of the global investments in new power generation (REN21 2021). The yearly added wind power capacity is growing steadily (REN21 2021), a trend that is expected to continue (GWEC 2022).

The typical way to exploit wind energy is with wind turbines. They convert the momentum in the wind to rotational movement, giving power to an electrical generator. Wind turbines are often grouped in clusters called wind farms to minimize the cost of installation and operation. While this is a good solution to reduce the required infrastructure and associated costs, it also reduces the performance of each turbine. Most noticeably, many turbines will be located, partly or wholly, in the wakes of upstream turbines. They will thus experience reduced wind velocities compared to the undisturbed wind, reducing the power production of the turbines (Barthelmie and Jensen 2010, Adaramola and Krogstad 2011). In addition, the turbulent nature of the wakes increases the mechanical loads on the turbines (Thomsen and Sørensen 1999).

Also, the total effect of the blockage a wind farm exerts on the flow field leads to reduced incoming wind velocities, lowering the production of even the leading wind turbines in a farm (Bleeg et al. 2018, Segalini and Dahlberg 2020). Thus, it is important to know about the flow inside and around a wind farm to exploit the wind resources optimally (Veers et al. 2019). Both measurements in the field and in the laboratory, as well as numerical simulations, are needed to increase our understanding and develop better models for wind farm planning (Stevens and Meneveau 2017).

1.2 Background

This section will introduce the state-of-the-art of wind turbine and wind farm flows. Furthermore, it will describe the methodology of using actuator disks (ADs) as wind turbine models in simulations and lab-scale experiments, which has become a popular tool in wind energy research.

1.2.1 Flow around a wind turbine

In the process of generating electrical power, a wind turbine in operation also alters the surrounding flow. The flow velocity upstream of the wind turbine is reduced due to the imposed blockage. The region where this can be observed is called the induction region. Moreover, by extracting energy from the flow, the wind turbine reduces the velocity in the wake downstream of the turbine. These effects are shown schematically in the time-averaged part of Figure 1.1 and will be described further in the following sections. Furthermore, the flow in the induction region and the wake is also influenced by the turbulence and shear of the atmospheric boundary layer (ABL), in which wind turbines typically operate. When there is a direct impact of the ABL on the described flow phenomena, this will be mentioned.

Wind turbine induction region

The reduction of the mean velocity U compared to the freestream velocity U_∞ in the induction region can be described by the vortex sheet theory model

$$\frac{U}{U_\infty} = 1 - a\left(1 + \frac{2x}{D}\left[1 + \left(\frac{2x}{D}\right)^2\right]^{-1/2}\right), \tag{1.1}$$

derived from the Biot-Savart law (Medici et al. 2011). It is valid for the velocity directly upstream of the hub or nacelle of the wind turbine. Here, x is the streamwise coordinate originating at the turbine location, D is the turbine diameter, and the axial induction factor a, defined as

$$a = \frac{U_1 - U_2}{U_1}, \tag{1.2}$$

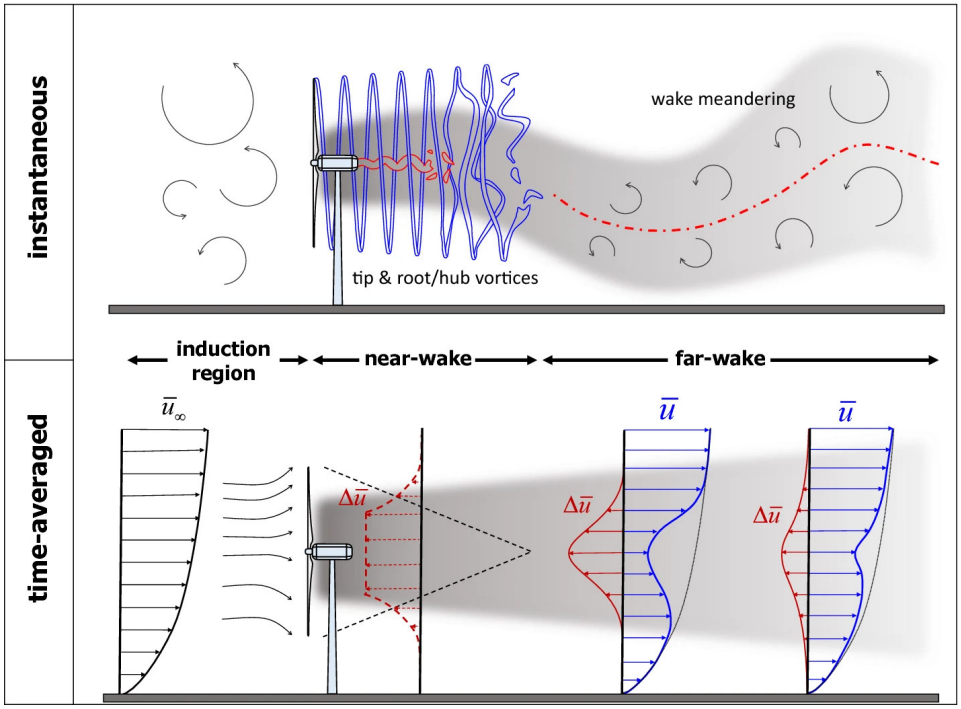

Figure 1.1: The instantaneous and time-averaged flow around a wind turbine. The figure is reproduced from Porté-Agel et al. (2020).

is the difference between the undisturbed velocity far upstream (U_1) and the velocity at, or just upstream of the, rotor hub (U_2). Medici et al. (2011) found that Equation 1.1 agrees well with their numerical simulations. However, both theory and simulations underpredict the velocity reduction compared to hot-wire measurements upstream of three different lab-scale wind turbines reported in the same work (Medici et al. 2011). Later studies found that the model agrees with lab-scale measurements (Howard and Guala 2016, Bastankhah and Porté-Agel 2017), but that it has some discrepancies compared to field measurements (Howard and Guala 2016, Simley et al. 2016, Li, Abraham, Li and Hong 2020). Still, Equation 1.1 gives an indication of the velocity in the induction region (Porté-Agel et al. 2020).

The applicability of the vortex sheet model (Equation 1.2) is limited to only the line straight upstream of the center of the wind turbine rotor. The region of reduced velocity, however, also spans the radial direction. To study the induction region, Troldborg and Meyer Forsting (2017) performed Reynolds Averaged Navier-Stokes (RANS) simulations with a uniform incoming flow. Their results show that the spanwise velocity profiles are not highly dependent on the rotor design and

that, when scaled with their width and maximum velocity deficit, they are close to self-similar more than $0.5D$ upstream of the rotor. However, lab-scale experiments show an asymmetry in the spanwise velocity profile in the induction region (Bastankhah and Porté-Agel 2017), which the authors designated to be an effect of varying angle-of-attack of the rotor blades due to their operation in a boundary layer. Through laser imaging, detection, and ranging (LiDAR) measurements, Simley et al. (2016) showed that the presence of the turbine decreased the streamwise velocity in the induction region, but that the radial velocity had an increased outward magnitude near the edges. Moreover, the presence of the wind turbine reduced the streamwise fluctuations while it increased the standard deviation in the radial direction.

Wind turbine wake

A turbine located in the wake of an upstream turbine suffers production losses due to reduced velocity and increased loads due to higher turbulence. Barthelmie and Jensen (2010) found that turbines located in the center of the Nysted offshore wind farm produced up to 20% less power than turbines on the edge of the same farm, depending on the inflow conditions. In an experimental campaign with uniform inflow conditions, Adaramola and Krogstad (2011) found that a turbine in the wake of an upstream turbine suffered a loss between 20% and 45% in the maximum power coefficient. Due to increased turbulence intensity (TI) and reduced turbulence length scales in the wake of upstream turbines, the fatigue loads experienced by a full-scale wind turbine in a wind farm are 5% to 15% higher than the loads a stand-alone turbine faces (Thomsen and Sørensen 1999). Thus, it is important to understand the physics governing the turbulent flow in a wind turbine wake.

As shown in Figure 1.1, the wind turbine wake is often separated into two major regions, namely the near-wake and the far-wake (Vermeer et al. 2003, Porté-Agel et al. 2020). In brief, the near-wake covers the region where the shear layers of the time-averaged velocity surrounding the wake have not yet met, and the tower, nacelle, and rotor heavily influence the flow; tip-, root-, and hub-vortices are present. $2-4D$ downstream of the turbine, these structures break up, and the flow can often be predicted by global parameters such as the incoming flow, thrust and power generation (Porté-Agel et al. 2020). Both the near-wake and the far-wake will be introduced here. For a more extensive description on the wind turbine wakes, the review papers by Vermeer et al. (2003), Stevens and Meneveau (2017), and Porté-Agel et al. (2020) are recommended.

The near-wake The velocity distribution in the near-wake depends on the operating conditions of the wind turbine. For example, Krogstad and Adaramola (2012) showed that at high tip-speed ratios (TSR), that is, the ratio between the speed of the

Wind Farm	Reference	Spacing [D]
Nysted	Barthelmie and Jensen (2010)	5.8 – 10.5
Horns rev I	Gaumond et al. (2014)	7
Rødsand II	Hansen et al. (2015)	5 – 10
Greater Gabbard	Argyle et al. (2018)	8.3 – 10
Princess Amalia	Fleming et al. (2016)	6.9 – 7.1

Table 1.1: Exemplary spacings between wind turbines in different wind farms.

blade tip of the turbine and the incoming flow velocity, a region of higher velocities was present in the center of the wake. The wind turbine tower breaks the axisymmetry of the wake and shifts it towards the ground (Pierella and Sætran 2017). The near-wake rotates in the opposite direction of the turbine blades (Medici and Alfredsson 2006). The rotation is stronger near the turbine, before it gradually slows down farther downstream (Zhang et al. 2012).

Different instantaneous vortex structures dominate the near-wake. Most prominent are the tip-vortices shed from the rotor blades, arising from the pressure difference between the suction and pressure side of the tip of the airfoil (Manwell et al. 2009). The tip-vortices are transported in a rotating helical path by the mean rotation of the wake, making a layer of high mean vorticity along the edge of the wake. It has been shown that this layer of coherent vortex structures reduces the mixing with the freestream flow surrounding the wake and hence reduces the energy entrainment from the ambient flow (Lignarolo et al. 2014). Root-vortices are shed from the root of the blades, but due to the effect of the turbine support structure, they persist over a shorter distance than the tip-vortices (Sherry et al. 2013). The extent of the near-wake is, to some extent, dependent on how long the tip vortices persist. Several studies show that higher ambient turbulence levels enhance the breakdown of tip-vortices, and hence that high freestream turbulence accelerates transition to the far-wake. (Medici and Alfredsson 2006, Aubrun et al. 2013, Barlas et al. 2016, Li, Hearst, Ferreira and Ganapathisubramani 2020).

The far-wake The far-wake of a wind turbine is, perhaps, a simpler flow. The tip and root vortices of the near-wake have broken down, and the mean rotation of the wake has diminished. In most modern wind farms, turbines have a spacing of 5-10D in the dominating wind direction (see Table 1.1 for examples). Downstream turbines are thus rarely located in the near-wake but rather in the far-wake of upstream turbines. It is thus not surprising that the far-wake has received considerable attention in the literature.

The mean velocity deficit is defined as the velocity of the flow in the wake subtrac-

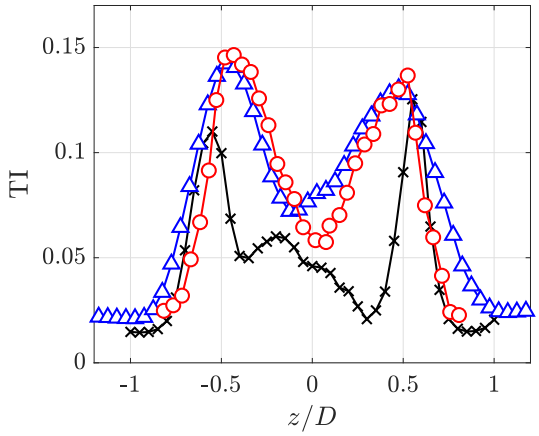

Figure 1.2: Examples of turbulence intensity profiles around $3D$ downstream of a wind turbine. z/D is the spanwise position. Data extracted from Bartl and Sætran (2017) (×), Zhan et al. (2020) (△), and Piqué et al. (2022) (○).

ted from the velocity at the same position under the same flow conditions, without the presence of the wind turbine. The velocity deficit in the far-wake of a wind turbine can be well approximated by a Gaussian distribution (Medici and Alfredsson 2006, Bastankhah and Porté-Agel 2014, Duckworth and Barthelmie 2008, Piqué et al. 2022), even when located in the shear of a boundary layer (Chamorro and Porté-Agel 2009). Farther downstream, the wake expands, and the velocity deficit is reduced (e.g., Barthelmie et al. (2003), Aitken et al. (2014)). Due to enhanced mixing, the wake recovery rate increases with higher turbulence levels in the ambient flow (e.g., Duckworth and Barthelmie (2008), Maeda et al. (2011), Aubrun et al. (2013), Barlas et al. (2016), Fuertes et al. (2018), Zhan et al. (2020)).

After a region of high turbulence production in the near-wake, the TI begins to decay in the far-wake. The breakdown of tip-vortices and merging of the shear layers significantly reduce the turbulence production. Upstream of this transition point, the TI profile is characterized by two peaks, as illustrated in Figure 1.2 (Maeda et al. 2011, Bartl and Sætran 2017, Zhan et al. 2020, Piqué et al. 2022), one at each shear layer, stemming from the high production in the tip-vortex layer. In the vertical direction, the TI peak at the height of the top tip is more pronounced than the peak at the bottom tip due to the effect of the ABL (Chamorro and Porté-Agel 2010). Farther downstream, the peaks diminish and the TI equalizes over the horizontal wake profile (Maeda et al. 2011, Wu and Porté-Agel 2012, Iungo et al. 2013, Zhan et al. 2020).

So far, the features of the far-wake have only been discussed with respect to the

mean velocity and TI. However, to fully characterize a turbulent flow, both higher-order turbulent statistics and, in particular, two-point turbulent statistics are necessary. Such statistics reveal information about, for example, the likelihood of extreme velocity events and periodic structures in the flow. An introduction to these measures will be given in Section 2. Aubrun et al. (2013) reported profiles of skewness and flatness downstream of a model wind turbine and a static porous disk, both in the near-wake and at the beginning of the far-wake. They show that the distribution of turbulent fluctuations in the wake is not Gaussian-like, but with increased magnitudes of skewness and flatness, in particular in the shear layers. The vortex shedding known to appear in the wake of bluff bodies is not found downstream of wind turbines. Instead, the wake oscillates sideways at low frequencies, called meandering. Medici and Alfredsson (2006) connected the wake meandering to vortex shedding phenomena. Later studies have instead connected the meandering to transport by the large turbulent scales in the incoming boundary layer flow (España et al. 2011, Muller et al. 2015), and there is now a general agreement that the meandering stems from such large-scale structures in the background flow (Porté-Agel et al. 2020). The intermittency, or "gustiness", of the incoming flow is reduced by the wind turbine, leaving a less intermittent flow in the wake (Singh et al. 2014, Bastine et al. 2015, Neunaber et al. 2021). In fact, some studies suggest that the turbulent characteristics in the wake are not dependent on the inflow conditions but a signature of the turbine itself (Neunaber et al. 2020). Schottler et al. (2018) showed a ring of highly intermittent flow surrounding the wake (if the velocity deficit defines the wake), effectively increasing the size of the wake. This intermittency ring is important, as intermittency in the incoming flow has been found to increase the fatigue loads on turbines (Schwarz et al. 2018).

1.2.2 Wind farm flow

Up to now, the impact of the wind turbine on the surrounding flow has been discussed. However, in wind farms, there is also an interaction between the individual turbines. Turbines are located in the wakes of upstream turbines, the wakes of different turbines interact, and the sum of the turbines imposes a global blockage reducing the incoming velocity to the farm. This section will introduce the flow in and around a wind farm. Extensive descriptions of the wind farm flow can be found in Stevens and Meneveau (2017) and Porté-Agel et al. (2020).

It is common to separate the flow over and around a wind farm into the induction region, the entrance and development region, the fully developed region, the exit region, and the wind farm wake (see for example Stevens and Meneveau (2017) and Porté-Agel et al. (2020)). The four foremost regions are illustrated schematically in Figure 1.3. It should be noted that the extent of the different flow regions and the development of the internal boundary layer (IBL) depend on the extent of the

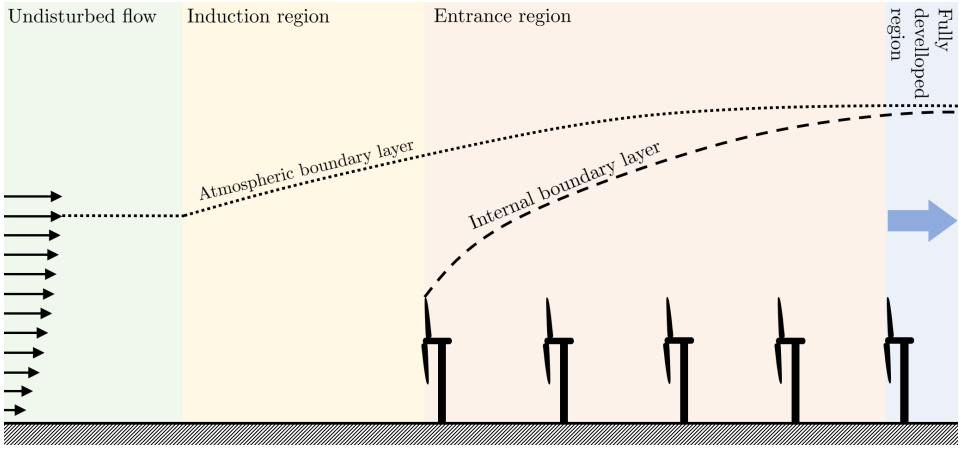

Figure 1.3: Schematics of the flow regions in the beginning of a wind farm. The figure is not to scale.

farm and the ABL (Wu and Porté-Agel 2017). The effect of the stratification and stability of the ABL is, however, considered to be out of the scope of this work and will not be discussed further.

In the recent years, the induction region of wind farms has received considerable attention. Bleeg et al. (2018) demonstrated, both through field measurements and simulations, that there is a significant reduction in available wind resources before and after installing and putting three different wind farms in operation. The magnitude of this velocity reduction cannot be explained exclusively by the single wind turbine induction. It has been shown that reducing the lateral spacing between turbines in a row can increase the power production due to acceleration of the flow going around the neighbouring turbine (McTavish et al. 2015, Meyer Forsting et al. 2017, Strickland and Stevens 2022). However, when several rows of turbines are present, the total blockage of the farm reduces the incoming velocity. The magnitude depends on the stratification of the ABL (Schneemann et al. 2021) and the turbine spacing (Segalini and Dahlberg 2020, Strickland and Stevens 2022), but is on the order of a few percent velocity reduction. Both Branlard and Meyer Forsting (2020) and Segalini (2021) have developed models to predict the effect of the global blockage. The latter model superimposes the induction of all the individual turbines (N) and reads

$$\frac{U(\vec{x})}{U_\infty} = 1 + \sum_{n=1}^{N} \frac{\tilde{C_T}(x - \xi_n)}{8\left|\vec{x} - \vec{\xi}_n\right|^3}, \tag{1.3}$$

where, $\vec{x} = [x, y, z]$ is the position vector, and $\vec{\xi}_n$ is the position of turbine n, with ξ

representing the x-position. The modified thrust coefficient $\widetilde{C}_T$ is calculated from the regular thrust coefficient

$$C_T = \frac{F_T}{\frac{1}{2}\rho U_\infty^2 A} \tag{1.4}$$

as

$$\widetilde{C}_T = 2\left(1 - \sqrt{1 - C_T}\right) \tag{1.5}$$

to compensate for the linearity of the model. Here, F_T is the thrust force experienced by the turbine, ρ is the density of the air, and A is the rotor swept area.

The flow inside a wind farm, that is, the flow downstream of the leading turbine and below the height of the top tip of the turbines, is governed by the wakes of the different turbines and their interactions. Low velocities and high TI characterize the wind farm flow compared to the undisturbed flow. The high turbulence levels in the incoming flow of downstream turbines promote wake recovery. For example, the tip-vortices break down much faster and are not measurable in downstream regions of a farm (Chamorro and Porté-Agel 2011). Already after the second row of turbines, they cease to exist (Segalini and Chericoni 2021).

The flow inside, and thus power production of, a wind farm depends on the wind farm's layout. Generally, the rows following the leading row of turbines experience higher production penalties in a layout aligned with the flow direction than for a staggered case (Bossuyt et al. 2017, Wu et al. 2019). Combined with the effect of larger spacing between turbines in the streamwise direction, this leads to a higher velocity approaching each turbine, giving higher total production in a staggered farm (Markfort et al. 2012, Wu and Porté-Agel 2013, Archer et al. 2013, Hamilton et al. 2015). The aligned and staggered layouts are idealized cases of wind farm layouts. In reality, the varying incoming wind direction leads to continuous changes in wind farm layouts. As for the different layouts, the wind direction is important for the production (Barthelmie et al. 2010, Stevens et al. 2014), even for small changes in the flow angle (Porté-Agel et al. 2013).

Although the layout and wind direction are important for production, this is more significant in the first rows where the incoming flow determines the power production (Stevens et al. 2014). Deeper in the wind farm, the entrainment of high momentum flow from above the farm governs the production (Stevens et al. 2016). In the fully developed region, the flux of mean kinetic energy (MKE) into the farm is dominated by transport by velocity fluctuations (Cal et al. 2010, Calaf et al. 2010). The largest turbulent structures contribute most to the entrainment (Newman et al. 2014). In the entrance and development region, however, the entrainment of MKE by the mean vertical velocity is larger (Newman et al. 2013, Cortina et al. 2020, Segalini and Chericoni 2021). From the leading turbine of the farm, the IBL starts

to grow inside the ABL, reducing the flow velocity just above the turbines. In a large wind farm, the IBL will eventually grow to the size of the ABL (Porté-Agel et al. 2020).

1.2.3 Flow field description and investigation

For industrial applications, i.e., planning site-specific wind farm layouts, it is still too expensive to use advanced numerical methods such as large-eddy simulations (LES). The number of incoming flow directions and operating conditions make it unfeasible. Therefore, analytical and empirical models are widely used (Porté-Agel et al. 2020). They are generally categorized into bottom-up models and top-down models. The former superpositions the effect of individual turbines, while top-down models give information on horizontally-averaged effects on the atmospheric boundary layer (Stevens and Meneveau 2017). The Jensen model (Jensen 1983) and the Frandsen model (Frandsen et al. 2006) are perhaps the most known wake models for wind farm planning. Still, improvement of models receives significant attention (e.g., Bastankhah and Porté-Agel (2014), Doubrawa et al. (2017), Cheng and Porté-Agel (2018), Blondel and Cathelain (2020), Bastankhah et al. (2021)).

While engineering models are good for planning wind farm layouts and estimating power production, they are unsuitable for increasing our understanding of flow physics. For that, it is possible to do numerical modelling, such as LES (e.g., Ivanell et al. (2010), Archer et al. (2013), Stevens et al. (2014), VerHulst and Meneveau (2015), Allaerts and Meyers (2018), Gadde and Stevens (2021), Strickland and Stevens (2022)), lab-scale experiments (e.g., Theunissen et al. (2015), Bossuyt et al. (2017), Bastankhah and Porté-Agel (2017), Li, Hearst, Ferreira and Ganapathisubramani (2020), Neunaber et al. (2020), Segalini and Dahlberg (2020), Segalini and Chericoni (2021)), and field measurements (e.g., Barthelmie et al. (2009), Barthelmie and Jensen (2010), Käsler et al. (2010), Iungo et al. (2013), Bodini et al. (2017), Zhan et al. (2020), Schneemann et al. (2021). All of these approaches have their advantages and disadvantages. LES can calculate entire flow fields but depend on modeling the smallest turbulent scales of the flow. Therefore, the results must carefully be validated and verified. Field measurements give information about the real flow physics but are usually limited to point measurements or sometimes limited planes of data (e.g., Li, Abraham, Li and Hong (2020)). It is also hard to characterize the incoming flow, and the results are often binned into groups determined by the flow condition. Full control over the incoming flow can be achieved in lab-scale experiments. However, scaling issues compared to full-scale turbines arise. In particular, the TSR and the Reynolds number cannot usually be matched simultaneously. Therefore, a combination of simulations, lab-scale experiments, and field measurements are needed to increase our knowledge and develop better analytical and empirical models (Stevens and Meneveau 2017).

Only a few examples of high Reynolds number lab experiments exist. In some, highly pressurized flow is used to increase the Reynolds number (e.g., Miller et al. (2019)), allowing simultaneous matching of the TSR. Another approach is to increase the turbine diameter to increase the Reynolds number. This was, for example, done in the New MEXICO measurement campaign, where a 4.5 m diameter turbine was placed in the German Dutch Wind Tunnel, (see for example Schepers et al. (2018)). The Reynolds number is still around two orders of magnitude lower than for utility scale wind turbines, where the largest are now reaching diameters of more than 200 m (REN21 2021). Few facilities allow for high pressure wake measurements, or can fit MEXICO-sized turbines. Most lab-scale experiments must therefore be performed at Reynolds numbers one or several orders of magnitude below the New MEXICO campaign. Hence, it is important to interpret results with care, bearing in mind that, most likely, scaling effects are present. Nevertheless, the benefits of the ability to perform advanced flow measurements (whereof some are described in Section 3.3) and carefully control the incoming flow makes lab-scale experiments a valuable resource for obtaining knowledge about wind turbine and wind farm flows (Porté-Agel et al. 2020). To generate the desired inflow conditions, passive devices such as grids, spires, and roughness elements can be used to simulate the ABL or produce turbulent flows (e.g., Hamilton et al. (2015), Bartl and Sætran (2017)). Furthermore, active grids can be used to tailor specific combinations of velocity profiles and TI (e.g., Hearst and Ganapathisubramani (2017), Li, Hearst, Ferreira and Ganapathisubramani (2020)), and even generate time varying flow conditions as demonstrated with the active grids at the University of Oldenburg (e.g., Wächter et al. (2012), Neuhaus et al. (2021), Berger et al. (2022)).

One of the challenges in both simulations and lab-scale experiments is how to represent the wind turbine. Resolving the blades and including the rotation in numerical models is costly; with the technology of today it is more or less impossible. Operating and controlling wind turbines is a challenge in lab-scale experiments, particularly when investigating wind farm flows, requiring a high number of wind turbines. Furthermore, the design of miniature turbines is not straightforward, as they typically have larger chord-to-length ratio of the blades, hub-to-diameter ratio, and different airfoil profiles than full-scale turbines. As such, the use of ADs, represented by porous disks in experiments, has become popular. The remaining part of this section will introduce the concept of this simplification and describe the implementation of ADs as static wind turbine models in lab-scale experiments.

The actuator disk

Based on linear momentum theory, Betz (1926) developed a model to relate the flow around a wind turbine to the thrust of the turbine. As it is a well-known model, found in textbooks such as Manwell et al. (2009), only a brief introduc-

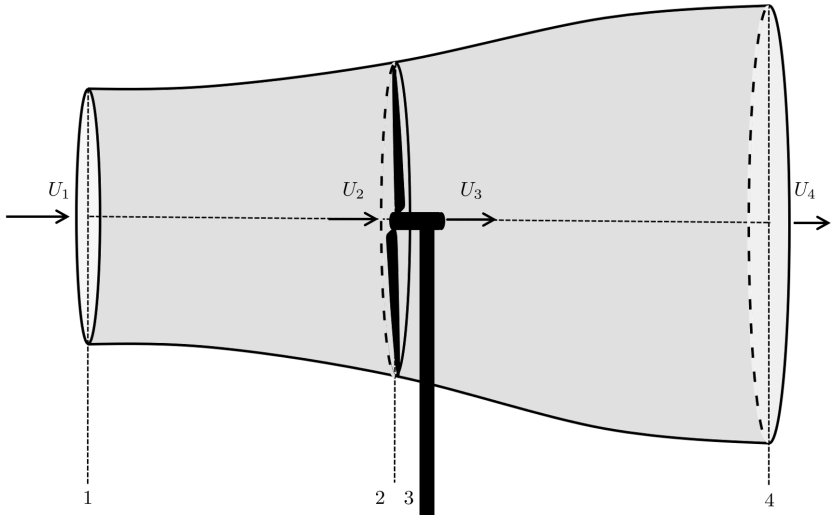

Figure 1.4: The stream tube around a wind turbine modelled by linear momentum theory.

tion will be given here. A control volume is defined by the stream tube limited by the flow passing through the rotor swept area. The start of the stream tube is taken upstream, where the flow can be considered undisturbed by the wind turbine (cross-section 1 in Figure 1.4) and ends somewhere downstream (cross-section 4 in Figure 1.4). As such, flow only enters and leaves the control volume at the stream tube's start and end. The wind turbine rotor is modeled as a pressure drop extracting energy from the flow, shown as the cross-section between positions 2 and 3 in Figure 1.4. This pressure drop is in computations referred to as the AD. The AD model is based on several assumptions: the flow is steady, homogeneous, and incompressible, frictional drag is neglected, the rotor consists of an infinite number of blades, the thrust over the disk or rotor area is distributed uniformly, there is no rotation of the wake, and the static pressure is equal around the control volume. From the model, the axial induction factor a, defined in Equation 1.2, can be related to C_T through

$$C_T = 4a(1 - a). \tag{1.6}$$

Due to the relatively low computational costs compared to resolving the full wind turbine rotor with rotation, the AD methodology is frequently used in computational fluid dynamics considering wind farm flows (see for example Stevens et al. (2014), VerHulst and Meneveau (2015), Stevens and Meneveau (2017), Allaerts and Meyers (2018), Porté-Agel et al. (2020), Gadde and Stevens (2021)). The applicability of the AD model in simulations has been investigated by comparing to lab-scale experiments (Wu and Porté-Agel 2013, Simisiroglou et al. 2017, Stevens

et al. 2018), field measurements (Wu and Porté-Agel 2015), and simulations with rotating models (Martínez-Tossas et al. 2015, Dong et al. 2022). Even though there are some discrepancies in the comparisons, the AD model generally predicts the flow field acceptably.

Actuator disks in lab-scale experiments

The idea of using ADs, realized by porous disks, as static wind turbine models originated no later than in the early 1980s, exemplified by the work of Sforza et al. (1981). They measured the wake properties of perforated disks with different blockage and thus C_T. Since the experiments of Sforza et al. (1981), ADs have become a popular tool to model wind turbines in lab-scale experiments. For example, España et al. (2011; 2012) and Muller et al. (2015) used ADs to investigate wake meandering. Howland et al. (2016) described the curled shape of the wake downstream of a yawed wind turbine using an AD. Unsteady loading on an AD was investigated by Yu et al. (2017). Abdulrahim et al. (2021) investigated the effect of the boundary layer on the wake of an AD. Recently, Travis et al. (2022) studied the effect of inertial particles in the turbulent flow around an AD. While the studies mentioned above focus on the flow around single units, even larger simplifications can be made by using ADs in a wind farm. Theunissen et al. (2015) measured the dag of a wind farm consisting of ADs to estimate production of the farm, while Bossuyt et al. (2017) measured the power output of a farm by mounting strain gages on ADs.

Porous disk wakes, not necessarily used as wind turbine models, have also received attention in the literature. Cannon et al. (1993) showed that for wire mesh disks with a blockage of less than 60%, the vortex shedding commonly found in the wake of bluff bodies ceased to exist. This is perhaps why Higuchi et al. (1998) found that the structures are more axisymmetric in the wakes of perforated disks compared to solid disks. Farther downstream than $6D$, the structure of the wakes of mesh disks becomes independent of their blockage (Myers and Bahaj 2010). Different results have been reported on the effect of the maximum velocity deficit. While Lin et al. (2017) found that a perforated disk had a higher maximum velocity deficit than a solid disk, Xiao et al. (2013) reported the opposite. Theunissen and Worboys (2019) investigated the near-wake of different high blockage porous disks and showed that porosity is the main determining factor for the drag but that the topology also has a small impact.

Many of the features in a wind turbine wake, for example the tip-vortices and mean rotation, cannot be replicated in the wake of a static AD. It is, however, generally accepted that ADs can give acceptable flow profiles in the far-wake. This was also the conclusion of Aubrun et al. (2013), who matched wake profiles of turbulent statistics up to fourth-order between wakes of a rotating wind turbine and a wire mesh

disk. They performed hot-wire anemometry (HWA) in both decaying isotropic turbulence and a simulated ABL. $0.5D$ downstream of the wake generating objects (WGOs) the tip-vortices were evident, but due to turbulent diffusion, they diminished upstream of the second measurement location at $3D$. Later, through stereo particle image velocimetry (PIV) Lignarolo et al. (2016) found that even though the mean profiles in the wake of a wire mesh disk and a 2-bladed turbine are similar, the mechanisms of turbulent mixing are different. However, they state that the mixing is similar in magnitude, such that ADs can be used as wind turbine models if care is exercised. The wakes of a non-uniform AD and a wind turbine, both located in the fourth row of a wind farm, were compared by Camp and Cal (2016; 2019). They report significant differences in turbulence production, turbulent stresses, and vertical energy entrainment in the near-wake. For all these features, the magnitudes are higher for the wind turbine. Still, as in the other studies, the differences are found to be small farther than $3D$ downstream of the WGOs. Neunaber et al. (2021) showed that the evolution of turbulence statistics is similar between a non-uniform porous disk and a wind turbine in the far-wake, where the turbulence in both wakes displays universal behavior. Even though turbines in a wind farm typically are located between $5D$ and $10D$ apart (see Table 1.1), and even farther if the wind direction is misaligned with the columns of turbines, the studies mentioned above focus on the near-wake and the beginning of the far-wake. To the author's knowledge, no comparison extends much farther than $5D$ downstream of the WGOs.

Even though ADs, in general, are often used as wind turbine models in experiments, there is no agreement on the design. In fact, there are very different designs in different experiments. The designs can roughly be divided into two groups: ADs with uniform design and ADs with non-uniform design. Schematic examples of the different designs are shown in Figure 1.5, with a typical uniform disk to the left, and a often used non-uniform disk on the right. Uniform disks have been used by for example Cannon et al. (1993), España et al. (2011; 2012), Muller et al. (2015), Lignarolo et al. (2016) and Yu et al. (2017). They are often realized as cut wire meshes, such as the AD in the left part of Figure 1.5. Some studies have used two meshes with different blockages for different radial positions to mimic wake features more accurately (e.g., Aubrun et al. (2013)), but they are categorized as uniform here since the blockage of each mesh is uniform. Another example of a uniform disk design is the perforated disk, for example, the ones used by Sforza et al. (1981). The non-uniform design often has a gradually decreasing blockage with increasing distance from the center, to mimic the higher relative blockage of the blades near the nacelle. The typical design consists of radial spars held together by rings at different radial positions, giving them the look of a dart-board as seen in the right part of Figure 1.5. They have been used in several studies, for example Howland et al. (2016), Camp and Cal (2016; 2019), Bossuyt et al. (2017),

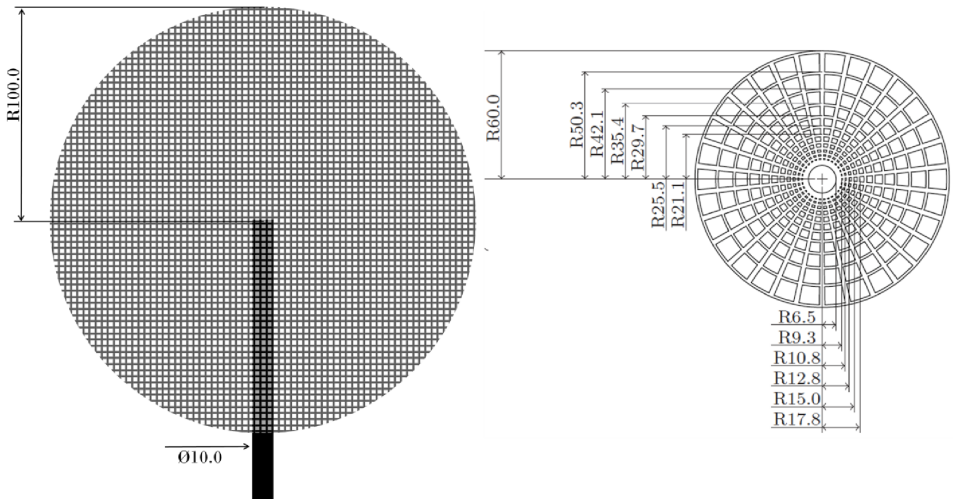

Figure 1.5: Schematics of typical examples of a uniform actuator disk (left) and a non-uniform actuator disk (right). The figure is reproduced from Aubrun et al. (2019).

Abdulrahim et al. (2021) and Travis et al. (2022). Neunaber et al. (2021) used a specific type of such a disk, with non-uniform spacing between the spars and a non-solid circumference. A different type of non-uniform disk is the perforated design used by Theunissen et al. (2015) in their wind farm experiments. To address the applicability of different disks, Aubrun et al. (2019) compared the wakes of the two disks shown in Figure 1.5 with different measurement techniques and different facilities. The results showed different wakes between the disks and different results between different facilities. As such, further study of the differences between different disks is needed.

1.3 Objectives

This thesis seeks to understand the flow around ADs and how well it replicates the flow around wind turbines. Although this has, to some extent, received attention in the literature, several research questions remain. The objectives of this thesis can be summarized in four research questions.

1. *How similar are the flows downstream of a uniform and a non-uniform actuator disk?*

There is no study comparing the wakes of ADs based on the two main design principles defined here, namely the uniform design and the non-uniform design. Al-

though both designs were studied by Aubrun et al. (2019)[1], the disks had different sizes and blockages and the objective of the study was to compare measurements in different facilities and with different techniques. To that end, Article I evaluates the wake of a uniform disk, the same as used by Aubrun et al. (2019), and a non-uniform disk based on the design of the AD from Camp and Cal (2016; 2019), which was also used in Aubrun et al. (2019). The disks in Article I have the same size, blockage, and approximately the same drag, such that they can be compared directly. Furthermore, wake profiles are taken up to $30D$ downstream of the two ADs, as well as a solid disk and a wind turbine as reference cases. In this way, potential differences in the far-wake will also be revealed.

2. *How does freestream turbulence influence the wakes of a uniform and a non-uniform actuator disk?*

While Article I investigates the AD wakes in a low-turbulent flow to emphasize differences between them, full-scale wind turbines experience turbulent incoming flows. Therefore, Article II expands the comparison between the two ADs by adding freestream turbulence to the base flow. The focus is on the wakes generated by the two ADs, expanding the investigation of the temporal features, particularly with an analysis of the flow's intermittency. Intermittency has earlier been shown to increase fatigue loads on wind turbines, and is thus an important parameter (Schwarz et al. 2018). Schottler et al. (2018) showed that a ring of high intermittency is found around the wake of a wind turbine. This ring surrounds the typical wake borders defined from first and second-order one-point statistics. To the author's knowledge, this has not been shown for AD wakes.

3. *How should an actuator disk be designed such that it replicates the flow field around a wind turbine?*

In the literature, most studies used ADs without showing how they arrived at a particular design. In Article III, the design process is highlighted. The flow around two sets of ADs, one with a uniform design and one with a non-uniform design, is compared to the flow around a rotating wind turbine model. The uniform disks were perforated disks, similar to the one used by Sforza et al. (1981) while the non-uniform disks have a design inspired by the disk used by Camp and Cal (2016; 2019). The disk that most closely replicates the flow field around the wind turbine is then used to compare different aspects of the flow in detail.

[1]The present author also co-authored this study.

4. *Can actuator disks be used to give a good representation of the flow in the induction and entrance regions of a wind farm?*

While there are several comparisons between ADs and wind turbines as single WGOs, only Camp and Cal (2016; 2019) make the comparison in a wind farm. They used a small farm of four rows and measured around the WGO in the center of the final row. Still, they focused on the flow around a single WGO, but with a wind farm inflow. As such, there are no studies investigating how an AD replicates the wind turbine flow in a wind farm's induction and entrance regions.Article IV does this for farms consisting of 69 rotating turbine models and 69 ADs. The ADs used here are the ones giving the best match to the turbines in Article III. The comparison is performed over three different incoming wind directions for staggered and aligned farm layouts. To date, this is the most comprehensive study comparing the flow around ADs and wind turbine models in a wind farm. Furthermore, it is an extensive study of the wind farm induction region.

Chapter 2

Theory

The general description of fluid motion is a complex problem. It is governed by the Navier-Stokes equations. However, in most real-world phenomena, the non-linearity of the equations makes them nearly impossible to solve analytically. Therefore, the fluid motion must be studied by other means, e.g., experimentally. Different quantities are used to describe the velocity, turbulence, and rotation of the flow. In this chapter, the quantities studied in the thesis will be introduced. Some are assumed to be well known and will only be introduced briefly, while others will receive more attention.

Many real flows are turbulent, that is, there is chaotic behavior in the flow. In short, turbulent flows consist of eddies, or swirls, over a range of scales. The motion of the eddies appears to be random and chaotic. A description of turbulent flows and how to quantify them can be found in Pope (2000). The basis of the description of turbulent flows is the Reynolds decomposition, where the instantaneous velocity $u(t)$ is decomposed as

$$u(t) = U + u'(t), \tag{2.1}$$

where $U = \overline{u(t)}$ is the time-averaged component and $u'(t)$ is the fluctuating component. The t indicates the time instance of a data-point, and the overbar indicates the time-average of a quantity. This can be done for the three velocity components u, v, and w, but is for simplicity limited to only u here. The mean velocity can be considered to be the most basic way of describing a flow field.

2.1 Vorticity and swirl

One key quantity of a flow field is the magnitude of rotation. The vorticity, defined as $\vec{\omega} = \nabla \times \vec{u}$, is a measure of the local rotation of the fluid. By only considering

two-dimensional data, this equation is reduced to

$$\omega_z = \frac{\partial v}{\partial x} - \frac{\partial u}{\partial y}, \tag{2.2}$$

or equivalent depending on the out-of-plane direction. Instantaneous structures of strong vorticity can identify important features of a flow field, for example tip-vortices in the wake of a wind turbine. To isolate the vortex cores, the signed swirling strength can be calculated according to the method outlined by Jeong and Hussain (1995),

$$\lambda = \frac{\frac{\partial v}{\partial x} - \frac{\partial u}{\partial y}}{\left|\frac{\partial v}{\partial x} - \frac{\partial u}{\partial y}\right|} \max\left\{0, -\left[\frac{\partial u}{\partial y}\frac{\partial v}{\partial x} - \frac{1}{2}\frac{\partial u}{\partial x}\frac{\partial v}{\partial y} + \frac{1}{4}\left(\left(\frac{\partial u}{\partial x}\right)^2 + \left(\frac{\partial v}{\partial y}\right)^2\right)\right]\right\}, \tag{2.3}$$

where the first fraction identifies the sign of the vorticity at the given point and the expression inside max $\{\cdots\}$ determines the strength of a vortex core.

2.2 One-point turbulence statistics

While turbulence is hard to define, it can, to a large extent, be described by statistical quantities. One-point statistics give information about the flow without taking the order in which velocity events occur into account. It should be noted that when the data is resolved in time, and not in space, the theory is applied to temporal rather than spatial data, which can be done based on Taylor's "frozen turbulenc" hypothesis. As such, it is in reality one-time and not one-point statistics. To include the evaluation of the order of events, two-point, or two-time, statistics are needed. The description of the one- and two-point statistics will partly follow earlier descriptions by Morales et al. (2011) and Neunaber et al. (2021).

The amount of turbulence in the flow is often the second statistical quantity, after the mean velocity, used to describe a turbulent flow. This can be done by calculating the TI, which is the strength of the turbulence relative to the mean velocity. TI is often calculated for a single velocity component, for example as σ_u/U, where σ_u is the standard deviation of the first velocity component. Note that, for flow measurements, the standard deviation is a feature of the flow and not a quantification of uncertainty. It should be commented that in Articles I and II, the standard deviation is denoted as u', but to avoid confusion with the fluctuating velocity component, σ_u is used in the preamble of the thesis. To visualize the difference between high and low turbulence, a low TI velocity signal is shown in panel a) and a high TI velocity signal is shown in panel b) of Figure 2.1.

Sometimes it is also interesting to know the amount of turbulence in the flow independent of the mean velocity. For this, the turbulent kinetic energy in the flow can

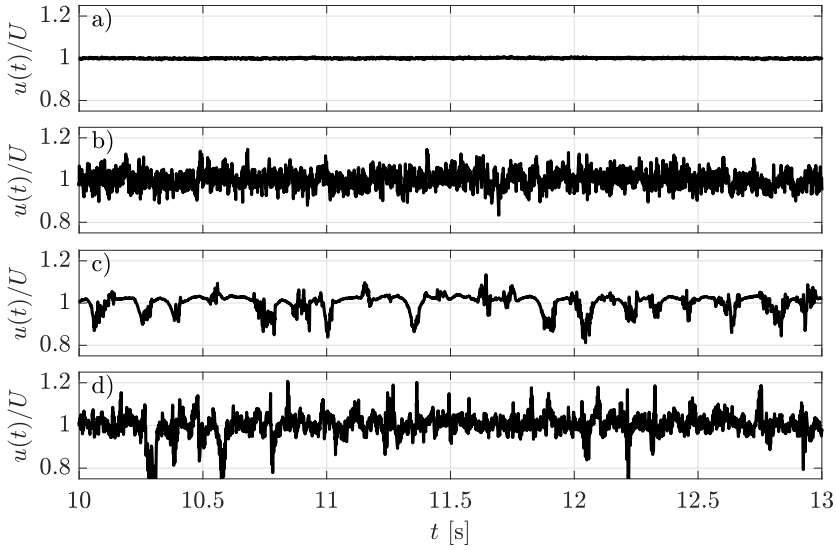

Figure 2.1: Time series of the velocity in a) a low-turbulent flow, b) a high-turbulent flow, c) a low-turbulent intermittent flow, and d) a high-turbulent intermittent flow. All the time series were acquired in the wake of an actuator disk as a part of this thesis.

be calculated as

$$k = \frac{1}{2}\left(\overline{u'^2} + \overline{v'^2} + \overline{w'^2}\right), \tag{2.4}$$

or a 1- or 2-dimensional surrogate if fewer velocity components are known. The three components in Equation 2.4, $\overline{u'^2}$, $\overline{v'^2}$, and $\overline{w'^2}$, referred to as the normal Reynolds stresses, are measures of the amount of turbulent energy in the flow. The key terms for turbulence energy production are the Reynolds shear stresses, that is, the correlations between the velocity fluctuations in different directions. Again, 2-dimensional measurements leaves only the $\overline{u'v'}$-term, with the velocity components depending on the coordinate system.

It is also of interest to know more about the nature of the fluctuating velocity components. For that purpose, the skewness, S, and flatness, F, (sometimes referred to as the kurtosis) are useful quantities. They are defined as

$$S(u) = \overline{u'^3} \Big/ \left(\overline{u'^2}\right)^{3/2} \tag{2.5}$$

and

$$F(u) = \overline{u'^4} \Big/ \left(\overline{u'^2}\right)^{2}, \tag{2.6}$$

respectively. In short, these two quantities describe the shape of the probability density function (PDF) of the fluctuations of a velocity time series. Positive skew-

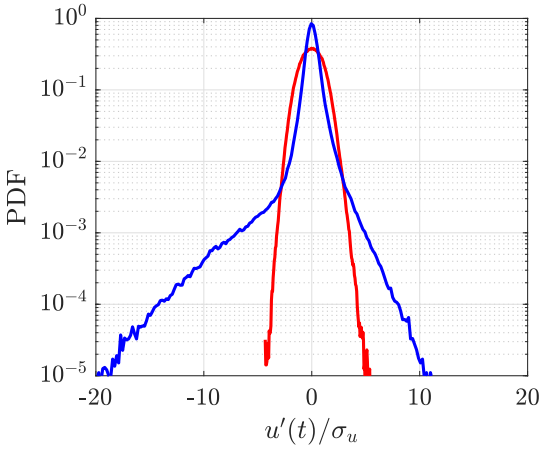

Figure 2.2: Probability density functions of velocity fluctuations for turbulence close to a Gaussian distribution (red) and turbulence with negative skewness and high flatness (blue). Both are original measurements, taken in the center and at the edge of an actuator disk wake, respectively.

ness means that high speed velocity fluctuations are more pronounced than low speed fluctuations, and vice versa for negative skewness. The flatness is a quantification of the probability of extreme events. A narrow PDF with heavy tails has a higher flatness value than a wider PDF with short tails, and thus implies that there are many extreme velocity events in the flow. A Gaussian distribution is symmetric, that is $S = 0$, and has a flatness of $F = 3$. To illustrate the effect of skewness and flatness on the PDF, Figure 2.2 shows PDFs of two velocity fluctuation signals, one close to a Gaussian distribution and one with negative skewness and high flatness. The non-Gaussian PDF has stronger tails compared to the Gaussian PDF, illustrating the high flatness of the velocity fluctuations. Furthermore, the negative tail is clearly more prominent than the positive tail, which shows that this profile has negative skewness.

2.3 Two-point turbulence statistics

While the analysis with mean velocity, TI, skewness, and flatness give a detailed description of the velocity fluctuations in a velocity signal, an analysis with two-point statistics is needed to include the order in which velocity events occur. The energy spectral density of the velocity fluctuations, E_{11}, here referred to as the velocity spectrum, gives information about energy content of structures in the flow. In particular, it shows energy content at different frequencies. The subscript *11* denotes that the *u*-component of the velocity is used to calculate the velocity spectrum. The velocity spectrum is derived using the Fourier transform of the auto-

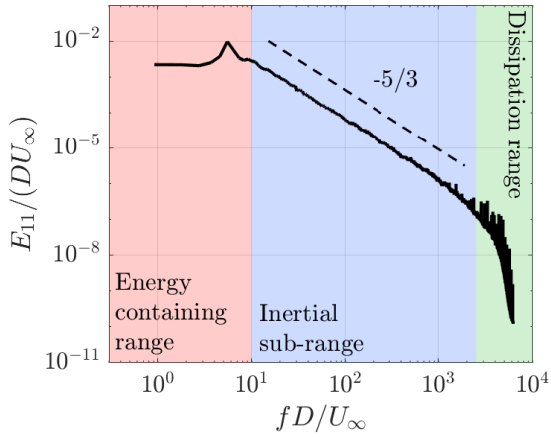

Figure 2.3: An example of an energy spectral density of velocity fluctuations for a hot-wire measurement taken in the wake of a solid disk as a part of this thesis.

correlation function of the velocity fluctuations. Figure 2.3 shows an example of a velocity spectrum, with color-coding to show different domains of the spectrum. In the dissipation range, turbulent kinetic energy dissipates to heat. The inertial sub-range approximately follows the -5/3 power-law if the flow is sufficiently turbulent (Kolmogorov 1941). The energy is transported from larger to smaller eddies (Richardson 1922). For the case of the -5/3 power-law, the energy cascade is in equilibrium. However, for the work in this thesis, the analysis is mainly limited to the energy-containing range to identify significant energy-carrying structures in the flow. They are often set by the boundary conditions of the flow, for example, wind turbines. In the spectrum in Figure 2.3, the peak in the energy containing range is an example of large-scale structures arising due to obstacles in the flow, as it shows the frequency at which vortex shedding is observed in the wake of a solid disk.

The other feature investigated by two-point statistics in this thesis is the intermittency, or gustiness, of the flow. Intermittency is a measure of the presence of extreme events in the flow. Examples of time series of intermittent flows are shown in panels c) and d) in Figure 2.1. For panel c), the flow is low-turbulent with intermittent turbulent bursts, while in panel d) the background flow is turbulent, but still with extreme events occurring through the time series. The central velocity increment is defined as

$$\delta u_\tau = u(t + \tau/2) - u(t - \tau/2), \tag{2.7}$$

where τ is a time scale separating two velocity events. The structure functions,

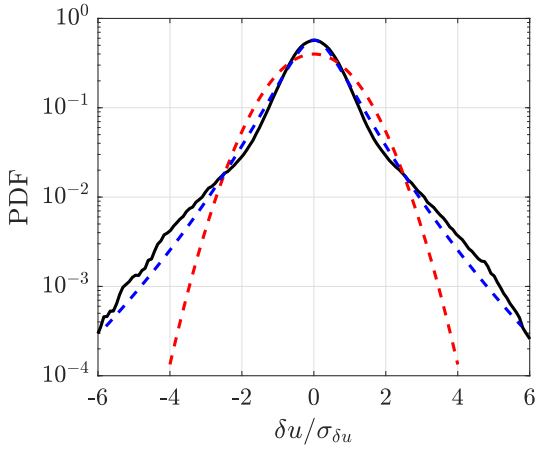

Figure 2.4: The probability density function of the velocity increment at a chosen time lag τ for the velocity signal shown in Figure 2.1d. The data is taken from the wake of an actuator disk as a part of this thesis. The dashed lines indicate a Gaussian distribution based on the standard deviation of the velocity increment time series (red) and a Castaing distribution based on the calculated shape parameter λ^2 (blue).

or the moments of the velocity increment $\overline{\delta u_\tau^n}$, can be used to study intermittency. However, in this thesis, the PDF of the velocity increments will be used. A deviation from the Gaussian distribution, particularly the occurance of heavy tails, will indicate an intermittent flow. The PDF of the velocity increment for a chosen τ of the time series in Figure 2.1d is shown in Figure 2.4. The heavy tails of the distribution show that the flow is intermittent at the time scale τ.

The PDF of the velocity increment gives the full information of the two-point statistics of the flow. However, it can only be plotted for one τ at one position at a time. To evaluate intermittency at several scales and also several positions, it is for practical reasons necessary to have a quantification of the intermittency. Castaing et al. (1990) derived the probability function

$$p\left(\delta u_\tau\right) = \frac{1}{2\pi\lambda(\tau)} \int_0^\infty \frac{\mathrm{d}\sigma}{\sigma^2} \exp\left[-\frac{\delta u_\tau^2}{2\sigma^2}\right] \exp\left[-\frac{\ln^2\left(\sigma/\sigma_0\right)}{2\lambda^2(\tau)}\right], \tag{2.8}$$

which superimposes a range of Gaussian distributions weighted by a log-normal distribution. The parameter σ_0 is given by Beck (2004) as

$$\sigma_0^2 = \overline{\delta u_\tau^2} \exp\left[-2\lambda^2(\tau)\right]. \tag{2.9}$$

Then the only remaining free parameter in Equation 2.8 is $\lambda^2(\tau)$, the shape parameter, which is a measure of the deviation of $p\left(\delta u_\tau\right)$ from a Gaussian distribution.

It is not trivial to fit the PDF to find the correct value for $\lambda^2(\tau)$. However, Chillà et al. (1996) introduced an explicit expression for the shape parameter,

$$\lambda^2(\tau) = \frac{\ln\left(F\left(\delta u_\tau\right)/3\right)}{4}. \tag{2.10}$$

This approximation rests on several assumptions, for example that the turbulence is fully developed (Chillà et al. 1996). A non-intermittent flow does not have a PDF of δu_τ^2 that deviates from a Gaussian distribution, and as such it has $\lambda^2 = 0$, while an intermittent flow has $\lambda^2 > 0$. As a final note on the intermittency of the flow, it should be mentioned that $\lambda^2(\tau)$ only gives a measure of the extent of extreme events relative to the "normal" fluctuations in the flow. As such, a highly intermittent, low TI flow can have extreme events that are smaller than the turbulent fluctuations of a non-intermittent, high TI flow.

2.4 Proper orthogonal decomposition

The one-point and two-point statistics discussed in the previous sections deal with time series from point measurements. A vast region of homogeneous, isotropic turbulent flow would be required to apply the same methods to spatially resolved data. Still, it is possible to evaluate structures in the flow from smaller spatial domains by performing a modal decomposition. A popular method for such a decomposition is the snapshot proper orthogonal decomposition (POD) developed by Sirovich (1987). This section will introduce the procedure to perform snapshot POD. For this thesis, only two velocity components, u and v or u and w, will be considered at a time.

Every instantaneous velocity field, either the full measured field or a chosen region of interest, is considered to be a snapshot of the flow. The snapshots are numbered as $n = 1, 2, \cdots, N$. Each snapshot consists of the same number, M, of velocity vectors. The first step is to create a matrix consisting of all the fluctuating velocity components,

$$\mathbf{U} = \begin{bmatrix} \mathbf{u'}^1 & \mathbf{u'}^2 & \cdots & \mathbf{u'}^N \end{bmatrix} = \begin{bmatrix} u'^1_1 & u'^2_1 & \cdots & u'^N_1 \\ \vdots & \vdots & \ddots & \vdots \\ u'^1_M & u'^2_M & \cdots & u'^N_M \\ v'^1_1 & v'^2_1 & \cdots & v'^N_1 \\ \vdots & \vdots & \ddots & \vdots \\ v'^1_M & v'^2_M & \cdots & v'^N_M \end{bmatrix}, \tag{2.11}$$

where each column contains the velocity data from one snapshot. Each row then consist of the same velocity component, at the same position, from the different snapshots. From this, the autocovariance vector

$$\widetilde{\mathbf{C}} = \mathbf{U}^T\mathbf{U} \tag{2.12}$$

is created, and the corresponding eigenvalue problem

$$\widetilde{\mathbf{C}}\mathbf{A}^i = \lambda^i \mathbf{A}^i \tag{2.13}$$

is solved. The eigenvectors, $\mathbf{A}^i$, are then used to construct the POD modes as

$$\mathbf{\Phi}^i = \frac{\sum_{n=1}^{N} \mathbf{A}_n^i \mathbf{u}'^n}{\left|\left|\sum_{n=1}^{N} \mathbf{A}_n^i \mathbf{u}'^n\right|\right|}, \quad \text{for } i = 1, 2, \cdots, N. \tag{2.14}$$

The modes are sorted by their energy content, that is, the value of the corresponding eigenvalue λ^i, such that the most prominent flow structures are visible in the first modes. These structures correspond to the features in the energy containing range of the velocity spectrum, for example, the vortex shedding seen in the peak in Figure 2.3.

It is possible to use the POD modes to perform reduced order modelling of the flow field. With this method, the number of modes used for the modelling can be reduced to the most energetic ones, reducing the complexity of the problem. The reconstruction can be done by

$$\mathbf{u}'^n = \sum_{i=1}^{N} a_i^n \phi^i, \tag{2.15}$$

where a_i^n are the POD coefficients. This equation also illustrates that the magnitude and sign of the vectors in a POD mode are only important relative to the other vectors in the mode. A change in the magnitude and sign for the entire mode is easily compensated for by the POD coefficients.

Chapter 3

Methodology

This chapter introduces the equipment and techniques used in the different articles. First, the ADs, wind turbines, and facilities will be described before attention turns to the measurement techniques.

3.1 Equipment

3.1.1 Actuator disks

200 mm disks

In total, three different disks were used in Articles I and II. All the three disks have diameters $D = 200$ mm and were mounted to a tower with a diameter of 10 mm. This thin tower was mounted to a thicker tower to raise the disks to the center of the wind tunnel. A cable was wound around the thicker tower to act as a vortex disruptor (Fox et al. 2016). A long try square, reaching the wind tunnel wall, was used to ensure that the disks directly faced the incoming flow.

The solid disk (SD) was cut from a plywood sheet with a thickness of 9 mm. As expected for a solid disk, the thrust coefficient of this disk was $C_T = 1.1$ (Çengel and Cimbala 2014). Note that the thrust coefficient is usually called the drag coefficient when objects other than wind turbines are considered. The wake of the SD was used as a reference for the ADs in Article I.

The two ADs are a uniform disk (UD) and a non-uniform disk (ND), both with a solidity of 57%. In Articles I and II they are referred to as the porous disks. Figure 3.1 shows schematics of the two ADs. The UD is cut from a wire mesh with a wire thickness of 0.8 mm and is the same as the one used by Aubrun et al. (2019). The ND was machined from a 5 mm thick acrylic sheet. The design is

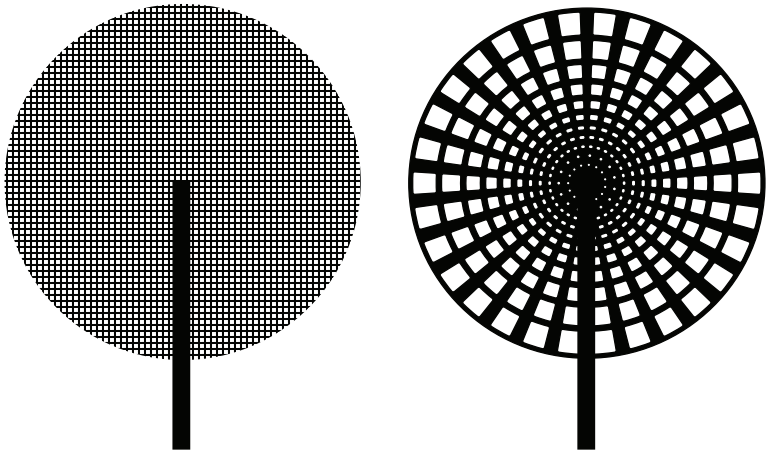

Figure 3.1: The uniform disk (left) and non-uniform disk (right) used in Articles I and II.

inspired by the AD used by Camp and Cal (2016; 2019), which was also the non-uniform AD used by Aubrun et al. (2019), but by changing the number of spars and rings and their dimensions, it was modified to match the size and blockage of the UD. The thrust coefficients of the UD and ND were measured to be $C_T = 0.77$ and $C_T = 0.82$, respectively, which was judged to be sufficiently similar for the purpose of the present experiments.

45 mm disks

The different disks used in Article III had a diameter of $D = 45$ mm and a thickness of 2.5 mm. The size was chosen to be sufficiently small such that they could be used in the wind farm experiments presented in Article IV. The disks were 3D-printed with polylactic acid (PLA) using an Ultimaker 2+. They are connected to towers through a nacelle, both with a diameter of 3 mm, which were mounted to the mounting bar by magnets (see description in Article III for details).

In total, the flow around six different disks was measured. Schematics of the different disks are shown in Figure 3.2. The first disk is a solid disk used as a reference. Furthermore, there are two ADs with uniform blockage. They are perforated disks, similar to the ones used by Sforza et al. (1981) rather than wire mesh disks as used in Articles I and II. The uniform disks are called uniform holes disks (UHDs). There are also three ADs with non-uniform blockage, named the non-uniform holes disks (NHDs). They are, like the ND, based on the design used by, for example, Camp and Cal (2016; 2019). Both AD designs were designed with blockages of 60% and 40%, and for the NHD design also 35% was used. It was not possible to manufacture a UHD with 35% and still keep a solid circumference. The lack of a solid

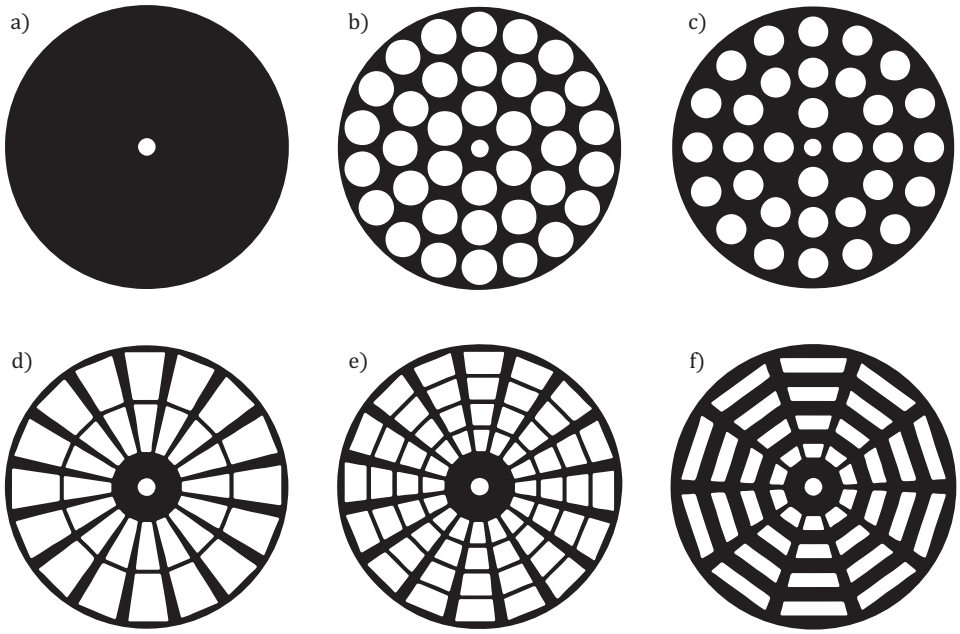

Figure 3.2: The different disks used in Article III: a) Solid, b) UHD40, c) UHD60, d) NHD35, e) NHD40, and f) NHD60. The NHD35 was also used in Article IV.

circumference would lead to different flow separation; therefore, that design option was kept out of the scope of this work. The naming convention for the disks is the disk type followed by the disk's blockage. The disk that was chosen to be used in Article IV is, for example, named NHD35.

3.1.2 Wind turbines

200 mm wind turbine

The three-bladed wind turbine depicted in Figure 3.3 was used in Article I. The diameter of the turbine is $D = 200$ mm. The blades have a NACA 63-418 airfoil profile along the entire length. The turbine is designed to operate at a TSR of 3.5. To achieve a constant angle-of-attack of $\alpha = 12°$ along the blade the geometrical pitch angle ranges from $\theta = 39.57°$ at the hub to $\theta = 0.73°$ at the tip. The chord length of the airfoil changes from 25 mm at the hub to 12.5 mm at the tip. The blades are connected to a 22 mm diameter hub. The blades and the hub were 3D-printed with a stereolithography printer.

The wind turbine rotor was mounted directly on the shaft of a permanent magnet direct current (DC) machine that acted as the generator of the wind turbine. The motor did not receive electrical power from any external source. A metal-oxide-

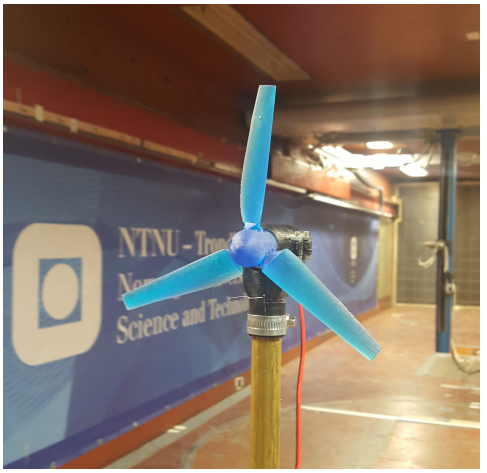

Figure 3.3: The three-bladed wind turbine used in Article I.

semiconductor field-effect transistor (MOSFET) was used to control the speed of the DC machine. It operates by opening and closing the electrical connection between the machine poles. The rotational speed under constant loading is determined by the time ratio between the open circuit and close circuit operation. A proportional integral derivative (PID) controller implemented on an Arduino Uno sets this ratio. The rotational speed is recorded by an encoder installed on the generator. It is equipped with a codewheel with 500 counts per revolution. The angular velocity is computed by counting the number of rising edges on the encoder signal for 0.25 s. The generator, encoder, and wiring were enclosed in a nacelle that was 3D-printed with PLA.

Measurements of the current generated by the machine are obtained with a 0.1 Ω shunt resistor, whose voltage drop is sampled by a 12-bit analog to digital converter and related to the current via Ohm's law. From the current it is possible to estimate the torque the DC machine experiences (Q_{sh}) through the relationship

$$Q_{sh} = K_T I + Q_f(\omega_r), \tag{3.1}$$

where I is the measured current, Q_f is the torque lost to friction, and K_T is a proportionality constant. It is assumed that the frictional losses are only dependent on the rotational speed ω_r. For more details on this procedure, see Gambuzza and Ganapathisubramani (2021), who used a similar set-up on a different wind turbine. From the torque estimate, the power coefficient C_P of the turbine can be calculated through

$$C_P = \frac{Q_{sh}\omega_r}{1/2\rho {U_\infty}^3 A}. \tag{3.2}$$

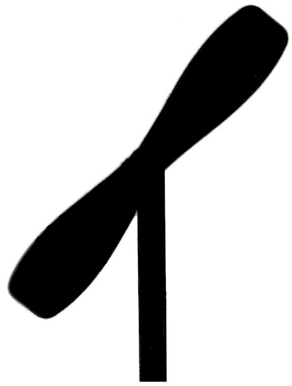

Figure 3.4: The small rotating model used in Articles III and IV.

45 mm rotating wind turbine models

The rotating models used in Articles III and IV have previously been used in works by Ebenhoch et al. (2017), Segalini and Dahlberg (2020), and Segalini and Chericoni (2021). They are referred to as rotating models rather than wind turbines as they, in contrast to the three-bladed wind turbine, do not produce power but rather rotate freely. The two blades are flat, twisted plastic sheets, and the rotors were industrially manufactured, originally intended as drone propellers. The diameter of the rotors is $D = 45$ mm, and the rotor is shown in Figure 3.4. The models rotate at a TSR of approximately five (Segalini and Dahlberg 2020), but this depends on the bearing friction and may vary between the turbines. Each rotating model is connected to a nacelle and tower with the same dimensions as for the small ADs, and was also mounted similarly.

3.2 Facilities

The main facility used in the work for this thesis is the large closed-loop wind tunnel at the Department of Energy and Process Engineering (EPT) at the Norwegian University of Science and Technology (NTNU). Schematics of the facility are shown in Figure 3.5. It is driven by a 220 kW radial fan located downstream of the test section and controlled by a variable frequency drive (VFD). The maximum freestream velocity of the test section is approximately 23 m/s. The flow is conditioned through an expansion chamber, including guiding vanes and three screens. After the expansion chamber, guiding vanes are used to turn the flow to meet the test section. Final conditioning is done through a honeycomb, another screen, and a contraction with an area ratio of 4.2:1. Any further flow conditioning is described in the respective papers.

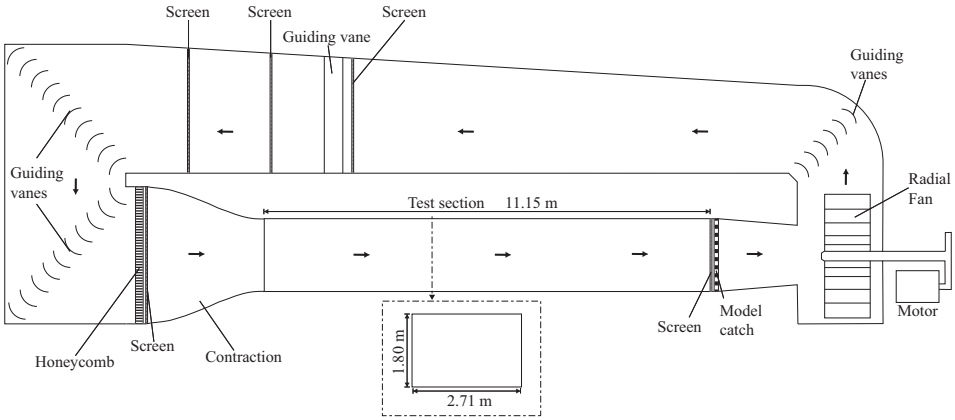

Figure 3.5: Schematics of the large closed-loop wind tunnel.

The test section has dimensions of 11.15 m × 2.71 m × 1.8 m (length × width × height). The height increases to 1.85 m at the end of the tunnel to compensate for the growing boundary layers such that the streamwise pressure gradient is approximately zero. It was constructed from plywood with glass windows on one wall, but during this thesis, it was renovated to have optical access from three sides; a glass floor, acrylic walls, and an acrylic roof. This renovation has been a significant part of the thesis. Nevertheless, the experiments performed for Article I and Article II were performed before this renovation. The experiments in Article IV were done in a partly refurbished tunnel, with the measurement location located in a renovated part of the tunnel, with optical access through the roof and side wall.

The experiments for Article III were performed in a smaller closed-loop wind tunnel on the same grounds. It has dimensions of 7 m × 1 m × 0.5 m (length × width × height) and a maximum velocity of 35 m/s. The velocity is controlled by vanes which can be opened or closed to increase or reduce the velocity. The wind tunnel is made of plywood but has a few windows for optical access. The walls expand downstream of the test section before the flow is directed around two corners. Here, the fan and another expansion chamber are located. The flow is then guided back to the test section through two corners and a contraction with an area ratio of approximately 3:1.

3.3 Experimental methods

HWA, force measurements, and PIV are the main measurement techniques used for this thesis. Before introducing those, a brief introduction about recording the experimental conditions will be given. It is more or less the same for all experiments.

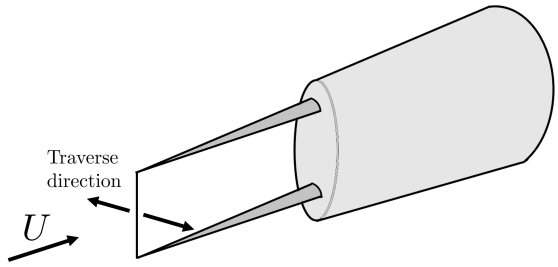

Figure 3.6: Schematics of a single-wire probe.

First, the pressure and temperature are needed to calculate the viscosity and density of the air. The atmospheric pressure was recorded with a mercury barometer, typically at the beginning and end of each measurement day. The temperature was recorded at the same time. This data was used for equipment calibration, or an average for the day was used to find the fluid properties. Secondly, the wind tunnel velocity was monitored using a pitot-static tube. The dynamic pressure was converted to voltage through a pressure transducer before it was calculated back to the values in Pascal. From this, the flow velocity can be calculated by $\Delta P = 1/2\rho U^2$, where ΔP is the dynamic pressure recorded by the pitot-static tube.

3.3.1 Hot-wire anemometry

HWA is a measurement technique used to measure the flow velocities at single points. It has a rapid response time, allowing for time-resolved measurements of the flow. As such, it is a well-suited method to measure turbulent statistics. In Articles I and II, the hot-wire was kept at a constant temperature, a method called constant temperature anemometry (CTA). This section will describe the principles of that particular method before giving details on the specific set-up used.

The hot-wire itself is a thin and short wire connected to a small probe. Schematics of a single-wire probe are shown in Figure 3.6, with the wire shown as a vertical line at the end of the prongs. It is heated to a constant temperature and thus constant resistance, and the voltage required to maintain that temperature is recorded. The required voltage is a measure of the flow velocity, as the convection of heat to the passing air depends on the flow speed. It is necessary to calibrate the hot-wire with other flow measurements to get the correct velocity. If the air temperature varies through the measurements, it is also required to include correction for the temperature drift. A single-wire is not sensitive to the direction of the flow as it is not able to distinguish between velocity components normal to the wire.

In this thesis, hot-wires of the type Dantec 55P11 were used for simultaneous

sampling. They are tungsten wires with a diameter of 5μm and a length of 1.25 mm. The wires were aligned with the vertical axis, normal to the incoming flow and the traversing direction (as indicated in Figure 3.6). The measured velocities were therefore the total velocity in the horizontal plane, while the vertical velocity was not measured. Dantec 55H21 probe holders were used to position the wires, and the wires were moved to the different measurement positions by a traversing mechanism permanently installed in the wind tunnel. The probe holders were connected to a Dantec StreamLine Pro CTA-unit. The voltage is measured over a Wheatstone bridge, where the hot wire is one of the arms. The temperature in the wind tunnel was recorded by a K-type thermocouple. At the start of the experimental campaign, a Dantec 55H30 shorting probe was used such that the resistance of the set-up without the hot-wires themselves could be measured, yielding one "cable and support"-resistance for each of the wires.

The resistance, including the hot-wires, was measured daily to be used throughout that day. Offset and gain were applied to the voltage signal to utilize the span of the $\pm$10 V range of the differential voltage module. The hot-wires were operated with an overheat ratio of 1.8 compared to the wind tunnel temperature recorded at the time of the daily resistance measurements. The sampling frequency of the experiments was kept at 30 kHz, with an analog low-pass filter applied at 10 kHz. The Kolmogorov frequency of the measured flows was found to be well below 10 kHz, so this sampling frequency was sufficient to capture the complete temporal turbulent statistics.

The hot-wire probes were calibrated with velocity measurements from a Pitot-static tube mounted beside the hot-wires. To include temperature corrections the procedure of Hultmark and Smits (2010) was used. The voltage is then related to the velocity through

$$\frac{U}{\nu} = f\left(\frac{E^2}{k_T \Delta T}\right), \tag{3.3}$$

where ν is the kinematic viscosity, E is the measured voltage, ΔT is the temperature difference between the wire and the ambient flow, and k_T is the thermal conductivity of air, given as $k_T = 418.4\left(5.75 \times 10^{-5}\left(1 + 0.00317T - 0.0000021T^2\right)\right)$ by Kannuluik and Carman (1951). Twelve different flow velocities were used in the calibration, covering the range of expected velocities, including the high-velocity turbulent fluctuations. The function f in Equation 3.3 was found using a fourth-order polynomial fit. Figure 3.7 shows the fit and the measurement points for two calibrations taken on an arbitrary day of the experimental campaign, one before starting measurements in the morning and one after finishing the measurements of the day. An average of the first and second calibration, weighted by the time between them, was used for each individual measurement. As Figure 3.7 shows,

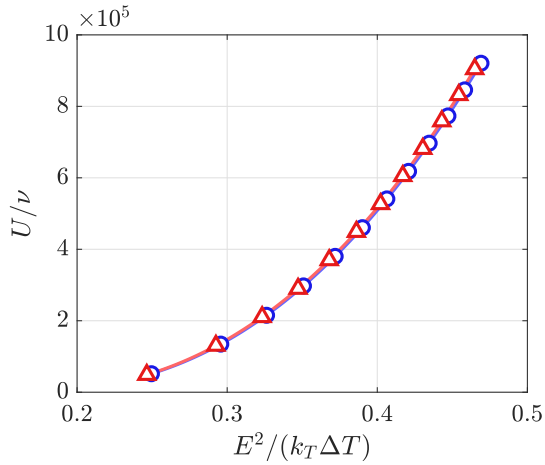

Figure 3.7: Hot-wire calibration curves for the calibrations at the start (blue) and end (red) of a measurement day. The solid lines are the curve fits to the calibration points marked by symbols.

the drift of the wire over a day is relatively small, justifying this procedure.

Finally, a digital filter was applied to the time series at the Kolmogorov frequency. The Kolmogorov length, η, is found through an iterative scheme estimating it from a temporarily filtered velocity signal by the equation

$$\eta = \frac{\nu^{3/4}}{\left(15\nu\overline{\left(\frac{\partial u}{\partial x}\right)^2}\right)^{1/4}} \tag{3.4}$$

until it has converged. The Kolmogorov frequency is then found by using Taylor's hypothesis. In this procedure it is assumed that the turbulence is locally isotropic (Pope 2000).

The uncertainty was calculated by the method given in Benedict and Gould (1996) and was less than 1% for the mean velocity in turbulent flow regions. This method of estimating the uncertainty does not work well in low-TI flow due to difficulties associated with estimating the integral time scale. For the higher-order statistics, the uncertainty is more prominent, particularly for the skewness and flatness in the outermost parts of the wake. This uncertainty is illustrated in the large scatter in the flow profiles and stems from the relatively few uncorrelated velocity events.

3.3.2 Force measurements

Force measurements were conducted to determine the drag of the different WGOs used in Article III. The method is described in that paper, but a summary will be given here. An AMTI BP400600HF 1000 force plate was used for the measurements. The voltage signal was amplified before a low-pass filter with a cut-off frequency of 1000 Hz was applied. Only one component, the streamwise force, was interesting for the current work. To reduce the uncertainty associated with the drift of the load cell, reference measurements were taken in quiescent flow before and after every single force measurement. The zero-measurement that was subtracted from the measured force was then calculated as a time-based weighted average from the two tare measurements.

3.3.3 Particle image velocimetry

PIV is an optical measurement technique used to capture two-, or sometimes three-dimensional, velocity fields in a plane or small flow volume. In addition to giving spatial information about the flow, one of the main advantages of the technique is that it is non-intrusive as it does not have any physical objects in the flow. In this thesis, only two-dimensional, two-component (2D2C) PIV has been used, and the discussion will be focused on that method. For a broader overview of different methods and a more thorough understanding of PIV, see the textbook by Raffel et al. (2018). The PIV set-ups used in Articles III and IV are different, so this introduction to the method will be general and not go into details of the specific set-ups. The reader is referred to the experimental method sections of the articles for details.

The PIV set-up consists of at least one light source, seeding source, and camera. Through a series of lenses, the laser beam is focused into a sheet covering the measurement plane. Two laser pulses, separated in time by Δt, illuminate the particles in the flow. For PIV, the particles size should preferably be larger than the pixel size in the images. This is often not possible in air, where the particle size typically is of the order 1 μm to 10 μm. The camera captures two images, one with the first laser pulse and one with the second. This leads to a pair of images displaying particles, or clusters of particles. Figure 3.8a shows snippets of a pair of particle images separated by Δt.

In order to extract the velocity field, the images are divided into interrogation windows. An example interrogation window is marked in orange in Figure 3.8a. The location of the peak in the the cross correlation between an interrogation window pair indicates how far the particles have moved in the course of Δt (see Figure 3.8b), and hence gives the velocity vector in that interrogation window. This is done it-

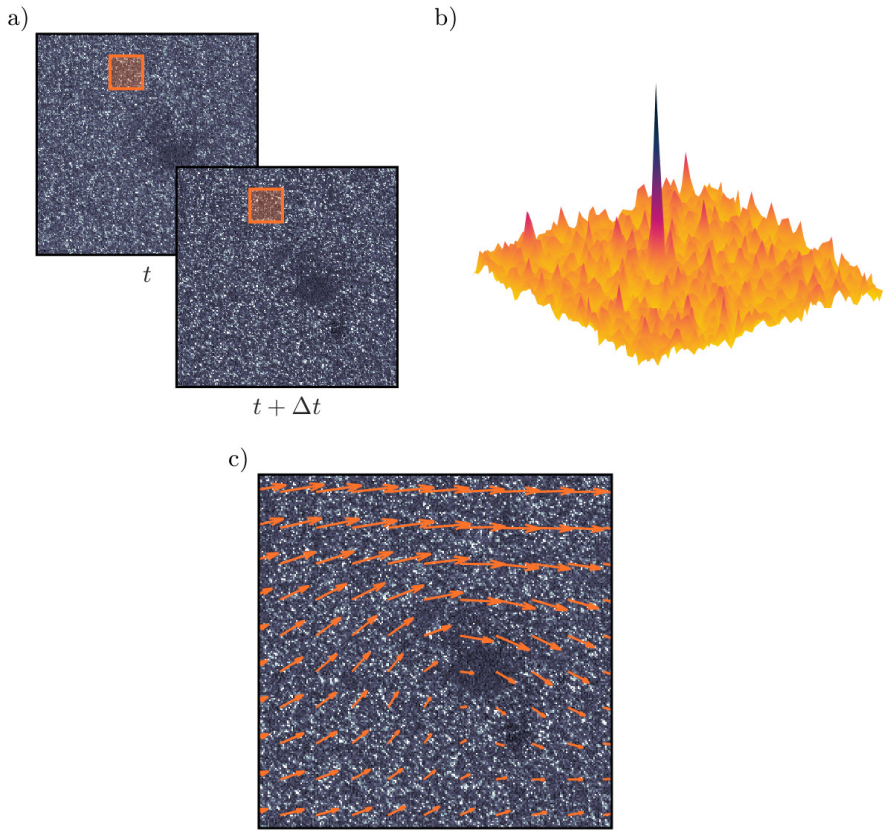

Figure 3.8: An illustration of PIV processing. a) Shows snippets from the two images in an image pair with an example interrogation window displayed in orange. b) Shows the correlation map for an interrogation window inside this field, displaying a clear peak indicating the movement of particles between the images in a). c) Shows the vector fields superimposed on the snippet from one of the raw images, displaying a clear vortex structure, in this case, a tip-vortex.

eratively on windows decreasing in size, with the final interrogation window being on the order of tens of pixels. Usually, some overlap is used between the interrogation windows. It should be emphasized that PIV correlates interrogation windows at two instances in time, but in contrast to particle tracking methods, it does not calculate the movement of individual particles. Combining all the interrogation windows, a velocity vector field is obtained. An example of a vector field is shown in Figure 3.8c, where it is plotted on top of one of the raw images. This particular snippet encapsulates a tip-vortex.

The quality of the PIV measurements is, to a large extent, shown in the uncertainty calculated by the software used (LaVision Davis 8), with the method given in Neal et al. (2015), Sciacchitano et al. (2015), and Wieneke (2015), which is based on the correlations. Other measures of the quality are the peak ratio, that is, the difference in the height between the two highest correlation peaks, and the correlation value which is the magnitude of the most prominent correlation peak. The typical uncertainty in the mean velocity is below 1%, which is the case for measurements in this thesis. The exact value typically depends on the amount of turbulence and vorticity inside each interrogation window. The uncertainty of the instantaneous velocities was below 0.5% in the undisturbed flow and below 5% in the turbulent wake. The calculated uncertainty, however, only estimates the random error associated with the experiments. Error sources contributing to the systematic uncertainty includes the alignment of the laser sheet and cameras.

In this work, where the PIV is not time-resolved, around 1000 image pairs are collected for each flow field. The sampling frequency is kept sufficiently low such that each image pair is uncorrelated to the one before and after and stands as an independent sample. The particle images are often pre-processed to improve the quality. Typically, both temporal and spatial filters are used to remove background noise.

For the experiments leading to Article IV several overlapping vector fields were acquired. A stitching algorithm was used in the overlap region to merge the sets of fields. First, to have a uniform grid of vectors, the second vector field is interpolated onto the grid of the first vector field. In the overlapping region, where there is data from both fields, a weighted average is used to find the velocity vector at each position. The weighting (w_s) is linearly based on the distance from the edge of the overlapping regions on both sides. The stitching process for instantaneous fields is illustrated in Figure 3.9.

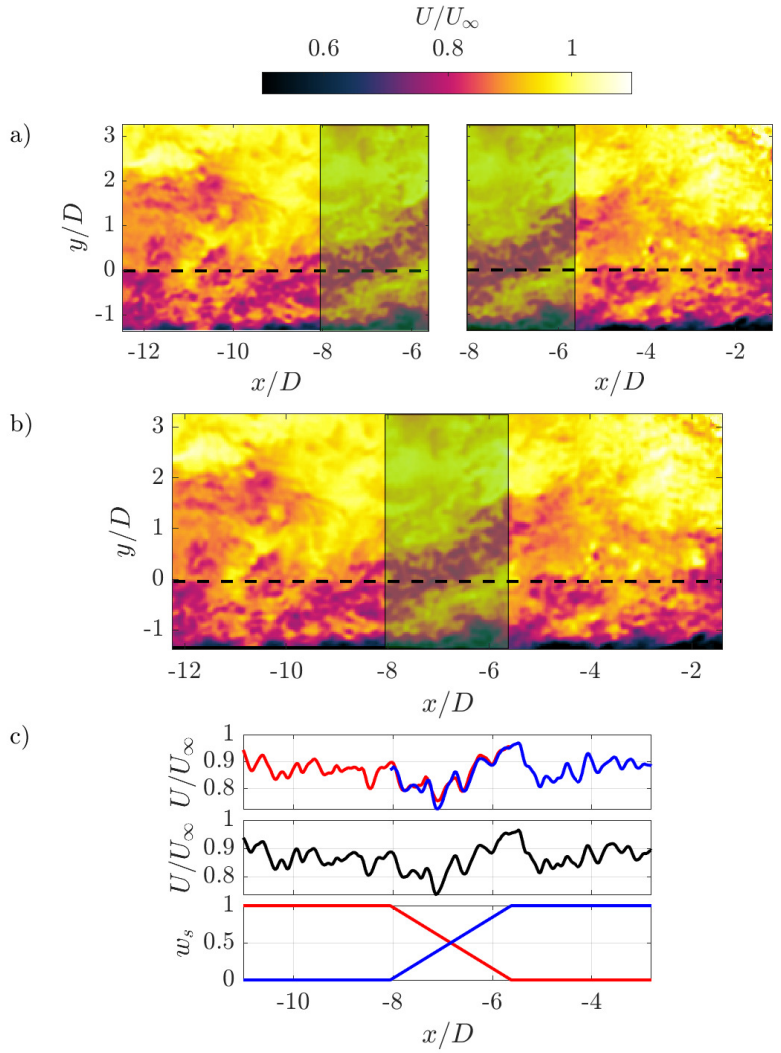

Figure 3.9: The stitching of instantaneous PIV fields. a) Two separate but overlapping velocity fields. The color map indicates the velocity magnitude. The green box illustrates the overlapping region. b) The stitched velocity field with the overlapping region in green. c) The velocity along the dashed lines in a) and b), with red and blue representing the first and second velocity field, respectively (top panel), and black coming from the stitched velocity field (middle panel). The bottom panel shows the weighting from each field in the overlapping region, with red and blue representing the first and second velocity fields, respectively.

Chapter 4

Summaries of the research articles and future work

4.1 Summary of articles

Article I

The far-wake of porous disks and a model wind turbine: Similarities and differences assessed by hot-wire anemometry

Magnus K. Vinnes, Stefano Gambuzza, Bharathram Ganapathisubramani, and R. Jason Hearst

Journal of Renewable and Sustainable Energy, **14**, 023304, (2022)

This article compares the wakes of two ADs with designs representative of those found in literature. One is a wire mesh disk with uniform blockage (UD), and the other one is a non-uniform acrylic disk (ND). Furthermore, the wakes of a solid disk and a wind turbine were included as reference cases. All the four WGOs have the same diameter. Hot-wire measurements were taken at several distances downstream, with the most downstream position being $30D$ downstream of the WGOs. The comparison was designed to answer the research question:

1. *How similar are the flows downstream of a uniform and a non-uniform actuator disk?*

The results show that neither of the ADs can reproduce the asymmetry in the wind turbine wake caused by the rotation of the blades. This asymmetry is evident in the skewness and flatness profiles, even in the far wake. While it is not surprising

that static disks are unable to reproduce features of a rotating wake, it is interesting to note how different the wakes downstream of the two ADs are. The wake of the ND recovers faster, displaying lower velocity deficits but a wider wake when compared to the UD wake. The UD wake retains a top-hat velocity deficit profile $3D$ downstream of the disk. There is thus little turbulence production in the center of the wake, yielding two peaks in the TI profile at the edges of the wake. These two peaks only meet $10D$ downstream. In contrast, the TI in the ND wake has a Gaussian profile near the disk, with a high maximum value in the center. However, from $10D$ downstream, the levels are smaller than for the UD. From this, it can be concluded that while there is strong production in the near-wake of the ND, leading to faster wake recovery, the strong withstanding gradients of the UD wake increase turbulence production farther downstream, yielding higher TI values in the far wake.

The mean profiles already show significant differences between the wakes. In addition, the velocity spectra reveal that there is vortex shedding in the ND wake and not in the UD wake. The UD wake contains lower frequency structures in the shear layer, which are associated with the shear layer instability. As such, there are significant differences in the governing physics of the two wakes, both for the one-point and the two-point statistics. The main conclusion from the article is that the wake of ADs are highly dependent on the design of the particular disk. Therefore, it is important to exercise care when choosing the design of an AD for experimental investigations.

Article II

Characterizing porous disk wakes in different turbulent inflow conditions with higher-order statistics

Magnus K. Vinnes, Ingrid Neunaber, Hauk-Morten H. Lykke, and R. Jason Hearst

Under consideration for publication in Experiments in Fluids

Expanding the work of Article I, Article II investigates the effect of ambient turbulence on the wake of the ADs. The experimental set-up is the same as in Article I, but a wooden bi-planar passive grid is used to increase the freestream TI. This addresses the second research question:

2. *How does freestream turbulence influence the wakes of a uniform and a non-uniform actuator disk?*

The results show that the increased freestream turbulence has more impact on the UD wake than on the ND wake. The wake recovery rate of the UD wake is enhanced, changing the shape of the velocity deficit and TI profiles at the closest

measurement positions. For both disks, the wake width and magnitude are altered by the freestream TI. The vortex shedding in the ND wake is still present, indicating that the wakes are still fundamentally different between the different ADs. The analysis of Article I is also expanded to include a description of the intermittency in the wakes of the two ADs. A region of highly intermittent flow is found to surround the wakes, increasing the effective wake size of both ADs. The intermittency ring is wider for low ambient TI, and for both inflow conditions, is more prominent for the ND wake. In sum, the enhanced background TI level makes the wakes more similar. Nevertheless, some of the governing physics of the flow are still different between the disks, particularly the vortex shedding observed in the ND wake.

Article III

A comparison of lab-scale free rotating wind turbines and actuator disks

Sanne de Jong Helvig, Magnus K. Vinnes, Antonio Segalini, Nicholas A. Worth, and R. Jason Hearst

Journal of Wind Engineering and Industrial Aerodynamics, **209**, 104485, (2021)

From Articles I and II, it is clear that the design process of an AD is important. To that end, the research question in focus for Article III is:

3. *How should an actuator disk be designed such that it replicates the flow field around a wind turbine?*

To answer this, the flow in the near-wake of two sets of ADs was measured by PIV. The two sets were designed with uniform and non-uniform blockages, as described in Section 3.1. Based on the mean velocity and the mean vorticity fields, the non-uniform disk with the lowest blockage (NHD35) was chosen for further examination.

As with the mean velocity and vorticity, the mean Reynolds stresses also agree reasonably between the disk and the rotating model, with differences mainly confined to within the first D downstream of the WGOs. However, instantaneous structures vary between the AD and turbine wakes. The signed swirl field reveals substantial instantaneous vorticity structures downstream of the AD, which are not present in the turbine wake. The turbine wake, however, contains the well-known tip-vortices, which cannot be replicated by the static AD. Through POD analysis, it is shown that the tip-vortices are a dominating feature of the flow, as they are the structures seen in the POD-modes with the highest energy content. The results show that, depending on the application, ADs can be used as static wind turbine models. Nevertheless, if detailed knowledge of the governing physics of the flow in the near-wake is desired, rotating wind turbines should be used.

Article IV

The flow in the induction and entrance regions of lab-scale wind farms

Magnus K. Vinnes, Nicholas A. Worth, Antonio Segalini, and R. Jason Hearst

Under consideration for publication in Wind Energy

The first three papers focus solely on single WGOs. As wind turbines are often grouped together in wind farms, the final article focuses on the difference in the flow field around ADs and rotating turbine models in a wind farm setting. This addresses the last research question of this thesis, which is:

4. *Can actuator disks be used to give a good representation of the flow in the induction and entrance regions of a wind farm?*

The flow around the induction and entrance regions of several wind farm layouts and alignments was measured to investigate this. The farms were built up of the same rotating wind turbine models used in Article III, as well as the NHD35 AD which was chosen as the best match in the same work. In the global induction region of the wind farms, there are no significant differences between the AD cases and the rotating model cases, and neither between the tested layouts and alignments. There is also reasonable agreement with the model proposed by Segalini (2021). In the local induction region of the most upstream WGO in the farm, however, the profiles differ between the different WGOs.

The same observations are made in the wake as well, consistent with the results from Article III. Looking at the wake of the second-row WGO for the aligned cases with the incoming flow parallel to the farm layout grid (the second-row WGO is not in the measurement field for the other cases), some of these differences are reduced. In particular, the POD modes show that the tip-vortices are not visible in the most energetic modes, and their impact on the flow physics is significantly reduced. The rapid break-down of the tip-vortices is ascribed to the higher TI in the incoming flow. This significant result shows that even though one should exercise care using ADs as wind turbine models, they might give valuable results, in particular when used in a wind farm where the high TI levels in the wakes of upstream WGOs enhance break-down of structures in the flow. How this affects the transport of mean kinetic energy from the flow above the farm cannot be derived from these results, as the measurements do not extend sufficiently deep into the wind farm. Over the first few rows, however, there is higher turbulence transport for the turbine models, but there are only minor differences in the transport by the mean vertical velocity between the different WGOs.

4.2 Future work

There are several ways to expand and build upon the results presented within this thesis. For Articles I, II, and III, the measurements were performed in idealized conditions, that is, in a uniform flow, and for Articles I and III also a low turbulent flow. The idealized conditions allowed identification of the main differences between the WGOs, but they do not include the complex flow where wind turbines usually operate. In particular, the effect of the atmospheric boundary layer has not been included. Future studies should investigate how the differences and similarities in these comparisons would be affected by the shear, the potential stratification, and the wide range of TI found in real-world flows. In addition, the implementation of active grids facilitates replication of dynamic flow events, such as gusts. Several such facilities already exist, for example at the University of Oldenburg (e.g., Berger et al. (2022)) and in the newly upgraded wind tunnel at NTNU (Jooss 2022).

Furthermore, many different AD designs can be investigated. Examples of designs that are not included in this work are the non-uniform disk used by Neunaber et al. (2021), which does not have a solid circumference and has non-constant spacing between the radial ribs, and the semi-uniform disk used by Aubrun et al. (2013), which consists of meshes with different blockages in the center and the surrounding part. Many other designs could also be imagined. Thus, there is ample parameter space to investigate for arriving at a suitable AD design. One idea is to make a thicker object with angled ribs to impose rotation on the wake.

The experiments conducted in this thesis are only done in single planes. However, the wind turbine wake is known to be highly three-dimensional, in particular in the near-wake. The three-dimensional features of the flow fields in the current thesis should be investigated in future studies. This could be done using X-wires in full wake scans (not only single-height scans) or by techniques such as stereo- or volumetric PIV. Of these, only volumetric PIV captures the flow field in a volume, but the other methods can also be used on multiple planes to evaluate three-dimensional phenomena.

For the wind farm measurements reported in Article IV, only the induction region and the first few rows of the wind farm are measured. This gives limited information about the flow farther downstream in a wind farm; thus, similar experiments performed deeper in the farm would be interesting. Only then can the transport of mean kinetic energy into a large wind farm of turbines or ADs be evaluated. The effect of the size of the wind farm and the turbine spacing in streamwise and lateral directions are interesting parameters that have not been addressed in this thesis.

Another interesting aspect for further investigation is the effect of the WGO on a

downstream wind turbine. The different turbulent structures in an AD wake and a wind turbine wake may have a different impact on the flow developing downstream of a second wind turbine. A future study could investigate this by having a second WGO downstream of both an AD and a wind turbine and investigate the wake of the second object.

Bibliography

Abdulrahim, A., Akpolat, M. T., Hassanein, A., Perçin, M. and Uzol, O. (2021), 'Effects of inflow boundary layer on the wake of a radially non-uniform porous disk', *Journal of Renewable and Sustainable Energy* **13**(3), 033302.

Adaramola, M. S. and Krogstad, P. Å. (2011), 'Experimental investigation of wake effects on wind turbine performance', *Renewable Energy* **36**(8), 2078–2086.

Aitken, M. L., Banta, R. M., Pichugina, Y. L. and Lundquist, J. K. (2014), 'Quantifying Wind Turbine Wake Characteristics from Scanning Remote Sensor Data', *Journal of Atmospheric and Oceanic Technology* **31**(4), 765–787.

Allaerts, D. and Meyers, J. (2018), 'Gravity Waves and Wind-Farm Efficiency in Neutral and Stable Conditions', *Boundary-Layer Meteorology* **166**(2), 269–299.

Archer, C. L., Mirzaeisefat, S. and Lee, S. (2013), 'Quantifying the sensitivity of wind farm performance to array layout options using large-eddy simulation', *Geophysical Research Letters* **40**(18), 4963–4970.

Argyle, P., Watson, S., Montavon, C., Jones, I. and Smith, M. (2018), 'Modelling turbulence intensity within a large offshore wind farm', *Wind Energy* **21**(12), 1329–1343.

Aubrun, S., Bastankhah, M., Cal, R. B., Conan, B., Hearst, R. J., Hoek, D., Hölling, M., Huang, M., Hur, C., Karlsen, B., Neunaber, I., Obligado, M., Peinke, J., Percin, M., Saetran, L., Schito, P., Schliffke, B., Sims-Williams, D., Uzol, O., Vinnes, M. K. and Zasso, A. (2019), 'Round-robin tests of porous disc models', *Journal of Physics: Conference Series* **1256**(1), 012004.

Aubrun, S., Loyer, S., Hancock, P. and Hayden, P. (2013), 'Wind turbine wake properties: Comparison between a non-rotating simplified wind turbine model

and a rotating model', *Journal of Wind Engineering and Industrial Aerodynamics* **120**, 1–8.

Barlas, E., Buckingham, S. and van Beeck, J. (2016), 'Roughness Effects on Wind-Turbine Wake Dynamics in a Boundary-Layer Wind Tunnel', *Boundary-Layer Meteorology* **158**, 27–42.

Barthelmie, R. J., Folkerts, L., Ormel, F. T., Sanderhoff, P., Eecen, P. J., Stobbe, O. and Nielsen, N. M. (2003), 'Offshore Wind Turbine Wakes Measured by Sodar', *Journal of Atmospheric and Oceanic Technology* **20**(4), 466–477.

Barthelmie, R. J., Hansen, K., Frandsen, S. T., Rathmann, O., Schepers, J. G., Schlez, W., Phillips, J., Rados, K., Zervos, A., Politis, E. S. and Chaviaropoulos, P. K. (2009), 'Modelling and measuring flow and wind turbine wakes in large wind farms offshore', *Wind Energy* **12**(5), 431–444.

Barthelmie, R. J. and Jensen, L. E. (2010), 'Evaluation of wind farm efficiency and wind turbine wakes at the Nysted offshore wind farm', *Wind Energy* **13**(6), 537–586.

Barthelmie, R. J., Pryor, S. C., Frandsen, S. T., Hansen, K. S., Schepers, J. G., Rados, K., Schlez, W., Neubert, A., Jensen, L. E. and Neckelmann, S. (2010), 'Quantifying the impact of wind turbine wakes on power output at offshore wind farms', *Journal of Atmospheric and Oceanic Technology* **27**(8), 1302–1317.

Bartl, J. and Sætran, L. (2017), 'Blind test comparison of the performance and wake flow between two in-line wind turbines exposed to different turbulent inflow conditions', *Wind Energy Science* **2**(1), 55–76.

Bastankhah, M. and Porté-Agel, F. (2014), 'A new analytical model for wind-turbine wakes', *Renewable Energy* **70**, 116–123.

Bastankhah, M. and Porté-Agel, F. (2017), 'Wind tunnel study of the wind turbine interaction with a boundary-layer flow: Upwind region, turbine performance, and wake region', *Physics of Fluids* **26**(6), 065105.

Bastankhah, M., Welch, B. L., Martínez-Tossas, L. A., King, J. and Fleming, P. (2021), 'Analytical solution for the cumulative wake of wind turbines in wind farms', *Journal of Fluid Mechanics* **911**, A53.

Bastine, D., Wächter, M., Peinke, J., Trabucchi, D. and Kühn, M. (2015), 'Characterizing Wake Turbulence with Staring Lidar Measurements', *Journal of Physics: Conference Series* **625**, 012006.

Beck, C. (2004), 'Superstatistics in hydrodynamic turbulence', *Physica D: Nonlinear Phenomena* **193**(1), 195–207.

Benedict, L. H. and Gould, R. D. (1996), 'Towards better uncertainty estimates for turbulence statistics', *Experiments in Fluids* **22**, 129–136.

Berger, F., Neuhaus, L., Onnen, D., Hölling, M., Schepers, G. and Kühn, M. (2022), 'Experimental analysis of the dynamic inflow effect due to coherent gusts', *Wind Energy Science* **7**, 1827–1846.

Betz, A. (1926), *Wind-Energie und ihre Ausnutzung durch Windmühlen*, Vandenhoeck and Ruprecht, Göttingen.

Bleeg, J., Purcell, M., Ruisi, R. and Traiger, E. (2018), 'Wind farm blockage and the consequences of neglecting its impact on energy production', *Energies* **11**(6), 1609.

Blondel, F. and Cathelain, M. (2020), 'An alternative form of the super-Gaussian wind turbine wake model', *Wind Energy Science* **5**(3), 1225–1236.

Bodini, N., Zardi, D. and Lundquist, J. K. (2017), 'Three-dimensional structure of wind turbine wakes as measured by scanning lidar', *Atmospheric Measurement Techniques* **10**(8), 2881–2896.

Bossuyt, J., Howland, M. F., Meneveau, C. and Meyers, J. (2017), 'Measurement of unsteady loading and power output variability in a micro wind farm model in a wind tunnel', *Experiments in Fluids* **58**, 1.

Branlard, E. and Meyer Forsting, A. R. (2020), 'Assessing the blockage effect of wind turbines and wind farms using an analytical vortex model', *Wind Energy* **23**(11), 2068–2086.

Cal, R. B., Lebrón, J., Castillo, L., Kang, H. S. and Meneveau, C. (2010), 'Experimental study of the horizontally averaged flow structure in a model wind-turbine array boundary layer', *Journal of Renewable and Sustainable Energy* **2**(1), 013106.

Calaf, M., Meneveau, C. and Meyers, J. (2010), 'Large eddy simulation study of fully developed wind-turbine array boundary layers', *Physics of Fluids* **22**(1), 015110.

Camp, E. H. and Cal, R. B. (2016), 'Mean kinetic energy transport and event classification in a model wind turbine array versus an array of porous disks: Energy budget and octant analysis', *Physical Review Fluids* **1**(4), 044404.

Camp, E. H. and Cal, R. B. (2019), 'Low-dimensional representations and anisotropy of model rotor versus porous disk wind turbine arrays', *Physical Review Fluids* **4**(2), 024610.

Cannon, S., Champagne, F. and Glezer, A. (1993), 'Observations of large-scale structures in wakes behind axisymmetric bodies', *Experiments in Fluids* **14**, 450.

Castaing, B., Gagne, Y. and Hopfinger, E. J. (1990), 'Velocity probability density functions of high Reynolds number turbulence', *Physica D: Nonlinear Phenomena* **46**(2), 177–200.

Çengel, Y. A. and Cimbala, J. M. (2014), *Fluid Mechanics: Fundamentals and Applications*, 3rd edn, McGraw-Hill Higher Education, New York.

Chamorro, L. P. and Porté-Agel, F. (2009), 'A wind-tunnel investigation of wind-turbine wakes: Boundary-Layer turbulence effects', *Boundary-Layer Meteorology* **132**(1), 129–149.

Chamorro, L. P. and Porté-Agel, F. (2010), 'Effects of Thermal Stability and Incoming Boundary-Layer Flow Characteristics on Wind-Turbine Wakes: A Wind-Tunnel Study', *Boundary-Layer Meteorology* **136**(3), 515–533.

Chamorro, L. P. and Porté-Agel, F. (2011), 'Turbulent Flow Inside and Above a Wind Farm: A Wind-Tunnel Study', *Energies* **4**(11), 1916–1936.

Cheng, W. C. and Porté-Agel, F. (2018), 'A simple physically-based model for wind-turbine wake growth in a turbulent boundary layer', *Boundary-Layer Meteorology* **169**(1), 1–10.

Chillà, F., Peinke, J. and Castaing, B. (1996), 'Multiplicative Process in Turbulent Velocity Statistics: A Simplified Analysis', *Journal de Physique II* **6**(4), 455–460.

Cortina, G., Sharma, V., Torres, R. and Calaf, M. (2020), 'Mean kinetic energy distribution in finite-size wind farms: A function of turbines' arrangement', *Renewable Energy* **148**, 585–599.

Dong, G., Li, Z., Qin, J. and Yang, X. (2022), 'Predictive capability of actuator disk models for wakes of different wind turbine designs', *Renewable Energy* **188**, 269–281.

Doubrawa, P., Barthelmie, R. J., Wang, H. and Churchfield, M. J. (2017), 'A stochastic wind turbine wake model based on new metrics for wake characterization', *Wind Energy* **20**(3), 449–463.

Duckworth, A. and Barthelmie, R. J. (2008), 'Investigation and validation of wind turbine wake models', *Wind Engineering* **32**(5), 459–475.

Ebenhoch, R., Muro, B., Dahlberg, J. Å., Berkesten Hägglund, P. and Segalini, A. (2017), 'A linearized numerical model of wind-farm flows', *Wind Energy* **20**(5), 859–875.

España, G., Aubrun, S., Loyer, S. and Devinant, P. (2011), 'Spatial study of the wake meandering using modelled wind turbines in a wind tunnel', *Wind Energy* **14**(7), 923–937.

España, G., Aubrun, S., Loyer, S. and Devinant, P. (2012), 'Wind tunnel study of the wake meandering downstream of a modelled wind turbine as an effect of large scale turbulent eddies', *Journal of Wind Engineering and Industrial Aerodynamics* **101**, 24–33.

Fleming, P. A., Ning, A., Gebraad, P. M. O. and Dykes, K. (2016), 'Wind plant system engineering through optimization of layout and yaw control', *Wind Energy* **19**(2), 329–344.

Fox, R. W., McDonald, A. T., Pritchard, P. J. and Mitchell, J. W. (2016), *Fluid Mechanics*, 9th edn, John Wiley & Sons Ltd., Chichester, UK.

Frandsen, S., Barthelmie, R., Pryor, S., Rathmann, O., Larsen, S., Højstrup, J. and Thøgersen, M. (2006), 'Analytical modelling of wind speed deficit in large offshore wind farms', *Wind Energy* **9**(1-2), 39–53.

Fuertes, F. C., Markfort, C. D. and Porté-Agel, F. (2018), 'Wind Turbine Wake Characterization with Nacelle-Mounted Wind Lidars for Analytical Wake Model Validation', *Remote Sensing* **10**(5), 668.

Gadde, S. N. and Stevens, R. J. A. M. (2021), 'Interaction between low-level jets and wind farms in a stable atmospheric boundary layer', *Physical Review Fluids* **6**(1), 014603.

Gambuzza, S. and Ganapathisubramani, B. (2021), 'The effects of free-stream turbulence on the performance of a model wind turbine', *Journal of Renewable and Sustainable Energy* **13**(2), 023304.

Gaumond, M., Réthoré, P.-E., Ott, S., Peña, A., Bechmann, A. and Hansen, K. S. (2014), 'Evaluation of the wind direction uncertainty and its impact on wake modeling at the Horns Rev offshore wind farm', *Wind Energy* **17**(8), 1169–1178.

GWEC (2022), *Global wind report 2022*, Global Wind Energy Council, Brussels.

Hamilton, N., Melius, M. and Cal, R. B. (2015), 'Wind turbine boundary layer arrays for Cartesian and staggered configurations-Part I, flow field and power measurements', *Wind Energy* **18**(2), 277–295.

Hansen, K. S., Réthoré, P.-E., Palma, J., Hevia, B. G., Prospathopoulos, J., Peña, A., Ott, S., Schepers, G., Palomares, A., van der Laan, M. P. and Volker, P. (2015), 'Simulation of wake effects between two wind farms', *Journal of Physics: Conference Series* **625**, 012008.

Hearst, R. J. and Ganapathisubramani, B. (2017), 'Tailoring incoming shear and turbulence profiles for lab-scale wind turbines', *Wind Energy* **20**(12), 2021–2035.

Higuchi, H., Zhang, J., Furuya, S. and Muzas, B. K. (1998), 'Immediate and Near Wake Flow Patterns Behind Slotted Disks', *AIAA Journal* **36**(9), 1626–1634.

Howard, K. B. and Guala, M. (2016), 'Upwind preview to a horizontal axis wind turbine: a wind tunnel and field-scale study', *Wind Energy* **19**(8), 1371–1389.

Howland, M. F., Bossuyt, J., Martínez-Tossas, L. A., Meyers, J. and Meneveau, C. (2016), 'Wake structure in actuator disk models of wind turbines in yaw under uniform inflow conditions', *Journal of Renewable and Sustainable Energy* **8**(4), 043301.

Hultmark, M. and Smits, A. J. (2010), 'Temperature corrections for constant temperature and constant current hot-wire anemometers', *Measurement Science and Technology* **21**(10), 105404.

IEA (2020), *World Energy Outlook 2020*, International Energy Agency, Paris.

IEA (2021), *World Energy Outlook 2021*, International Energy Agency, Paris.

Iungo, G. V., Wu, Y.-T. and Porté-Agel, F. (2013), 'Field Measurements of Wind Turbine Wakes with Lidars', *Journal of Atmospheric and Oceanic Technology* **30**(2), 274–287.

Ivanell, S., Mikkelsen, R., Sørensen, J. N. and Henningson, D. (2010), 'Stability analysis of the tip vortices of a wind turbine', *Wind Energy* **13**(8), 705–715.

Jensen, N. O. (1983), A note on wind generator interaction, Technical Report Risø-M No. 2411, Risø National Laboratory.

Jeong, J. and Hussain, F. (1995), 'On the identification of a vortex', *Journal of Fluid Mechanics* **285**, 69–94.

Jooss, Y. (2022), A fluid mechanic view on urban wind energy, PhD thesis, Norwegian University of Science and Technology, Trondheim.

Kannuluik, W. G. and Carman, E. H. (1951), 'The temperature dependence of the thermal conductivity of air', *Australian Journal of Scientific Research, Series A: Physical Sciences* **4**(3), 305–314.

Käsler, Y., Rahm, S., Simmet, R. and Kühn, M. (2010), 'Wake Measurements of a Multi-MW Wind Turbine with Coherent Long-Range Pulsed Doppler Wind Lidar', *Journal of Atmospheric and Oceanic Technology* **27**(9), 1529–1532.

Kolmogorov, A. N. (1941), 'The local structure of turbulence in incompressible viscous fluids for very large Reynolds numbers', *Doklady Akademii Nauk SSSR* **30**(4), 301–305. (Translated version: (1991) *Proceedings of the Royal Society of London. Series A: Mathematical and Physical Sciences*, **434**(1890), 9–13.).

Krogstad, P.-Å. and Adaramola, M. S. (2012), 'Performance and near wake measurements of a model horizontal axis wind turbine', *Wind Energy* **15**(5), 743–756.

Li, C., Abraham, A., Li, B. and Hong, J. (2020), 'Incoming flow measurements of a utility-scale wind turbine using super-large-scale particle image velocimetry', *Journal of Wind Engineering and Industrial Aerodynamics* **197**, 104074.

Li, L., Hearst, R. J., Ferreira, M. A. and Ganapathisubramani, B. (2020), 'The near-field of a lab-scale wind turbine in tailored turbulent shear flows', *Renewable Energy* **149**, 735–748.

Lignarolo, L. E. M., Ragni, D., Ferreira, C. J. and van Bussel, G. J. W. (2016), 'Experimental comparison of a wind-turbine and of an actuator-disc near wake', *Journal of Renewable and Sustainable Energy* **8**(2), 023301.

Lignarolo, L. E. M., Ragni, D., Krishnaswami, C., Chen, Q., Simão Ferreira, C. J. and van Bussel, G. J. W. (2014), 'Experimental analysis of the wake of a horizontal-axis wind-turbine model', *Renewable Energy* **70**, 31–46.

Lin, M., Xie, C., Yao, M. and Yang, J. (2017), 'Study on the near wake of a honeycomb disk', *Experimental Thermal and Fluid Science* **81**, 33–42.

Maeda, T., Kamada, Y., Murata, J., Yonekura, S., Ito, T., Okawa, A. and Kogaki, T. (2011), 'Wind Tunnel Study on Wind and Turbulence Intensity Profiles in Wind Turbine Wake', *Journal of Thermal Science* **20**(2), 127–132.

Manwell, J. F., McGowan, J. G. and Rogers, A. L. (2009), *Wind Energy Explained: Theory, Design and Application*, John Wiley & Sons, Ltd., Chichester, UK.

Markfort, C. D., Zhang, W. and Porté-Agel, F. (2012), 'Turbulent flow and scalar transport through and over aligned and staggered wind farms', *Journal of Turbulence* **13**, N33.

Martínez-Tossas, L. A., Churchfield, M. J. and Leonardi, S. (2015), 'Large eddy simulations of the flow past wind turbines: Actuator line and disk modeling', *Wind Energy* **18**(6), 1047–1060.

McTavish, S., Rodrigue, S., Feszty, D. and Nitzsche, F. (2015), 'An investigation of in-field blockage effects in closely spaced lateral wind farm configurations', *Wind Energy* **18**(11), 1989–2011.

Medici, D. and Alfredsson, P. H. (2006), 'Measurements on a wind turbine wake: 3D effects and bluff body vortex shedding', *Wind Energy* **9**(3), 219–236.

Medici, D., Ivanell, S., Dahlberg, J. Å. and Alfredsson, P. H. (2011), 'The upstream flow of a wind turbine: blockage effect', *Wind Energy* **14**(5), 691–697.

Meyer Forsting, A. R., Troldborg, N. and Gaunaa, M. (2017), 'The flow upstream of a row of aligned wind turbine rotors and its effect on power production', *Wind Energy* **20**(1), 63–77.

Miller, M. A., Kiefer, J., Westergaard, C., Hansen, M. O. L. and Hultmark, M. (2019), 'Horizontal axis wind turbine testing at high Reynolds numbers', *Physical Review Fluids* **4**(11), 110504.

Morales, A., Wächter, M. and Peinke, J. (2011), 'Characterization of wind turbulence by higher-order statistics', *Wind Energy* **15**(3), 391–406.

Muller, Y.-A., Aubrun, S. and Masson, C. (2015), 'Determination of real-time predictors of the wind turbine wake meandering', *Experiments in Fluids* **56**(3), 53.

Myers, L. E. and Bahaj, A. S. (2010), 'Experimental analysis of the flow field around horizontal axis tidal turbines by use of scale mesh disk rotor simulators', *Ocean Engineering* **37**(2-3), 218–227.

Neal, D. R., Sciacchitano, A., Smith, B. L. and Scarano, F. (2015), 'Collaborative framework for PIV uncertainty quantification: the experimental database', *Measurement Science and Technology* **26**(7), 074003.

Neuhaus, L., Berger, F., Peinke, J. and Hölling, M. (2021), 'Exploring the capabilities of active grids', *Experiments in Fluids* **62**(6), 130.

Neunaber, I., Hölling, M., Stevens, R. J. A. M., Schepers, G. and Peinke, J. (2020), 'Distinct Turbulent Regions in the Wake of a Wind Turbine and Their Inflow-Dependent Locations: The Creation of a Wake Map', *Energies* **13**(20), 5392.

Neunaber, I., Hölling, M., Whale, J. and Peinke, J. (2021), 'Comparison of the turbulence in the wakes of an actuator disc and a model wind turbine by higher order statistics: A wind tunnel study', *Renewable Energy* **179**, 1650–1662.

Newman, A. J., Drew, D. A. and Castillo, L. (2014), 'Pseudo spectral analysis of the energy entrainment in a scaled down wind farm', *Renewable Energy* **70**, 129–141.

Newman, J., Lebron, J., Meneveau, C. and Castillo, L. (2013), 'Streamwise development of the wind turbine boundary layer over a model wind turbine array', *Physics of Fluids* **25**(8), 085108.

Pierella, F. and Sætran, L. (2017), 'Wind tunnel investigation on the effect of the turbine tower on wind turbines wake symmetry', *Wind Energy* **20**(10), 1753–1769.

Piqué, A., Miller, M. A. and Hultmark, M. (2022), 'Laboratory investigation of the near and intermediate wake of a wind turbine at very high Reynolds numbers', *Experiments in Fluids* **63**, 106.

Pope, S. B. (2000), *Turbulent Flows*, Cambridge University Press, Cambridge.

Porté-Agel, F., Bastankhah, M. and Shamsoddin, S. (2020), 'Wind-Turbine and Wind-Farm Flows: A Review', *Boundary-Layer Meteorology* **174**(1), 1–59.

Porté-Agel, F., Wu, Y.-T. and Chen, C. H. (2013), 'A numerical study of the effects of wind direction on turbine wakes and power losses in a large wind farm', *Energies* **6**(10), 5297–5313.

Raffel, M., Willert, C. E., Scarano, F., Kähler, C. J., Wereley, S. T. and Kompenhans, J. (2018), *Particle image velocimetry: A practical guide*, 3rd edn, Springer Cham.

REN21 (2021), *Renewables 2021 Global Status Report*, REN21 Secreteriat, Paris.

Richardson, L. F. (1922), 'Weather prediction by numerical process', *Quarterly Journal of the Royal Meteorological Society* **48**(203), 282–284.

Schepers, J., Lutz, T., Boorsma, K., Gomez-Iradi, S., Herraez, I., Oggiano, L., Rahimi, H., Schaffarczyk, P., Pirrung, G., Madsen, H., Shen, W. and Weihing, P. (2018), *Final Report of IEA Wind Task 29 Mexnext (Phase 3)*, ECN.

Schneemann, J., Theuer, F., Rott, A., Dörenkämper, M. and Kühn, M. (2021), 'Offshore wind farm global blockage measured with scanning lidar', *Wind Energy Science* **6**(2), 521–538.

Schottler, J., Bartl, J., Mühle, F., Sætran, L., Peinke, J. and Hölling, M. (2018), 'Wind tunnel experiments on wind turbine wakes in yaw: Redefining the wake width', *Wind Energy Science* **3**(1), 257–273.

Schwarz, C. M., Ehrich, S., Martín, R. and Peinke, J. (2018), 'Fatigue load estimations of intermittent wind dynamics based on a Blade Element Momentum method', *Journal of Physics: Conference Series* **1037**, 072040.

Sciacchitano, A., Neal, D. R., Smith, B. L., Warner, S. O., Vlachos, P. P., Wieneke, B. and Scarano, F. (2015), 'Collaborative framework for PIV uncertainty quantification: comparative assessment of methods', *Measurement Science and Technology* **26**(7), 074004.

Segalini, A. (2021), 'An analytical model of wind-farm blockage', *Journal of Renewable and Sustainable Energy* **13**(3), 033307.

Segalini, A. and Chericoni, M. (2021), 'Boundary-layer evolution over long wind farms', *Journal of Fluid Mechanics* **925**, A2.

Segalini, A. and Dahlberg, J. Å. (2020), 'Blockage effects in wind farms', *Wind Energy* **23**(2), 120–128.

Sforza, P. M., Sheerin, P. and Smorto, M. (1981), 'Three-dimensional wakes of simulated wind turbines', *AIAA Journal* **19**(9), 1101–1107.

Sherry, M., Sheridan, J. and Lo Jacono, D. (2013), 'Characterisation of a horizontal axis wind turbine's tip and root vortices', *Experiments in Fluids* **54**, 1417.

Simisiroglou, N., Breton, S.-P. and Ivanell, S. (2017), 'Validation of the actuator disc approach using small-scale model wind turbines', *Wind Energy Science* **2**(2), 587–601.

Simley, E., Angelou, N., Mikkelsen, T., Sjöholm, M., Mann, J. and Pao, L. Y. (2016), 'Characterization of wind velocities in the upstream induction zone of a wind turbine using scanning continuous-wave lidars', *Journal of Renewable and Sustainable Energy* **8**(1), 013301.

Singh, A., Howard, K. B. and Guala, M. (2014), 'On the homogenization of turbulent flow structures in the wake of a model wind turbine', *Physics of Fluids* **26**(2), 25103.

Sirovich, L. (1987), 'Turbulence and the dynamics of coherent structures Part I: Coherent structures', *Quarterly of Applied Mathematics* **45**(3), 561–571.

Stevens, R. J. A. M., Gayme, D. F. and Meneveau, C. (2014), 'Large eddy simulation studies of the effects of alignment and wind farm length', *Journal of Renewable and Sustainable Energy* **6**(2), 023105.

Stevens, R. J. A. M., Gayme, D. F. and Meneveau, C. (2016), 'Effects of turbine spacing on the power output of extended wind-farms', *Wind Energy* **19**(2), 359–370.

Stevens, R. J. A. M., Martínez-Tossas, L. A. and Meneveau, C. (2018), 'Comparison of wind farm large eddy simulations using actuator disk and actuator line models with wind tunnel experiments', *Renewable Energy* **116**, 470–478.

Stevens, R. J. A. M. and Meneveau, C. (2017), 'Flow Structure and Turbulence in Wind Farms', *Annual Review of Fluid Mechanics* **49**(1), 311–339.

Strickland, J. M. I. and Stevens, R. J. A. M. (2022), 'Investigating wind farm blockage in a neutral boundary layer using large-eddy simulations', *European Journal of Mechanics - B/Fluids* **95**, 303–314.

Theunissen, R., Housley, P., Allen, C. B. and Carey, C. (2015), 'Experimental verification of computational predictions in power generation variation with layout of offshore wind farms', *Wind Energy* **18**(10), 1739–1757.

Theunissen, R. and Worboys, R. (2019), 'Near-wake observations behind azimuthally perforated disks with varying hole layout and porosity in smooth airstreams at high Reynolds numbers', *Journal of Fluids Engineering, Transactions of the ASME* **141**(5), 051108.

Thomsen, K. and Sørensen, P. (1999), 'Fatigue loads for wind turbines operating in wakes', *Journal of Wind Engineering and Industrial Aerodynamics* **80**(1), 121–136.

Travis, K. N., Smith, S. E., Vignal, L., Djeridi, H., Bourgoin, M., Cal, R. B. and Obligado, M. (2022), 'Characterization of coupling between inertial particles and turbulent wakes from porous disk generators', *Journal of Fluid Mechanics* **933**, A42.

Troldborg, N. and Meyer Forsting, A. R. (2017), 'A simple model of the wind turbine induction zone derived from numerical simulations', *Wind Energy* **20**(12), 2011–2020.

UNFCCC (2015), *The Paris Agreement*, United Nations Framework Convention on Climate Change.

Veers, P., Dykes, K., Lantz, E., Barth, S., Bottasso, C. L., Carlson, O., Clifton, A., Green, J., Green, P., Holttinen, H., Laird, D., Lehtomäki, V., Lundquist, J. K., Manwell, J., Marquis, M., Meneveau, C., Moriarty, P., Munduate, X., Muskulus, M., Naughton, J., Pao, L., Paquette, J., Peinke, J., Robertson, A., Rodrigo, J. S., Sempreviva, A. M., Smith, J. C., Tuohy, A. and Wiser, R. (2019), 'Grand challenges in the science of wind energy', *Science* **366**(6464), eaau2027.

VerHulst, C. and Meneveau, C. (2015), 'Altering Kinetic Energy Entrainment in Large Eddy Simulations of Large Wind Farms Using Unconventional Wind Turbine Actuator Forcing', *Energies* **8**(1), 370–386.

Vermeer, L. J., Sørensen, J. N. and Crespo, A. (2003), 'Wind turbine wake aerodynamics', *Progress in Aerospace Sciences* **39**(6-7), 467–510.

Wächter, M., Heißelmann, H., Hölling, M., Morales, A., Milan, P., Mücke, T., Peinke, J., Reinke, N. and Rinn, P. (2012), 'The turbulent nature of the atmospheric boundary layer and its impact on the wind energy conversion process', *Journal of Turbulence* **13**(26), 1–21.

Wieneke, B. (2015), 'PIV uncertainty quantification from correlation statistics', *Measurement Science and Technology* **26**(7), 074002.

Wu, K. L. and Porté-Agel, F. (2017), 'Flow Adjustment Inside and Around Large Finite-Size Wind Farms', *Energies* **10**(12), 2164.

Wu, Y.-T., Liao, T. L., Chen, C. K., Lin, C. Y. and Chen, P. W. (2019), 'Power output efficiency in large wind farms with different hub heights and configurations', *Renewable Energy* **132**, 941–949.

Wu, Y.-T. and Porté-Agel, F. (2012), 'Atmospheric Turbulence Effects on Wind-Turbine Wakes: An LES Study', *Energies* **5**(12), 5340–5362.

Wu, Y.-T. and Porté-Agel, F. (2013), 'Simulation of Turbulent Flow Inside and Above Wind Farms: Model Validation and Layout Effects', *Boundary-Layer Meteorology* **146**, 181–205.

Wu, Y.-T. and Porté-Agel, F. (2015), 'Modeling turbine wakes and power losses within a wind farm using LES: An application to the Horns Rev offshore wind farm', *Renewable Energy* **75**, 945–955.

Xiao, H., Duan, L., Sui, R. and Rösgen, T. (2013), Experimental investigations of turbulent wake behind porous disks, *in* '1st Marine Energy Technology Symposium, Washington DC'.

Yu, W., Hong, V. W., Ferreira, C. and van Kuik, G. M. A. (2017), 'Experimental analysis on the dynamic wake of an actuator disc undergoing transient loads', *Experiments in Fluids* **58**, 149.

Zhan, L., Letizia, S. and Valerio Iungo, G. (2020), 'LiDAR measurements for an onshore wind farm: Wake variability for different incoming wind speeds and atmospheric stability regimes', *Wind Energy* **23**(3), 501–527.

Zhang, W., Markfort, C. D. and Porté-Agel, F. (2012), 'Near-wake flow structure downwind of a wind turbine in a turbulent boundary layer', *Experiments in Fluids* **52**, 1219–1235.

Publications in full text

Article I

The far wake of porous disks and a model wind turbine: Similarities and differences assessed by hot-wire anemometry

Magnus K. Vinnes, Stefano Gambuzza, Bharathram Ganapathisubramani, R. Jason Hearst

Published in:
Journal of Renewable and Sustainable Energy, ***14****, 023304, (2022)*

Journal of Renewable and Sustainable Energy

The far wake of porous disks and a model wind turbine: Similarities and differences assessed by hot-wire anemometry

Cite as: J. Renewable Sustainable Energy **14**, 023304 (2022); https://doi.org/10.1063/5.0074218
Submitted: 07 October 2021 • Accepted: 08 March 2022 • Published Online: 24 March 2022

Magnus K. Vinnes, Stefano Gambuzza, Bharathram Ganapathisubramani, et al.

Journal of Renewable and Sustainable Energy ARTICLE scitation.org/journal/rse

The far wake of porous disks and a model wind turbine: Similarities and differences assessed by hot-wire anemometry

Cite as: J. Renewable Sustainable Energy **14**, 023304 (2022); doi: 10.1063/5.0074218
Submitted: 7 October 2021 · Accepted: 8 March 2022 ·
Published Online: 24 March 2022

Magnus K. Vinnes,[1,a)] Stefano Gambuzza,[2] Bharathram Ganapathisubramani,[2] and R. Jason Hearst[1,a)]

AFFILIATIONS

[1]Department of Energy and Process Engineering, Norwegian University of Science and Technology, Trondheim, Norway
[2]Engineering and Physical Sciences, University of Southampton, Southampton, United Kingdom

[a)]**Authors to whom correspondence should be addressed:** magnus.kyrkjebo@ntnu.no and jason.hearst@ntnu.no

ABSTRACT

The wakes of two different porous disks have been evaluated experimentally. Such disks are commonly used as physical actuator disk analogs for wind turbines. One disk is made of a uniform wire mesh, while the other has a nonuniform design with radial spars connected by rings. The disks have the same solidity and produce approximately the same drag. The wakes have also been compared to the wake of a model wind turbine and a solid disk. In contrast to earlier studies, the far wake, up to 30 diameters downstream, is included in the comparison. In the near wake, the velocity deficit and turbulence intensity profiles of the disk wakes differ significantly. High levels of turbulence intensity in the wake of the nonuniform disk increase the transverse transport in the wake, which leads to faster spreading and lower velocity deficits in the far wake, compared to the uniform disk and the wind turbine. High velocity gradients in the wake of the uniform disk give rise to turbulence production farther downstream, maintaining higher turbulence levels in the far wake. In addition, coherent vortex shedding is only identified in the wake of the nonuniform disk. None of the disks were able to replicate the asymmetric features of the wind turbine wake. Nonetheless, the results highlight important flow physics that should be considered in the design process of a porous disk used as a wind turbine surrogate.

I. INTRODUCTION

Wind turbines (WTs) are typically located in clusters, called wind farms. In such farms, many turbines operate in the wake of upstream turbines, experiencing reduced mean wind velocity and increased turbulence intensity (TI) compared to the undisturbed incoming flow. The decreased velocity reduces the power production potential. Barthelmie and Jensen[1] found a difference in the power production of up to 20% between turbines located in the center of the Nysted offshore wind farm and the turbines located at the edge. Increased TI leads to higher mechanical loads on the structure. Thomsen and Sørensen[2] reported 5%–15% higher loads on a turbine in a farm compared to a single turbine, with the exact value depending on the farm layout.

The near wake is often defined to be the region where rotation and tip and root vortices are seen in the flow, that is, where the signature of the turbine, nacelle, and tower dominate the flow.[3] The near wake of a wind turbine is a highly three-dimensional flow. The turbine rotation adds a counter-rotation to the wake flow.[4] Tip vortices and root vortices further complicate the flow.[3,5] However, both the rotation and the vortices lose strength rapidly. The azimuthal velocity in the wake has been shown to be only a few percent of the freestream velocity at a distance of 1 rotor diameter (D) downstream of the turbine.[4] The size of the near wake depends on the incoming flow. Typically, it ends between $2D$ and $4D$ downstream of the turbine.[6,7]

In wind farms, the spacing between turbines is typically in the range of $5D$ to $10D$, as exemplified by five different full scale farms shown in Table I. Depending on the wind direction compared to the farm alignment, turbines even farther downstream might be located directly in the wakes of upstream turbines, as can be seen in the work by Porté-Agel *et al.*[8] The turbines will thus never be located in the near wake of other turbines, but rather in the far wake. While the flow is highly three dimensional in the near wake, the far wake has more global characteristics of the velocity deficit and TI.[3] When the complicated flow structures in the near wake are less important, it is possible

TABLE I. Turbine spacing in different wind farms.

Wind farm	Spacing (D)
Nysted[1]	5.8–10.5
Horns rev I[13]	7
Rødsand II[14]	5–10
Greater Gabbard[15]	8.3–10
Princess Amalia[16]	6.9–7.1

to simplify both computations and experiments. Therefore, actuator disk (AD) methodology has become a popular tool. In simulations, it consists of implementing a pressure discontinuity at the disk location.[9] In some cases, the rotation of the flow can also be added.[7,10,11] In experiments, the analogy is to use porous disks (PDs) with the same drag coefficient

$$C_D = \frac{F_D}{\frac{1}{2}\rho U_\infty^2 A} \tag{1}$$

as that of a wind turbine.[12] Here, F_D is the drag force acting on the turbine; ρ is the density of the air; U_∞ is the freestream velocity; and A is the swept area of the rotor, corresponding to the frontal area of an AD. Note that in this study, C_D is used rather than the thrust coefficient C_T, as the focus is on disks. They are, however, the same parameter.

Computational research has evolved to utilize the available computational power of supercomputers. Large eddy simulations (LESs), where only the small turbulent scales are modeled and the large scales are directly simulated from the governing equations, have become a popular tool. Many LES studies on wind turbines or wind farms utilize either rotating or non-rotating AD models (e.g., Refs. 8 and 17–20). Reviews on simulations of wind farm flows are found in the recent review papers by Stevens and Meneveau[6] and Porté-Agel *et al.*[7] In industrial applications, where LES is too expensive, wake models are used to plan the layout of a wind farm. Some of the best known models are the Jensen model[21] and the Frandsen model.[22] The development of new wake models as well as the improvement of earlier models are still subjects of academic interest.[23–26] Experimental studies are needed to validate both wake models and simulation results,[6] and are also useful and necessary to obtain further insight into the physical phenomena that govern flow around wind turbines and wind farms.[7]

PDs are popular to use as experimental wind turbine models. Wake meandering in relation to large scale boundary layer structures was investigated by España *et al.*[27,28] and Muller *et al.*,[29] who both used wire mesh disks as a static wind turbine models. Howland *et al.*[30] studied the wake deflection downstream of a yawed PD, stating that the deflection of the wake is largest near the center. They used a disk with ribs protruding from the center, connecting several solid circles at different radial positions. Very recently, Abdulrahim *et al.*[31] investigated which effects an incoming boundary layer has on the wake of a PD of similar design. Unsteady loading on wire mesh disks was studied by Yu *et al.*[32,33] PDs have also been used as wind turbine models in wind farm experiments. For example, Theunissen *et al.*[34] measured the drag of a model wind farm where the turbines were represented by perforated disks, while Bossuyt *et al.*[35] used 100 PDs to measure the spatiotemporal power output from wind farms in different arrangements.

While PDs have already been used as static wind turbine models, several studies also focus directly on the flow field around them. Early PD experiments were performed by Sforza *et al.*[36] They measured the wake expansion and velocity deficit downstream of perforated disks with different solidity. Instead of using perforated disks, Cannon *et al.*[37] used wire mesh disks in their flow visualization of the wake downstream of disks with different solidity. For disks with a solidity lower than 60%, they did not observe vortex shedding in the wake, in contrast to the vortex shedding seen behind solid disks (SDs) and wire mesh disks with higher solidity. The near wake of slotted disks of different solidity was investigated by Higuchi *et al.*[38] They reported that the three-dimensional structures downstream of the perforated disks are more axisymmetric than those behind a solid disk. More recently, Myers and Bahaj[39] showed that beyond 6*D* downstream of wire mesh disks, the wake velocity deficit is nearly independent of the disk solidity when it is varied. Lin *et al.*[40] found that the wake of a perforated disk with a solidity of 88% had a higher maximum velocity deficit than the wake of a solid disk in the range from 3*D* to 5*D* downstream, and that the structure of the recirculation zone was different between the disks. This is in contrast to results reported by Xiao *et al.*,[41] which reported lower velocity deficit in the wake of a perforated disk with 75% blockage compared to the wake of a solid disk. Ranjbar *et al.*[42] investigated the drag, induction factor, and the power coefficient estimated from the induction factor for porous disks of different solidities. Recently, Huang *et al.*[43] introduced a new scaling parameter $D^* = 4A/P$, with A being the disk area and P the perimeter, to match the wake recovery of porous disks of different geometries: circular, square, and rectangular.

Several studies have assessed the feasibility of using ADs as wind turbine models in simulations, both for single turbines (e.g., Ref. 44) and for several interacting turbines (e.g., Ref. 45). To validate the usage of PDs in wind tunnel experiments, Aubrun *et al.*[46] performed hot-wire measurements in the near wake of a rotating turbine and a wire mesh disk. They found reasonable agreement up to the fourth-order turbulence statistics in the wake 3*D* downstream of the wake generating objects (WGOs), both in decaying isotropic turbulence and in an atmospheric boundary layer. Later, Lignarolo *et al.*[47] used stereo particle image velocimetry (SPIV) to capture the near wake of a wire mesh disk and a rotating turbine. They showed that the wakes agree well, but that the TI is higher in the shear layer of the turbine than the disk. It was also shown that the total flux of kinetic energy into the wake is equal for the two cases, although the tip vortices from the turbine contribute both with a positive and a negative flux, meaning that the transport mechanisms are different in the different wakes.[47] The difference in the instantaneous structures of a PD wake and a rotating turbine wake was recently emphasized by Helvig *et al.*[12] They showed that the coherent structures in the near wake differ both in size and location between a rotating model and a porous disk. Neunaber[48] has later confirmed that the PD and wind turbine wakes mix differently in the near wake, but that the centerline evolution in the far wakes is similar.[49] These studies did not use a wire mesh disk, but they have a design with nonuniform blockage and without an outer solid rim. Similar disks, but with a solid circumference, were used by Camp and

Cal.[50,51] They used a 3 × 4 array of turbines and disks, and did particle image velocimetry (PIV) around the center turbine in the last row. In the far wake, the mean kinetic energy transport is captured well by the PD. However, they highlight the importance of properly choosing the design of the PD. The near wake features of PDs were examined by Theunissen and Worboys.[52] They varied the hole topology and positions of high solidity PDs and observed near wake features as for example jet mixing.

The aforementioned comparisons generally target the near wake, with limited information downstream of approximately 5D from the WGO. This is upstream of where subsequent turbines are placed in several real wind farms (Table I). Furthermore, there is no agreement on what is the best design philosophy for such PD models. Aubrun *et al.*[53] began to address this by comparing the wakes of two actuator disks in different facilities at 4D. Later, Helvig *et al.*[12] compared several PDs to a rotating model, detailing how one of the disks generated a wake more similar to the wake of a rotating model. Although the results showed good agreement in the mean features, their analysis showed discrepancies between the wakes with regard to the temporal structures in the flow, and again the results were limited to the near wake, stopping at 3.5D.

This work fills a knowledge gap by performing measurements in the wakes of two different PDs and a power extracting wind turbine model at distances up to 30D downstream. Such measurements are important in that wake modeling essentially assumes an asymptotic self-similar state, which in turbulence is rarely assumed to begin within the first tens of characteristic lengths from a body; but, this is the exact region of interest in wind energy. There is thus a need to investigate if wakes of different PDs with the same drag and at the same characteristic velocity in fact do approach one another before the typical position of the next turbine; and if not, do they ever agree within the measurable range of the experimental facility? The measurements were performed in low-turbulence, uniform conditions, rather than in a turbulent boundary layer, to isolate the effect of changing the geometry of the WGOs. The design of the two PDs is different in their nature: whereas one of them is a wire mesh, the other is a perforated disk with nonhomogeneous blockage. As a reference case, the wake behind a solid disk was also measured. Turbulence statistics from first- to fourth-order velocity moments are presented. This is thus the first study evaluating the ability of PDs to replicate a wind turbine far wake. It also presents a first glance at a detailed comparison of the far wake downstream of different PDs used as wind turbine models.

II. EXPERIMENTAL SETUP

A. Disks and wind turbine

The two ADs used in the present study have a diameter of $D = 200$ mm and a solidity of $\sigma = 57\%$. The solidity is thus lower than the limit of where vortex shedding was observed by Cannon *et al.*[37] The first disk was cut from an industrially manufactured wire mesh with a wire thickness of 0.8 mm, and has a uniform blockage. The disk, here referred to as the uniform disk (UD), is the same as the uniform PD used by Aubrun *et al.*[53] in their blind test comparison. The other disk was designed to have the same solidity as the UD but now with a nonuniform blockage. It is therefore referred to as the non-uniform disk (ND). The ND has ribs expanding from the center to a solid rim. The blockage is highest near the center of the disk, which replicates the relatively large size of the wind turbine blades at the same location and the nacelle. The design is based on the nonuniform disk used by Aubrun *et al.*[53] and Camp and Cal.[50,51] The ND was machined from a 5 mm thick acrylic sheet to match the diameter and solidity of the UD. Schematics of the UD and ND are shown in Fig. 1. The drag of the disks was measured using a force balance, and it was found that $C_D = 0.77$ and $C_D = 0.82$ for the UD and the ND, respectively. As a reference case, the wake of a wooden, 9 mm thick, solid disk (SD) with the same diameter, $D = 200$ mm was also measured. The SD has $C_D = 1.1$, as expected for this geometry. All the disks

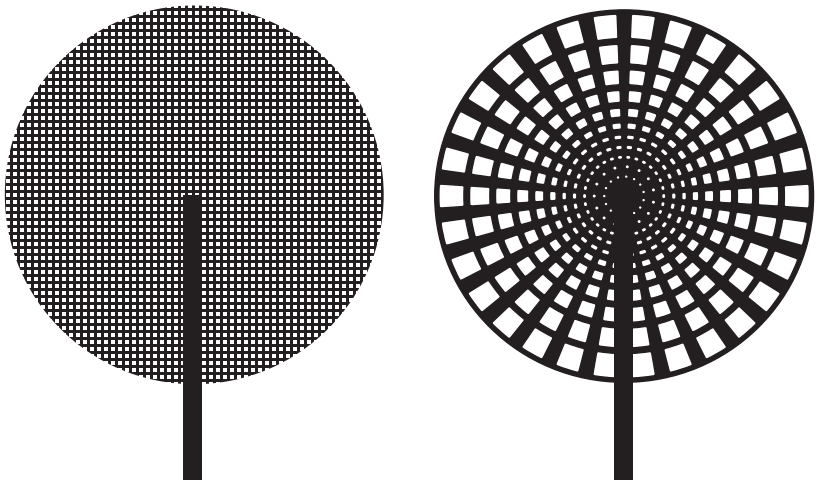

FIG. 1. Schematics of the uniform disk, UD, (left) and the non-uniform disk, ND, (right) mounted to towers.

were attached to a 10 mm diameter steel rod, which in turn was mounted to a thicker steel rod with a diameter of 32 mm. The thicker mast stops 200 mm below the hub height. To reduce the influence of the thicker rod, a cable was wound around it to act as a vortex disruptor.[54] The length of the rods was adjusted in order for the disks to be located in the vertical and horizontal center of the wind tunnel cross section such that the wake is not affected by the boundary layers of the wind tunnel walls.

The wind turbine (WT) is a three-bladed, speed-controlled fixed-pitch turbine. It has the same diameter as the disks, $D = 200$ mm. The blades were 3D-printed with a stereolithography printer, with the NACA 63–418 airfoil profile along the entire blade. The chord of the blade ranges from 25 mm at the hub to 12.5 mm at the tip, and the geometrical pitch angle ranges from $\theta = 39.57°$ to $\theta = 0.73°$. The values were chosen to give a constant angle-of-attack (α) of 12° along the blade at a tip speed ratio $\lambda = 3.5$, which yields good turbine performance according to blade element momentum simulations. The hub of the turbine has a diameter of 22 mm, and the generator, encoder, and wiring were enclosed in the nacelle, which has a diameter of 24 mm and was 3D-printed with a filament-deposit printer using polylactic acid (PLA). Furthermore, the nacelle was mounted to a rod with a diameter of 20 mm. This rod was mounted to the same mast as the actuator disks. Figure 2 shows the WT mounted in the wind tunnel.

The rotational speed of the WT was set to achieve the maximum power coefficient, C_p, at the given incoming velocity. Figure 3 shows the power curve of the WT, with the dotted vertical line illustrating the operating point at $\lambda = 3.65$, which is close to the λ that was used to determine the geometrical pitch of the blade. Details about the control and electronics of the WT can be found in a recent paper by Gambuzza and Ganapathisubramani.[55] They use the same control system on a slightly smaller turbine. Due to constraints in the experimental setup, it was not possible to measure the drag of the rotating turbine. Through wake integration, the drag of the WT was found to be smaller than the drag of the PDs, although this method is not robust enough to yield exact values due to the 3D nature of the flow. Nevertheless, important features, such as tip vortices and rotation of the flow, are present in the model WT wake. The main focus of this work is on the disks, and thus the turbine is only used for qualitative comparison of the flow features given the disparity in drag.

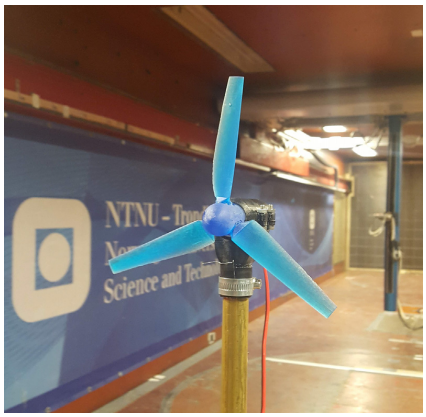

FIG. 2. The wind turbine model, WT, mounted in the wind tunnel. The traversing system with the hot wires can be seen in the background.

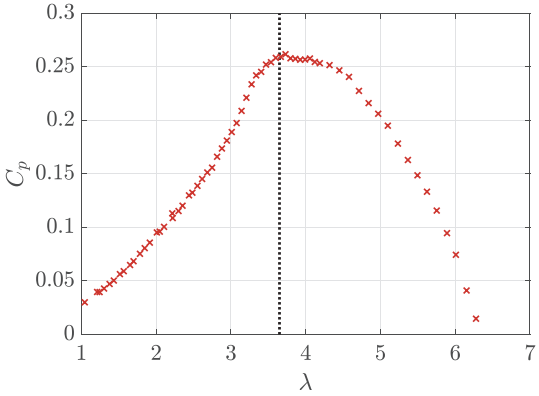

FIG. 3. C_p at different λ. In the experiments, $\lambda = 3.65$ illustrated by the dotted line, was used.

B. Facility

The experiments were performed in the $11.15 \times 2.71 \times 1.80\ \text{m}^3$ (length × width × height) closed loop wind tunnel at the Norwegian University of Science and Technology. The height of the roof was gradually increased from 1.80 m at the inlet to 1.85 m at the outlet of the test section to compensate for the growing boundary layer thickness. The WGOs cover an area well below 1% of the wind tunnel cross section, and blockage effects are negligible. To ensure low TI and homogeneous flow, a wire mesh screen was installed at the inlet of the test section. The WGOs were mounted 1.6 m downstream of the contraction, corresponding to 640 mesh lengths (M) downstream of the screen. A schematic of the facility is shown in Fig. 4.

Hot-wire anemometry (HWA) was used for all velocity measurements. Three Dantec Dynamics 55P11 single-wire probes, operated in constant temperature mode, were used for simultaneous sampling. They were connected to a Dantec Dynamics StreamLine Pro anemometer. The sampling frequency was 30 kHz, with an analog low-pass filter applied at 10 kHz. An automated traversing system was used to make horizontal scans at six different downstream locations, $x/D = 3, 5, 10, 15, 20$, and 30, illustrated by ×-symbols in Fig. 4. All scans were performed at hub height. It should be noted that the hub height does not represent the wake centerline, as the tower shifts the wake downward.[56] However, in many wind farms, the turbine hubs will be at the same height; thus, hub-height measurements are of utmost important for any downstream turbine. At the beginning and end of each day of the campaign, the probes were calibrated against a pitot-tube. The temperature was recorded with a thermocouple, and the calibrations were corrected for temperature variations according to the procedure outlined by Hultmark and Smits.[57] A weighted average,

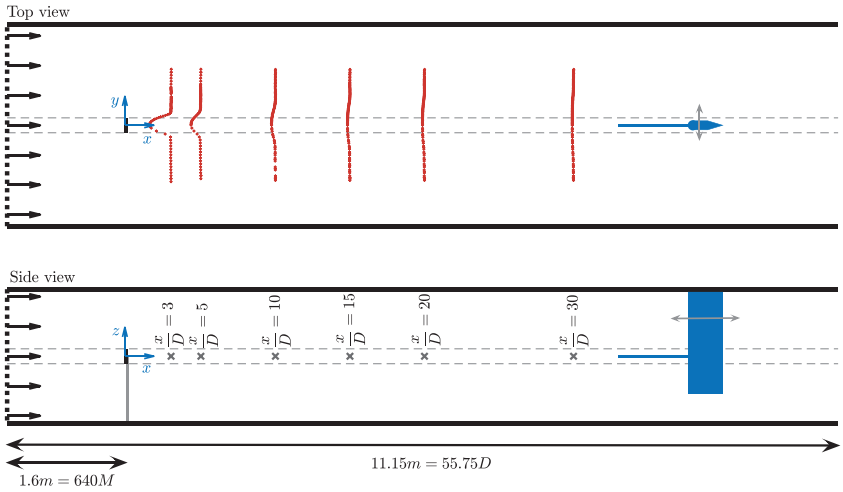

FIG. 4. Schematics of experimental setup in the test section of the wind tunnel. The streamwise locations of the hot-wire scans are marked with × in the side view. The velocity profiles for the non-uniform disk are shown in the top view.

based on the time between acquisition and each of the two calibrations, was used to convert the voltage signal to velocity.

In the wake of the WT, the distance between each measurement point in the scan was 10 mm at all downstream positions. In the wakes of the disks, which are expected to be symmetric, only half the wake was scanned with 10 mm distance between the measurement points. To check for symmetry, the other half of the wake was scanned with a maximum distance between two measurement points of 50 mm. In the freestream, outside of the wake, the larger distance was used. To ensure good convergence of turbulence statistics up to the fourth order, 360 s measurements were taken when the distance between the measurement points was small. For the lower density measurements, 200 s samples were used. The measurements from the three different wires were normalized to each other by the first measurement in each profile scan. To account for hot-wire drift, the last measurement was normalized to the first measurement for the separate wires. All the normalizing measurements were taken well outside the wake region. For the profiles farthest downstream of the SD, the wake outgrew the traverse limits such that normalization was not possible. Instead, correction factors for the start and end of each scan were found by minimizing the least squares error between the separate wire profiles. A weighted average of the correction factors was used across the scans. This procedure was only applied at the two most downstream profiles and only influences the mean velocity profiles, not the higher-order statistics.

The velocity and turbulence profiles of the background flow were measured with hot-wire anemometry at six different streamwise positions. The incoming velocity was $U_\infty \simeq 8.1$ m/s, corresponding to a Reynolds number of $Re = (DU_\infty)/\nu \simeq 10^5$. At each position, a 200 s sample was taken. The profiles are shown in Fig. 5. The velocity is uniform within $\pm 1\%$ for all streamwise positions. Recall, the WGOs are located in the center of the tunnel, far away from the boundary layers of the tunnel walls. A small shear is observed in the center of the tunnel, with the velocity on the positive side ($y > 0$) being slightly higher. This small shear shifts the wakes of the WGOs slightly toward $y > 0$. For all the WGOs, at all downstream positions, this shift is within 2% of the distance from the object. The shift is also approximately the same for the different objects. Based on this, the small velocity gradient was judged to be acceptable. The TI, defined as u'/U, where U is the local mean velocity and u' is the standard deviation of the velocity fluctuations, is also shown. The values are below 6×10^{-3} across the tunnel (0.6% turbulence intensity). The small shear in the tunnel leads to a peak and asymmetry in the TI profiles. The other parts of the

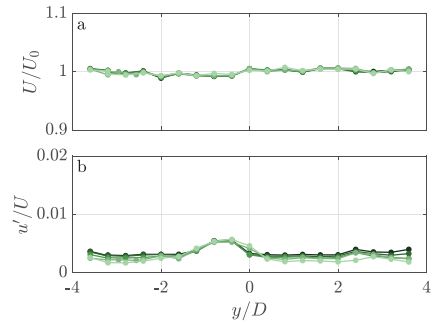

FIG. 5. Mean velocity (a) and turbulence intensity, TI, (b) of the background flow in the wind tunnel. The velocity is normalized by the mean velocity across the tunnel, U_0. Measurements are taken at five streamwise positions – $x = 0D$, $0.5D$, $3D$, $10D$ and, $30D$ – at the height of the center of the wake-generating objects. The colors in the figure range from dark at $0D$ to light at $30D$.

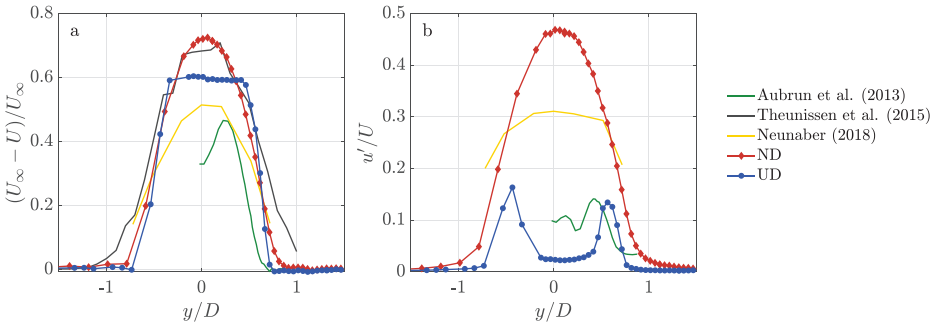

FIG. 6. Velocity deficit (a) and turbulence intensity, TI, (b) of disk wakes from the present study and the literature. The profiles are taken at positions close to $x = 3D$.

profiles have values around 3×10^{-3} (0.3% turbulence intensity), decaying with increasing downstream distance. Overall, these values are quite low for a facility of this size.

III. BASELINE COMPARISON TO OTHER STUDIES

Wind turbine and PD wakes have been reported extensively in the literature (e.g., Refs. 4, 34, 46, 48, 58, and 59). To put the current results into context, the velocity deficit ($(U_\infty - U)/U_\infty$) and TI measured in the present study are compared to a sample of results from existing studies that could be accessed. The comparison is made at $x \approx 3D$, as this is a common measured position for most studies. In Fig. 6, the velocity deficit and the TI in the wake of several PDs are shown. The different studies used in the comparison are briefly summarized in Table II. The velocity and TI profiles differ between the studies. Some of the discrepancies are due to the different C_D of the disks; also, the shape of the profiles is different between the disks. The velocity deficit ranged from rounded, Gaussian-like profiles to top-hat profiles, with the ND and the UD representing the two extremities, respectively. Large discrepancies in the TI profiles can also be observed between the disks. In total, the wake of the ND is somewhat similar to the wake of Neunaber's[48] disk, while the wakes of Aubrun's[46] disk and the UD show some similarities in the TI profiles. To improve wind turbine models, it is important to understand the physics leading to these differences. To that measure, the two different PDs used in this work are reasonable design choices, as the shape of their velocity deficit and TI profiles differ from each other and cover the span of differences seen between earlier disks.

Similarly, the wake of the rotating model has been compared to different earlier wake measurements, ranging from lab-scale to full-scale measurements. The results are shown in Fig. 7. Information about the presented studies can be found in Table III. Most of the turbines, including the WT used in the present study, have an asymmetric wake. However, the wakes reported by Medici and Alfredsson[4] and Neunaber[48] are close to symmetric. Also here, some of the differences arise from different operating conditions. This effect is particularly evident in the full-scale measurements by Zhan *et al.*[59] Two of the cases they report are shown in Fig. 7. While these are wake measurements of the same turbine, the different operating conditions during the measurements change the wake. Clearly, it is difficult to compare PD models to rotating models and full-scale wind turbines when even the benchmark is highly dependent on operating conditions.

Nonetheless, the figure shows that the WT used in the present study has a wake that, with respect to the magnitude of the velocity deficit and TI, and the width of the wake, lies within typical results from other studies. Only the full-scale measurements by Zhan *et al.*[59] show wider wakes, but the results they present are obtained by averaging velocity measurements over a small range of different incoming conditions and wind directions over a fixed time, which could possibly make the wake appear wider. In addition, the shape of the WT wake profile qualitatively agrees well with the full-scale measurements by Zhan *et al.*[59] despite the lower C_D. Thus, the WT is a suitable benchmark for the present investigation where we can rigorously control the experimental conditions.

IV. RESULTS

A. Mean velocity and turbulence intensity

A wind turbine's power production is governed by the incoming velocity. It is therefore important to match the wake velocity profile of

TABLE II. List of actuator disks in Fig. 6.

Reference	Description	Re	x/D	C_D	Solidity	Technique
Aubrun *et al.* (2013)[46]	Wire mesh	7×10^4	3		0.45/0.35	HWA, 1C
Theunissen *et al.* (2015)[34]	Holes	4×10^4	3		0.86	LDV, 2C
Neunaber (2018)[48]	Ribs	3×10^5	2.97	0.96	0.53	HWA, 1C
ND	Ribs	1×10^5	3	0.82	0.57	HWA, 1C
UD	Wire mesh	1×10^5	3	0.77	0.57	HWA, 1C

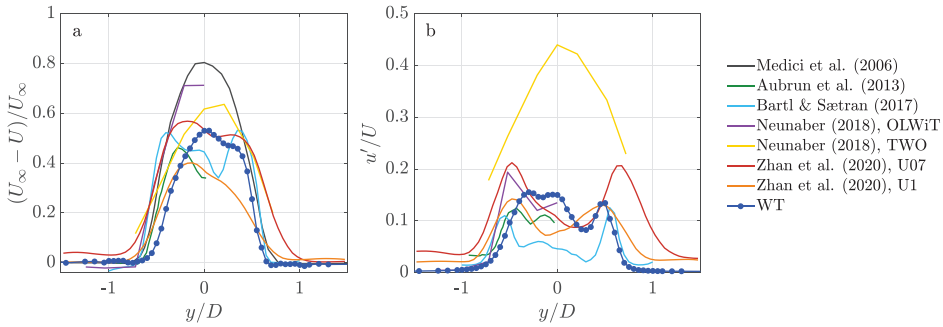

FIG. 7. Velocity deficit (a) and turbulence intensity, TI, (b) of turbine wakes from the present study and the literature. The profiles are taken at positions close to $x = 3D$.

a PD's wake to a wind turbine wake. Figure 8 shows the velocity deficit of all WGOs used in this study. All six downstream positions are presented in the different subfigures.

The SD and the ND both have rounded velocity profiles at $x = 3D$. The maximum velocity deficit is high for the ND this close to the disk. For both the mentioned disks, the velocity deficit diminishes rapidly farther downstream. At the same time, the wake extends horizontally, spanning the entire range of the measurements at $x = 30D$. The SD wake is wider than the ND wake, throughout the measurement region, but it has a lower maximum velocity deficit. This is in agreement with Lin *et al.*[40] but in contrast to Xiao *et al.*[41]

In the near wake, at $x = 3D$, the UD generates a different wake. The velocity deficit has a top hat profile, with strong velocity gradients at the edges of the wake. The UD reduces the velocity evenly across its cross section. From $x = 5D$, the velocity gradients are reduced. However, the maximum velocity deficit increases slightly between $3D$ and $5D$ downstream of the disk. The maximum velocity deficit is reduced farther downstream, but not as much as for the ND. For $x \geq 5D$, the disk has the highest maximum velocity deficit of all the WGOs. The wake is also smaller in width, keeping the high velocity deficit in the center of the wake, in contrast to the velocity deficit in the ND wake, which is spread out over a larger area. Hence, there are large differences between the wakes of the two PDs, even though they are generated by disks with the same diameter, solidity, and approximately the same C_D. Note that here, the normalized velocity deficit is plotted, such that both shape and magnitude could be evaluated. In Appendix A, figures of the self-normalized velocity deficit and TI are provided, to allow for better comparison of the shape of the wake profiles. The self-normalized profiles further indicate that the shape of the mean velocity profile that best matches the WT is the UD, at least for $x/D \geq 10$.

The WT wake has a smaller velocity deficit than the ND and UD at $x = 3D$, which is related to its lower C_D. As such, we offer the comparison to this model in order to identify phenomenological features of the WT wake and its general shape, rather than a direct comparison to the velocity deficit. The WT wake is asymmetric, as was also seen in Fig. 7. The reduction of the maximum velocity deficit is slower compared to the ND, and already at $5D$ downstream, the maximum velocity deficit is higher for the WT despite the lower C_D. The expansion of the wake width is also smaller. Figure 9 shows both the evolution of the wake width and the evolution of the maximum velocity deficit for all WGOs. The wake width, $\Delta\delta_{0.5}$, is defined as the distance between the two points where the velocity deficit is half the maximum velocity deficit, and is displayed in Fig. 9(a). The expansion of the wake of the WT and the UD collapses very well for $x \geq 10D$, while the SD and ND grow much faster. It is interesting to note that the latter two grow at approximately the same rate, even though their width is different. The evolution of the maximum velocity deficit, displayed in Fig. 9(b), does not show the same behavior. Still, the decay of the maximum velocity deficit is more rapid in the ND wake than the WT and UD

TABLE III. List of turbines in Fig. 7.

Reference	*Re*	*x/D*	No. blades	C_D	λ	Technique
Medici and Alfredsson (2006)[4]	1×10^5	3	2	0.794	3.66	HWA, 2C
Aubrun *et al.* (2013)[46]	7×10^4	3	3	0.5	5.8	HWA, 1C
Neunaber, TWO (2018)[48]	3×10^5	2.97	3	1	5.7	HWA, 1C
Neunaber, OLWiT (2018)[48]	3×10^5	2.97	3	1	6.2	HWA, 1C
Bartl and Sætran (2017)[58]	7×10^5	2.77	3	0.811	6.0	HWA, 1C
Zhan *et al.* (2020)[59]	Full-scale	2.75	3			LiDAR
Zhan *et al.* (2020)[59]	Full-scale	2.75	3			LiDAR
WT	1×10^5	3	3		3.65	HWA, 1C

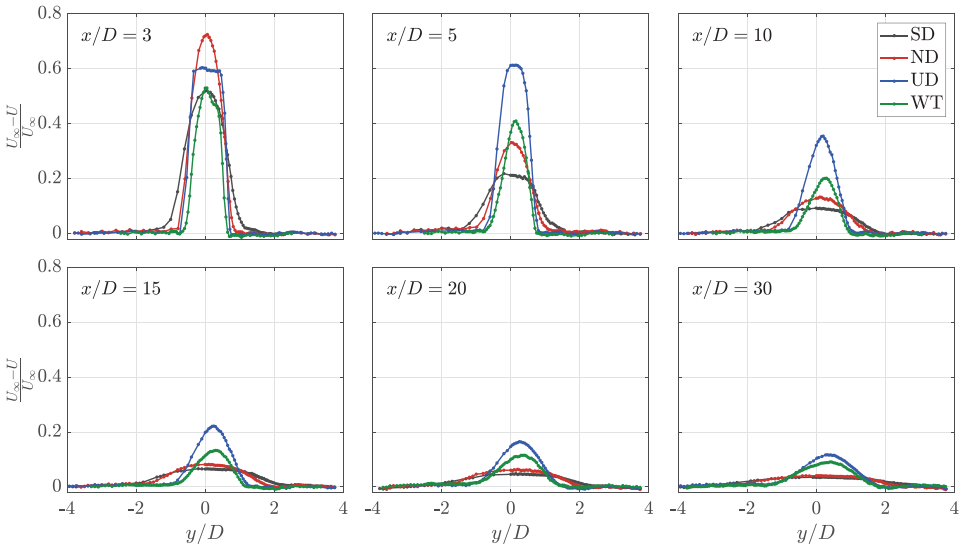

FIG. 8. Velocity deficit profiles at all downstream positions.

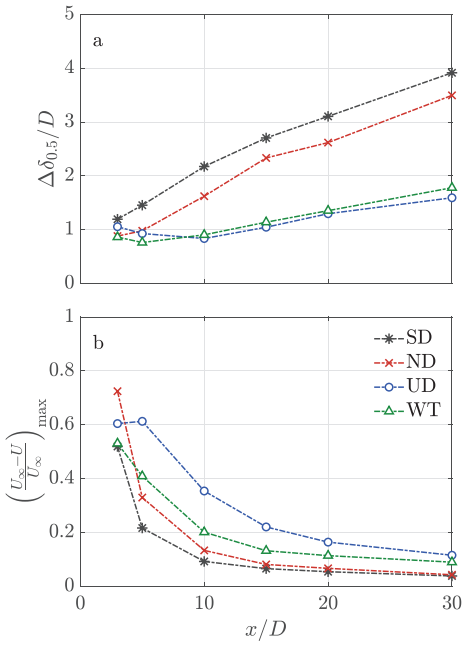

FIG. 9. Evolution of the wake width (a) and velocity deficit (b) at different positions downstream of the wake-generating objects.

wakes. One reason for the discrepancy between the UD wake and WT wake could be the difference in C_D. No comparison to analytical wake models or axisymmetric wake theory has been included in this work. The downward shift of the wake, due to the tower,[56] makes it unfeasible to compare it with a general axisymmetric wake.

The TI profiles of the wakes are shown in Fig. 10. In the center of the SD and ND wakes, at $x = 3D$, the TI is at a level where hot-wires cannot accurately measure it due to backflow events.[60] These magnitudes should therefore be considered with caution. The high turbulence levels enhance the transport of momentum from the freestream into the wake. This explains the rapid wake expansion and reduction of the velocity deficit for the SD and ND, as was shown in Figs. 8 and 9.

On the other hand, the turbulence levels close to the UD are lower, but also decrease much slower. At $x = 3D$, the highest levels of turbulence are found at the edge of the wake, where the velocity gradient is high. In contrast to the SD and ND wakes, the TI is low in the center of the wake. Until $x = 10D$, the maximum TI in the wake stays around the same magnitude, but the peaks located in the shear layer grow in width and at $x = 10D$ they have merged to span the entire wake. Farther downstream, the turbulence decays, although the levels stay higher than for the SD and the ND wakes also for $x > 10D$.

The two PD designs produce wakes with different characteristics, even in the low order statistics. The ND produces several jets of different sizes, as can be seen in the PIV fields in the work by Helvig *et al.*[12] and Thenuissen and Worboys,[52] where the former used disks with very similar design to the ND. The high local velocity gradients in the wake produce turbulent energy; thus, the TI is increased. The high levels of TI increase transport, which spreads the wake and reduces the maximum velocity deficit. The UD has a fine mesh, such that the majority of turbulent production arises in the high shear regions in

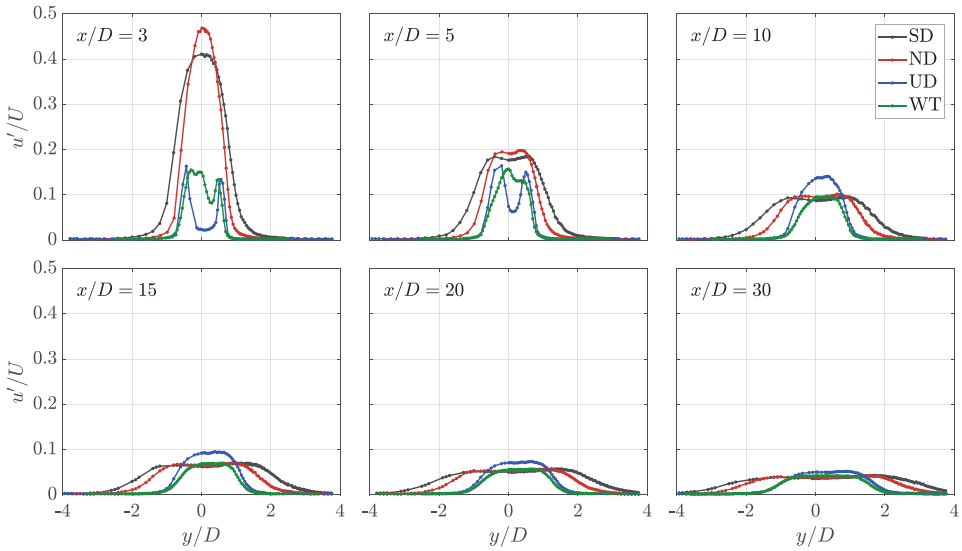

FIG. 10. Turbulence intensity profiles at all downstream positions.

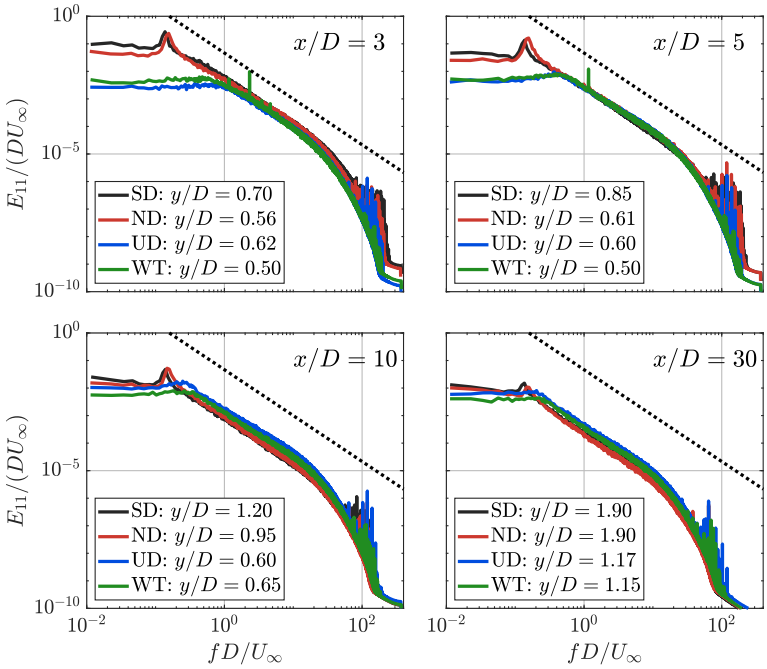

FIG. 11. Velocity spectra at different downstream positions. All spectra are taken at the position where the velocity deficit is closest to half the maximum velocity deficit, i.e., in the shear layer.

the wake. As the high levels of shear extend farther downstream from the disk, production continues farther downstream, maintaining higher levels of turbulence in the far wake.

For the two closest positions, the WT wake has an asymmetric TI profile. This arises from combined effects of the tower wake and the rotation of the turbine wake, and has been reported earlier.[61] At these two positions, the levels of TI are close to the ones in the UD wake. However, the TI is higher than for the UD in the center of the wake. The turbulence also decays more rapidly in the WT wake from $x = 5D$. Figure 8 shows that the velocity gradients in the WT wake are smaller than for the UD, but larger than the wakes behind the other WGOs. The TI profiles demonstrate that the disks are unable to replicate the TI profile in the WT-wake, although the UD does lead to comparable magnitudes of TI, and the wake widths are approximately the same for the two. It should be noted that Helvig *et al.*[12] recently showed that even though the mean profiles of wind turbine and porous disk wakes show reasonable agreement, the instantaneous structures might differ significantly.

B. Velocity spectra

The first- and second-order statistics give valuable insight into the mean wake features. However, they do not give information about the structures in the wake. Such structures are important for loads on downstream turbines.[2] To obtain information about the structure of the wake, the power spectral density of the velocity fluctuations (E_{11}), here referred to as the velocity spectrum, of the wakes was studied. Some selected spectra are shown in Fig. 11. The spectral comparisons have been made at the measurement positions where the velocity deficit is closest to half the maximum velocity deficit in each wake; this is within the shear layer for each flow. By evaluating in the shear layer rather than at the same physical position in each wake, different flow features at the same relative position in the wake can be assessed. For reference, the same comparisons made at the same physical location are presented in Appendix B.

There are distinct low frequency peaks in the velocity spectra for the SD and the ND, which are present all the way to $x = 30D$. The Strouhal numbers, $St = fD/U_\infty$, of the peaks are $St = 0.137$ and $St = 0.150$, respectively, for the two disks. The former corresponds to the expected St of vortex shedding downstream of a circular disk (e.g., Refs. 37, 62, and 63). As the latter is only slightly higher, it is also believed to be the standard vortex shedding for an ND. No distinct peaks are observed in the UD spectra, and there is thus no strong vortex shedding in this wake. This is in agreement with the results reported by Cannon *et al.*,[37] who did not observe vortex shedding in the wake of wire mesh disks when the solidity was less than 60%.

At the closest measurement position, three sharp peaks are observed in the WT spectrum. The first peak has a reduced frequency of $St = 1.159$, which is the rotational frequency of the WT. The two other peaks are at reduced frequencies of 2.320 and 4.640, and are thus harmonics of this first one. For the WT, there is no strong periodic energy associated with vortex shedding for most of the wake, which differs from that present behind SD and ND.

To illustrate the extent of the vortex shedding, spectrograms of different cases have been prepared. A spectrogram is a collection of spectra plotted beside each other, with a colormap indicating the magnitude of energy at the different frequencies. An example spectrogram is shown in Fig. 12(a). The vertical axis shows the frequency,

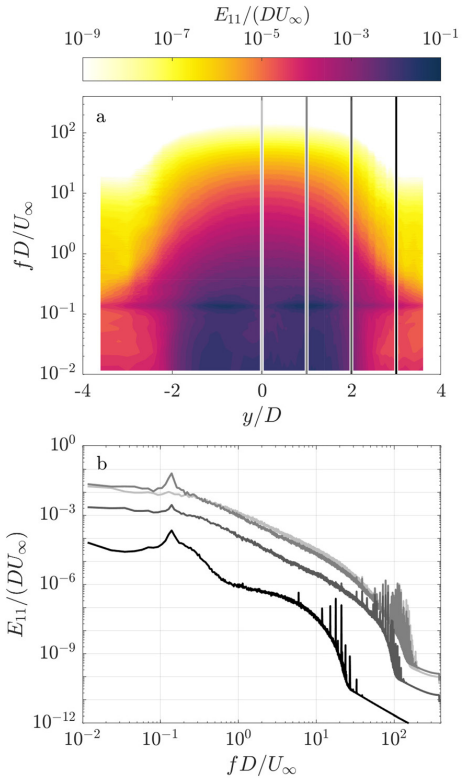

FIG. 12. A graphical explanation of spectrograms. (a) Spectrogram of the SD wake at $x = 10D$. (b) Four spectra plotted in the traditional way, corresponding to the vertical lines in panel (a).

corresponding to the x axis in a conventional plot of a spectrum, while the horizontal axis shows the y-position in the wake. In that sense, each vertical line in Fig. 12(a) is a spectrum, shown in Fig. 12(b) with the respective color. The colormap displays the energy content, thus representing the y axis in a typical spectrum. The spectrograms allow investigation of the spanwise extent of structures in the flow, as well as a direct comparison between the same physical position in the different wakes.

Figure 13 shows spectrograms at representative downstream positions. The velocity spectra integrate to the variance of the velocity, equivalent to the square of the turbulence intensity when the mean velocity is held constant across test cases as done here. Thus, the color intensity of the spectrogram agrees with the TI profiles in Fig. 10. The vortex shedding associated peaks are visible for the SD and ND, highlighted with (i) in the figure, spreading over the entire width of the wake and also some distance outside the high-energy regions. Even $30D$ downstream of the disks, traces of vortex shedding can be seen for both disks. As discussed in relation to Fig. 11, no such vortex

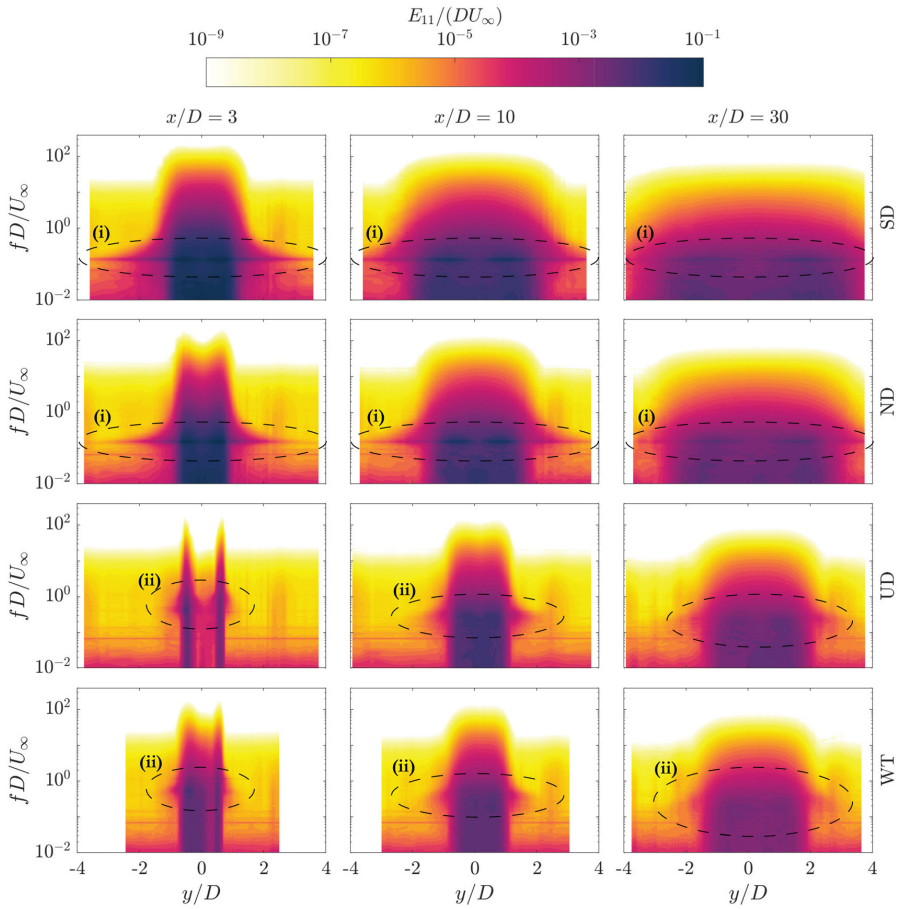

FIG. 13. Spectrograms at representative downstream positions. The dashed ellipses highlight vortex shedding frequencies (i) and instantaneous structures arising from the strong shear (ii).

shedding peak is observed for the UD and WT wakes. However, at the edges of the high-energy regions, a range of energy containing frequencies are present, marked with (ii) in Fig. 13. These frequencies are higher than the vortex shedding frequency. The sharp velocity gradients found here are comparable to mixing layer flows, where coherent structures are known to exist.[64,65] Thus, these high-energy frequencies result from the strong shear in the flow. From this and the results in Sec. IV A, the edges of the wakes downstream of the UD and WT act as mixing layer flows due to the strong shear. The same behavior is not observed for the SD and the ND. An analysis of the spectra reveals that different physical mechanisms govern the different wakes. In particular, it is interesting to observe that the ND leads to vortex shedding in the wake, which is not present in the UD wake. In turn, the UD wake has high-energy structures in the shear layers, although with smaller magnitude than vortex shedding.

C. Velocity skewness and kurtosis

For the structural loads on downstream turbines, it is important to understand the distribution of velocities within the turbulent flow. To that measure, the skewness and kurtosis of the velocity fluctuations can be instructive. Skewness, $\overline{u^3}/\overline{u^2}^{3/2}$, is a measure of the asymmetry of the velocity fluctuation distribution. For negative skew, the extremes of the negative velocity fluctuations are more prominent than the positive ones and vice versa for positive skew. A symmetrical distribution has zero skew.

The skewness of velocity fluctuations at all six measurement positions is shown in Fig. 14. The wakes of both SD and ND have similar skewness profiles throughout the length of the measurements. The magnitude is low in the center of the wake, and the skewness gradually decreases toward a negative peak around the edge of the wake. Then, there is a distinct shift to a positive peak of lower magnitude just outside where the velocity deficit approaches zero. The peak magnitudes are slightly higher for the SD, and as the wake gets wider, they are also farther from the center of the wake.

For the UD, the same inner negative and the outer positive peaks as observed in the SD and ND wake are present, however, with smaller magnitude. In particular, the outermost positive peak is smaller. For $x = 3D$ and $x = 5D$, there are also positive peaks near the center of the wake. Qualitatively, this agrees with the results Aubrun *et al.*[46] reported for a wire mesh disk at $x = 3D$. A more detailed comparison with those results is not feasible, as their TI (4%) is much higher than the one used in the present work, the solidity of their disk is different, and their disk is not uniform near the center. Farther downstream, the profiles have the same shape as the SD and the ND, but the peaks are smaller in magnitude and are more closely spaced, following from the smaller wake size observed in the lower order velocity statistics.

The fourth-order moment, $\overline{u^4}/\overline{u^2}^2$, referred to as the kurtosis or the flatness of the velocity fluctuation distribution, is another descriptor of the turbulent velocity distribution. The higher the kurtosis, the stronger the tails are. For reference, a Gaussian distribution has a kurtosis of 3 and 0 skewness. If the magnitude of the skewness is large, the kurtosis must also be large, as one of the tails becomes stronger. In Fig. 15, the kurtosis of all the measurement series is shown. There are high levels of kurtosis around the edges of all wakes at all positions. In turn, this means that the turbulence around the edges of the wake is dominated by extreme events. In the center of the wake, the distribution is close to Gaussian. It should also be noted that the magnitude of kurtosis is higher for the SD and ND than for the UD and WT, showing that extreme velocity deficits happen more often in the wakes of the former disks. It is also worth noting that $3D$ and $5D$ downstream of the UD, there are increased levels of kurtosis in the center of the wake.

There is a clear asymmetry in the skewness and kurtosis profiles of the WT wake at $x = 3D$ and $x = 5D$. The magnitude of both statistics is higher for negative y-values. From $10D$ downstream of the turbine, the asymmetry shifts side, with higher peaks for positive y-values. From this distance, the asymmetry gradually decreases, and the skewness and kurtosis approach the profiles measured in the wake of the UD. This asymmetry is not replicated by any of the disks, but it should not be expected that a static, symmetric disk produces an asymmetric wake. Earlier comparisons of the wake of PDs and wind turbines do not report this asymmetry, but they also only evaluate one side of the wake.[46,47] The interaction between a rotating wake and the wake of the tower is a possible explanation for this asymmetry.

It is noticeable that the magnitudes of both skewness and kurtosis, for all the WGOs, are high at the very edge of the wake, where the TI approaches zero. In this region, bursts of high velocity occur in the flow, increasing the forces acting on downstream turbines. Thus, in agreement with Schottler *et al.*,[66] the wake is wider than what can be seen in the mean velocity and TI profiles. The turbulence in this outer part of the wake is defined by rare extreme events. For the SD and the ND, these extreme events occur at the very edge of the vortex shedding peak observed in the spectrograms in Fig. 13, and thus have some periodicity. The same periodicity is not present in the edges of the UD and

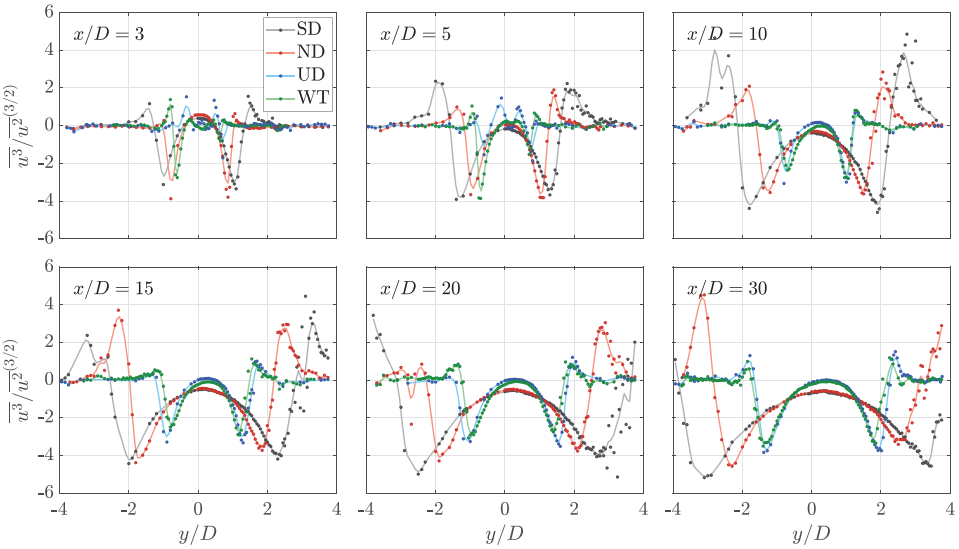

FIG. 14. Profiles of the skewness at all downstream positions. Due to high scatter around the edge of the wake, the solid lines are weighted averages of interpolated data points.

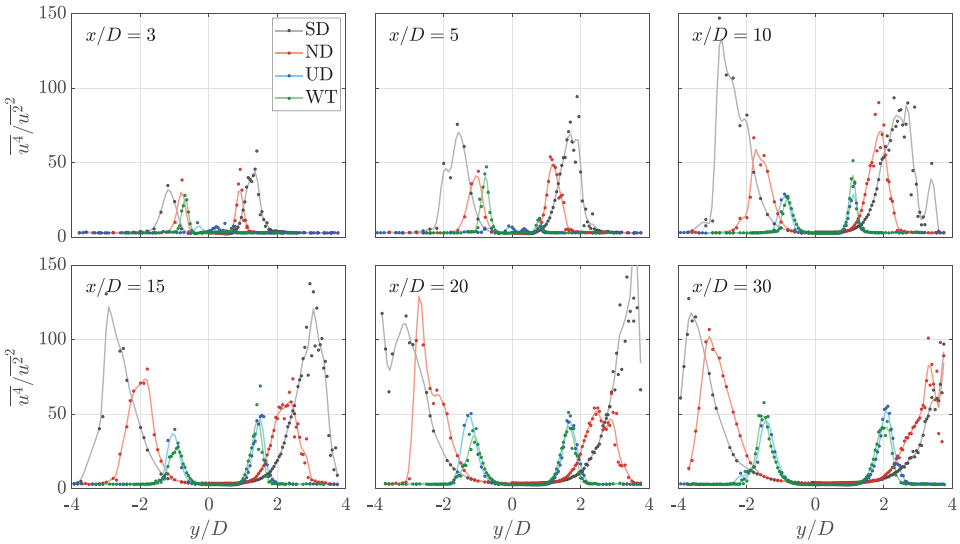

FIG. 15. Profiles of kurtosis at all downstream positions. Due to high scatter around the edge of the wake, the solid lines are weighted averages of interpolated data points.

WT wakes. The lack of vortex shedding might thus be the reason for the lower magnitude of the skewness peaks. In Fig. 16, probability density functions (PDFs) are shown for all WGOs at a streamwise position of $x = 10D$. Both the geometrical centerline and the position of maximum negative skewness are shown. The latter was chosen as a criterion to evaluate a comparable position in the wake of each WGO, instead of choosing a certain y-position in different parts of the wake. At the maximum negative skewness position, the velocity deficit is on the order of 1% or less for all the wakes. The TI is also below 40% of the maximum TI for the respective WGO at the current streamwise position. The geometrical centerline has turbulence levels close to the maximum for each object. The negative tails of the PDF are larger for the position at the edge of the wake than for the centerline position, despite the low velocity deficit and the lower values of TI. Thus, the extreme turbulent bursts have the same magnitude where the velocity deficit approaches zero, as in the center of the wake. The large tails of the PDFs demonstrate that it is important to be able to represent the higher-order turbulent statistics when choosing a wind turbine model. For reference, the PDFs at the same physical locations are presented in Appendix B, but this does not change the findings presented above.

V. CONCLUSIONS

The wakes of two porous disks, one energy extracting wind turbine and a solid disk, have been assessed with hot-wire anemometry. The main focus has been on the differences in the wakes downstream of two different static porous disks and how they replicate the wake of a rotating wind turbine model. The solid disk was included as a

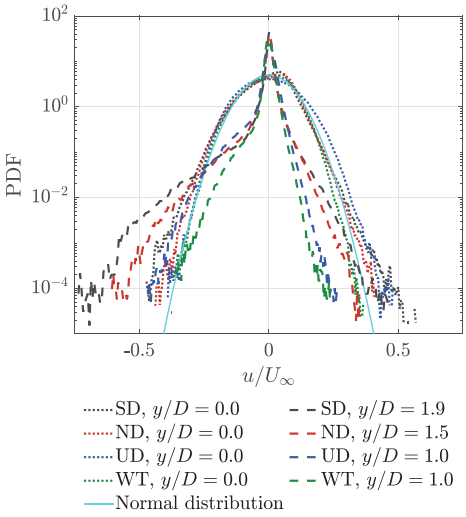

FIG. 16. Probability density functions of the velocity fluctuations at $x = 10D$. y/D-positions are at the centerline and at the position of maximum negative skewness. The PDFs have been normalized by the incoming velocity rather than the standard deviation, such that the strength of the fluctuations is comparable between the curves.

reference case. The presented measurements compare two common actuator disk configurations with a rotating model at downstream distances up to 30*D*, which is significantly farther downstream than presently available in the literature.

The results highlight the importance of choosing the right porous disk design. In particular, it is found that for two disks with the same solidity, only one leads to vortex shedding in the wake. The nonuniform disk produces vortex shedding, whereas no such phenomenon is observed in the wake downstream of the uniform disk. Furthermore, the velocity deficit and turbulence intensity profiles differ between the disks. The wake downstream of the nonuniform disk is highly turbulent. The high turbulence intensity increases transport, spreading the wake. On the other hand, the uniform disk has little turbulence in the near wake, but rather sharp velocity gradients. The velocity gradients lead to turbulence production, increasing and maintaining higher turbulence levels in the far wake. Thus, the uniform disk has a smaller wake, with higher velocity deficits and higher turbulence intensity in the far wake. The evolution of velocity deficit and turbulence intensity is also different between the disks. The skewness and kurtosis profiles differ between the two disks, with higher magnitudes in the nonuniform disk wake. The governing physics in the two disk wakes are thus significantly different, and the differences persist throughout the measurement domain up to 30*D* downstream of the disks.

The wake of the wind turbine is asymmetric, which cannot be replicated by any of the static disks. This asymmetry is present even in far wakes, more prominently for higher-order velocity statistics. Apart from the asymmetry, the uniform disk leads to a wake that is a closer replication of the wind turbine wake. The instantaneous structures and the shape and magnitude of velocity statistics are a better match. The two actuator disks in this study were chosen as examples of disks used in the literature and are not designed to replicate the wake of the particular wind turbine used in this study. They proved to be good choices to evaluate different flow features in porous disk wakes, giving an overview of different flow physics that must be taken into account in actuator disk design processes. Nonetheless, care must be taken when extrapolating these results to other specific disks, because, as we have illustrated, the wake and its evolution are highly dependent on the geometry.

ACKNOWLEDGMENTS

The authors thank Hauk-Morten Heimlund Lykke for helping in preparing and performing the experiments.

AUTHOR DECLARATIONS

Conflict of Interest

The authors have no conflicts to disclose.

DATA AVAILABILITY

The data that support the findings of this study are openly available in the NTNU Open Research Data repository at https://doi.org/10.18710/FFELKX.

APPENDIX A: SELF-NORMALIZED WAKE PROFILES

Figures 17 and 18 show the self-normalized velocity deficit and turbulence intensity, respectively. This form of normalization places emphasis on the comparison of the shape of the wakes by effectively removing the magnitude from the comparison. From both Figs. 17 and 18, it is evident that the shape of the UD and WT is generally comparable, at least for $x/D \geq 10$. The ND and SD have

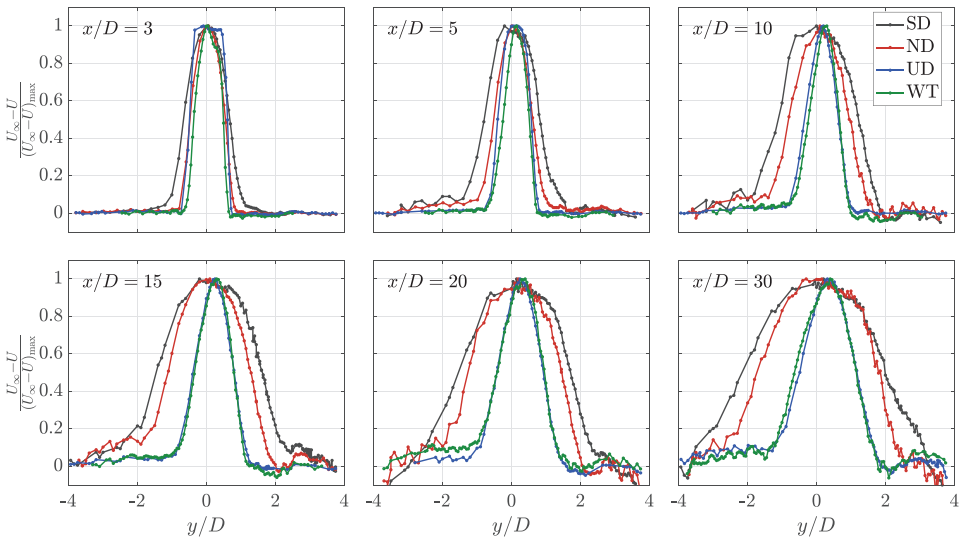

FIG. 17. Self-normalized velocity deficit.

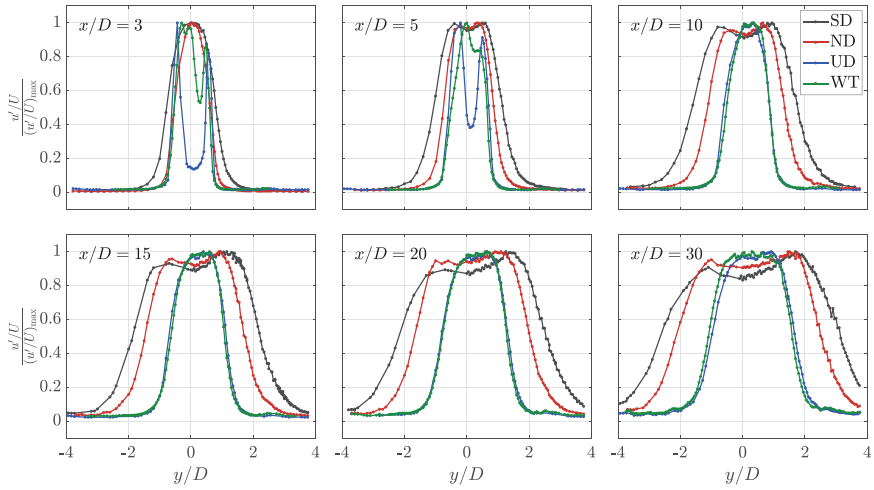

FIG. 18. Self-normalized turbulence intensity.

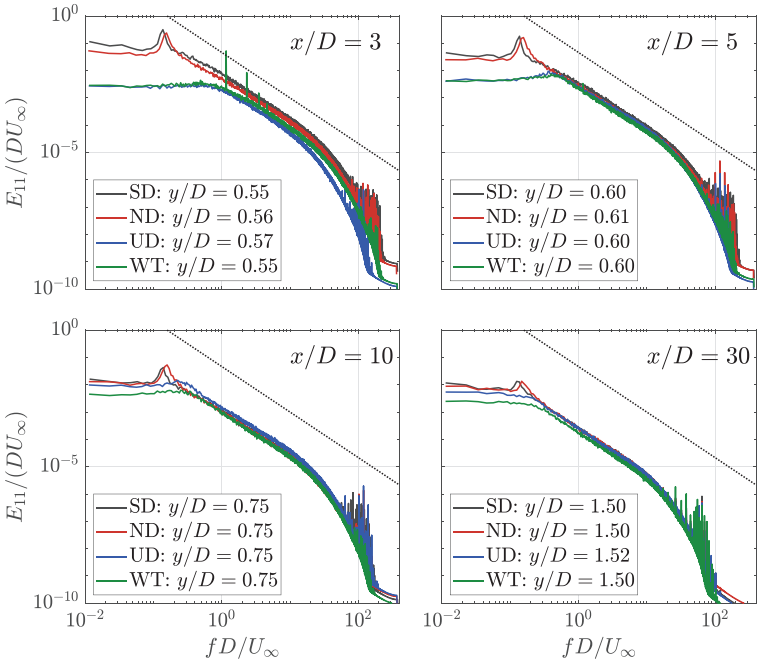

FIG. 19. Velocity spectra at different downstream positions. Spectra are taken at a location approximately centered between the position where the velocity deficit is half the maximum velocity deficit for the ND and the UD. The straight solid line represents a reference $f^{-5/3}$ curve.

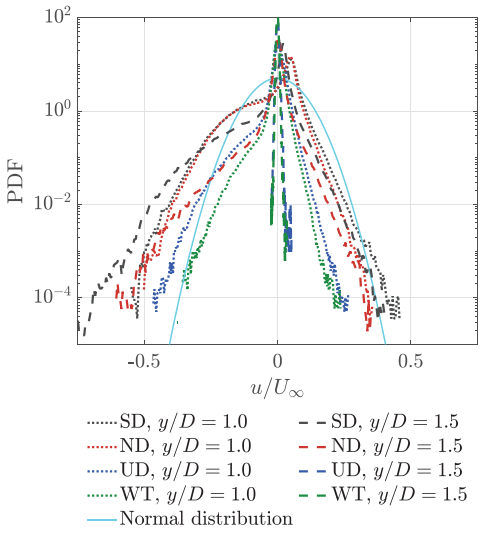

FIG. 20. Probability density functions of the velocity fluctuations at $x = 10D$. The PDFs have been normalized by the incoming velocity rather than the standard deviation, such that the strength of the fluctuations is comparable between the curves.

distinctively different shapes, generally with a wider wake, but are more comparable to each other than to the UD and WT. These curves complement those provided in the main text where the magnitude is also incorporated.

APPENDIX B: ADDITIONAL VELOCITY SPECTRA AND PDFS

Figure 11 shows the velocity spectra at the position where the velocity deficit is half the maximum velocity deficit. It is also interesting to compare spectra at the same physical position. This is done in Fig. 19, at a position approximately centered between the ND and UD positions in Fig. 11. The two figures show the same energy containing frequencies. There are some small changes in the energy content, but that is to be expected, as the TI differs between the positions. In sum, comparing the spectra as in Fig. 19 does not change the results and conclusions presented in the body of this work.

In the same manner, PDFs plotted at $y/D = 1$ and $y/D = 1.5$ are shown in Fig. 20 to allow a direct comparison at the same physical location. For both y-positions, the streamwise position is $x/D = 10$. At $y/D = 1.5$, the measurement position is outside the UD and WT wakes, and thus the TI is low. Therefore, these positions have very narrow velocity distributions. The clear asymmetry of the other profiles shows the skewness of the flow, while the large tails, in particular, for the SD and ND wakes, show the high kurtosis of the velocity distribution.

REFERENCES

[1]R. J. Barthelmie and L. E. Jensen, "Evaluation of wind farm efficiency and wind turbine wakes at the Nysted offshore wind farm," Wind Energy **13**, 537–586 (2010).
[2]K. Thomsen and P. Sørensen, "Fatigue loads for wind turbines operating in wakes," J. Wind Eng. Ind. Aerodyn. **80**, 121–136 (1999).
[3]L. J. Vermeer, J. N. Sørensen, and A. Crespo, "Wind turbine wake aerodynamics," Prog. Aerosp. Sci. **39**, 467–510 (2003).
[4]D. Medici and P. H. Alfredsson, "Measurements on a wind turbine wake: 3D effects and bluff body vortex shedding," Wind Energy **9**, 219–236 (2006).
[5]W. Zhang, C. D. Markfort, and F. Porté-Agel, "Near-wake flow structure downwind of a wind turbine in a turbulent boundary layer," Exp. Fluids **52**, 1219–1235 (2012).
[6]R. J. Stevens and C. Meneveau, "Flow structure and turbulence in wind farms," Annu. Rev. Fluid Mech. **49**, 311–339 (2017).
[7]F. Porté-Agel, M. Bastankhah, and S. Shamsoddin, "Wind-turbine and wind-farm flows: A review," Boundary Layer Meteorol. **174**, 1–59 (2020).
[8]F. Porté-Agel, Y. T. Wu, and C. H. Chen, "A numerical study of the effects of wind direction on turbine wakes and power losses in a large wind farm," Energies **6**, 5297–5313 (2013).
[9]J. F. Manwell, J. G. McGowan, and A. L. Rogers, *Wind Energy Explained: Theory, Design and Application* (John Wiley and Sons, Ltd., Chichester, UK, 2009).
[10]Y.-T. Wu and F. Porté-Agel, "Large-eddy simulation of wind-turbine wakes: Evaluation of turbine parametrisations," Boundary Layer Meteorol. **138**, 345–366 (2011).
[11]Y.-T. Wu and F. Porté-Agel, "Simulation of turbulent flow inside and above wind farms: model validation and layout effects," Boundary Layer Meteorol. **146**, 181–205 (2013).
[12]S. de Jong Helvig, M. K. Vinnes, A. Segalini, N. A. Worth, and R. J. Hearst, "A comparison of lab-scale free rotating wind turbines and actuator disks," J. Wind Eng. Ind. Aerodyn. **209**, 104485 (2021).
[13]M. Gaumond, P.-E. Réthoré, S. Ott, A. Peña, A. Bechmann, and K. S. Hansen, "Evaluation of the wind direction uncertainty and its impact on wake modeling at the Horns Rev offshore wind farm," Wind Energy **17**, 1169–1178 (2014).
[14]K. S. Hansen, P.-E. Réthoré, J. Palma, B. G. Hevia, J. Prospathopoulos, A. Peña, S. Ott, G. Schepers, A. Palomares, M. P. van der Laan, and P. Volker, "Simulation of wake effects between two wind farms," J. Phys.: Conf. Ser. **625**, 012008 (2015).
[15]P. Argyle, S. Watson, C. Montavon, I. Jones, and M. Smith, "Modelling turbulence intensity within a large offshore wind farm," Wind Energy **21**, 1329–1343 (2018).
[16]P. A. Fleming, A. Ning, P. M. O. Gebraad, and K. Dykes, "Wind plant system engineering through optimization of layout and yaw control," Wind Energy **19**, 329–344 (2016).
[17]J. Meyers and C. Meneveau, "Optimal turbine spacing in fully developed wind farm boundary layers," Wind Energy **15**, 305–317 (2012).
[18]R. J. Stevens, D. F. Gayme, and C. Meneveau, "Large eddy simulation studies of the effects of alignment and wind farm length," J. Renewable Sustainable Energy **6**, 023105 (2014).
[19]J. P. Goit and J. Meyers, "Optimal control of energy extraction in wind-farm boundary layers," J. Fluid Mech. **768**, 5–50 (2015).
[20]J. P. Goit, W. Munters, and J. Meyers, "Optimal coordinated control of power extraction in LES of a wind farm with entrance effects," Energies **9**, 29 (2016).
[21]N. O. Jensen, "A note on wind generator interaction," Technical Report No. Risø-M-2411 (Risø National Laboratory, Roskilde, 1983).
[22]S. Frandsen, R. Barthelmie, S. Pryor, O. Rathmann, S. Larsen, J. Højstrup, and M. Thøgersen, "Analytical modelling of wind speed deficit in large offshore wind farms," Wind Energy **9**, 39–53 (2006).
[23]M. Bastankhah and F. Porté-Agel, "A new analytical model for wind-turbine wakes," Renewable Energy **70**, 116–123 (2014).
[24]P. Doubrawa, R. J. Barthelmie, H. Wang, and M. J. Churchfield, "A stochastic wind turbine wake model based on new metrics for wake characterization," Wind Energy **20**, 449–463 (2017).
[25]W. C. Cheng and F. Porté-Agel, "A simple physically-based model for wind-turbine wake growth in a turbulent boundary layer," Boundary Layer Meteorol. **169**, 1–10 (2018).
[26]M. Bastankhah, B. L. Welch, L. A. Martínez-Tossas, J. King, and P. Fleming, "Analytical solution for the cumulative wake of wind turbines in wind farms," J. Fluid Mech. **911**, 53 (2021).

[27]G. España, S. Aubrun, S. Loyer, and P. Devinant, "Spatial study of the wake meandering using modelled wind turbines in a wind tunnel," Wind Energy **14**, 923–937 (2011).
[28]G. España, S. Aubrun, S. Loyer, and P. Devinant, "Wind tunnel study of the wake meandering downstream of a modelled wind turbine as an effect of large scale turbulent eddies," J. Wind Eng. Ind. Aerodyn. **101**, 24–33 (2012).
[29]Y.-A. Muller, S. Aubrun, and C. Masson, "Determination of real-time predictors of the wind turbine wake meandering," Exp. Fluids **56**, 53 (2015).
[30]M. F. Howland, J. Bossuyt, L. A. Martínez-Tossas, J. Meyers, and C. Meneveau, "Wake structure in actuator disk models of wind turbines in yaw under uniform inflow conditions," J. Renewable Sustainable Energy **8**, 043301 (2016).
[31]A. Abdulrahim, M. T. Akpolat, A. Hassanein, M. Perçin, and O. Uzol, "Effects of inflow boundary layer on the wake of a radially non-uniform porous disk," J. Renewable Sustainable Energy **13**, 033302 (2021).
[32]W. Yu, V. W. Hong, C. Ferreira, and G. A. M. van Kuik, "Experimental analysis on the dynamic wake of an actuator disc undergoing transient loads," Exp. Fluids **58**, 149 (2017).
[33]W. Yu, C. Ferreira, and G. A. van Kuik, "The dynamic wake of an actuator disc undergoing transient load: A numerical and experimental study," Renewable Energy **132**, 1402–1414 (2019).
[34]R. Theunissen, P. Housley, C. B. Allen, and C. Carey, "Experimental verification of computational predictions in power generation variation with layout of offshore wind farms," Wind Energy **18**, 1739–1757 (2015).
[35]J. Bossuyt, M. F. Howland, C. Meneveau, and J. Meyers, "Measurement of unsteady loading and power output variability in a micro wind farm model in a wind tunnel," Exp. Fluids **58**, 1 (2017).
[36]P. M. Sforza, P. Sheerin, and M. Smorto, "Three-dimensional wakes of simulated wind turbines," AIAA J. **19**, 1101–1107 (1981).
[37]S. Cannon, F. Champagne, and A. Glezer, "Observations of large-scale structures in wakes behind axisymmetric bodies," Exp. Fluids **14**, 450 (1993).
[38]H. Higuchi, J. Zhang, S. Furuya, and B. K. Muzas, "Immediate and near wake flow patterns behind slotted disks," AIAA J. **36**, 1626–1634 (1998).
[39]L. E. Myers and A. S. Bahaj, "Experimental analysis of the flow field around horizontal axis tidal turbines by use of scale mesh disk rotor simulators," Ocean Eng. **37**, 218–227 (2010).
[40]M. Lin, C. Xie, M. Yao, and J. Yang, "Study on the near wake of a honeycomb disk," Exp. Therm. Fluid Sci. **81**, 33–42 (2017).
[41]H. Xiao, L. Duan, R. Sui, and T. Roesgen, "Experimental investigations of turbulent wake behind porous disks," in Proceedings of the 1st Marine Energy Technology Symposium, Washington DC (2013).
[42]M. H. Ranjbar, H. Zanganeh Kia, S. A. Nasrazadani, K. Gharali, and J. Nathwani, "Experimental and numerical investigations of actuator disks for wind turbines," Energy Sci. Eng. **8**, 2371–2386 (2020).
[43]M. Huang, C. Ferreira, A. Sciacchitano, and F. Scarano, "Wake scaling of actuator discs in different aspect ratios," Renewable Energy **183**, 866–876 (2022).
[44]L. A. Martínez-Tossas, M. J. Churchfield, and S. Leonardi, "Large eddy simulations of the flow past wind turbines: Actuator line and disk modeling," Wind Energy **18**, 1047–1060 (2015).
[45]N. Simisiroglou, S.-P. P. Breton, and S. Ivanell, "Validation of the actuator disc approach using small-scale model wind turbines," Wind Energy Sci. **2**, 587–601 (2017).
[46]S. Aubrun, S. Loyer, P. Hancock, and P. Hayden, "Wind turbine wake properties: Comparison between a non-rotating simplified wind turbine model and a rotating model," J. Wind Eng. Ind. Aerodyn. **120**, 1–8 (2013).
[47]L. E. Lignarolo, D. Ragni, C. J. Ferreira, and G. J. Van Bussel, "Experimental comparison of a wind-turbine and of an actuator-disc near wake," J. Renewable Sustainable Energy **8**, 023301 (2016).
[48]I. Neunaber, "Stochastic investigation of the evolution of small-scale turbulence in the wake of a wind turbine exposed to different inflow conditions," Ph.D. thesis (Carl von Ossietzky Universität Oldenburg, 2019).
[49]I. Neunaber, M. Hölling, J. Whale, and J. Peinke, "Comparison of the turbulence in the wakes of an actuator disc and a model wind turbine by higher order statistics: A wind tunnel study," Renewable Energy **179**, 1650–1662 (2021).
[50]E. H. Camp and R. B. Cal, "Mean kinetic energy transport and event classification in a model wind turbine array versus an array of porous disks: Energy budget and octant analysis," Phys. Rev. Fluids **1**, 044404 (2016).
[51]E. H. Camp and R. B. Cal, "Low-dimensional representations and anisotropy of model rotor versus porous disk wind turbine arrays," Phys. Rev. Fluids **4**, 024610 (2019).
[52]R. Theunissen and R. Worboys, "Near-wake observations behind azimuthally perforated disks with varying hole layout and porosity in smooth airstreams at high Reynolds numbers," J. Fluids Eng. **141**, 051108 (2019).
[53]S. Aubrun, M. Bastankhah, R. B. Cal, B. Conan, R. J. Hearst, D. Hoek, M. Hölling, M. Huang, C. Hur, B. Karlsen, I. Neunaber, M. Obligado, J. Peinke, M. Percin, L. Saetran, P. Schito, B. Schliffke, D. Sims-Williams, O. Uzol, M. K. Vinnes, and A. Zasso, "Round-robin tests of porous disc models," J. Phys.: Conf. Ser. **1256**, 012004 (2019).
[54]R. W. Fox, A. T. McDonald, P. J. Pritchard, and J. W. Mitchell, *Fluid Mechanics*, 9th ed. (Wiley, 2016).
[55]S. Gambuzza and B. Ganapathisubramani, "The effects of free-stream turbulence on the performance of a model wind turbine," J. Renewable Sustainable Energy **13**, 023304 (2021).
[56]F. Pierella and L. Sætran, "Wind tunnel investigation on the effect of the turbine tower on wind turbines wake symmetry," Wind Energy **20**, 1753–1769 (2017).
[57]M. Hultmark and A. J. Smits, "Temperature corrections for constant temperature and constant current hot-wire anemometers," Meas. Sci. Technol. **21**, 105404 (2010).
[58]J. Bartl and L. Saetran, "Blind test comparison of the performance and wake flow between two in-line wind turbines exposed to different turbulent inflow conditions," Wind Energy Sci. **2**, 55–76 (2017).
[59]L. Zhan, S. Letizia, and G. Valerio Iungo, "LiDAR measurements for an onshore wind farm: Wake variability for different incoming wind speeds and atmospheric stability regimes," Wind Energy **23**, 501–527 (2020).
[60]F. E. Jørgensen, "How to measure turbulence with hot-wire anemometers—A practical guide," Technical Report No. 9040U6154 (Dantec Dynamics, 2005).
[61]C. Santoni, K. Carrasquillo, I. Arenas-Navarro, and S. Leonardi, "Effect of tower and nacelle on the flow past a wind turbine," Wind Energy **20**, 1927–1939 (2017).
[62]J. J. Miau, T. S. Leu, T. W. Liu, and J. H. Chou, "On vortex shedding behind a circular disk," Exp. Fluids **23**, 225–233 (1997).
[63]P. W. Bearman and M. Takamoto, "Vortex shedding behind rings and discs related content vortex shedding behind rings and discs," Fluid Dynamics Research **3**, 1–4 (1988).
[64]C. D. Winant and F. K. Browand, "Vortex pairing: The mechanism of turbulent mixing-layer growth at moderate Reynolds number," J. Fluid Mech. **63**, 237–255 (1974).
[65]M. Kamruzzaman, "On the effects of non-homogeneity on small scale turbulence," Ph.D. thesis (The University of Newcastle, Australia, 2016).
[66]J. Schottler, J. Bartl, F. Mühle, L. Sætran, J. Peinke, and M. Hölling, "Wind tunnel experiments on wind turbine wakes in yaw: Redefining the wake width," Wind Energy Sci. **3**, 257–273 (2018).

Article II

Characterizing porous disk wakes in different turbulent inflow conditions with higher-order statistics

Magnus K. Vinnes, Ingrid Neunaber, Hauk-Morten H. Lykke, R. Jason Hearst

Under consideration for publication in:
Experiments in Fluids

This paper is under consideration for publication and is therefore not included.

Article III

A comparison of lab-scale free rotating wind turbines and actuator disks

Sanne de Jong Helvig, Magnus K. Vinnes, Antonio Segalini, Nicholas A. Worth, R. Jason Hearst

Published in:
Journal of Wind Engineering & Industrial Aerodynamics, ***209****, 104485, (2021)*

Journal of Wind Engineering & Industrial Aerodynamics 209 (2021) 104485

Contents lists available at ScienceDirect

Journal of Wind Engineering & Industrial Aerodynamics

journal homepage: www.elsevier.com/locate/jweia

A comparison of lab-scale free rotating wind turbines and actuator disks

Sanne de Jong Helvig [a], Magnus K. Vinnes [a], Antonio Segalini [b], Nicholas A. Worth [a], R. Jason Hearst [a,*]

[a] Department of Energy & Process Engineering, Norwegian University of Science & Technology, NO-7491, Trondheim, Norway
[b] Linné Flow Centre, STandUP for Wind, KTH Mechanics, Stockholm, Sweden

ARTICLE INFO

Keywords:
Wind turbine
Actuator disk
Lab-scale
POD

ABSTRACT

Planar particle image velocimetry was conducted upstream and in the near-wake of a lab-scale free-rotating wind turbine model and compared to several actuator disks with the same dimensions. The Reynolds number of the incoming flow is order 10^4. Actuator disks with different designs and solidities were tested, and the process of actuator disk selection is explicitly shown. The drag, mean velocity and mean vorticity in the wake of the disks were compared to that of the rotating model. For the disk that was the best match, the Reynolds stresses and swirling strength are also presented. The instantaneous swirling strength illustrated that despite similar mean fields, the instantaneous phenomena were significantly different. Distinct tip vortices were present in the wake of the rotating model but were absent from the wake of the actuator disk. Proper orthogonal decomposition was used to further investigate the underlying phenomena in the two flows, again demonstrating the importance of tip vortices when studying the rotating model and the lack of such distinct vortices when using the actuator disk. Hence, despite well-matched mean characteristics, the instantaneous structures in the two flows remain distinct.

1. Introduction

Renewable energy now accounts for a third of global power capacity, and, according to Siemens (2019), wind power alone may represent one third of the global electric demand by 2040. Placing wind turbines in wind farms is the most economic and efficient implementation with respect to planning, maintenance and use of land and infrastructure. However, it means that the turbines are permanently exposed to the wakes caused by upstream rows of turbines, and hence, Veers et al. (2019) stated that the first grand challenge in wind energy research today is to improve the understanding of wind farm flow physics. Porté-Agel et al. (2019) also described the importance of further developing models for wind farm wake flow studies and extending these studies to include factors such as topography, thermal stability and the role of atmospheric turbulence. Moreover, in their 'future perspectives', Porté-Agel et al. (2019) emphasised the need for continued wind tunnel testing "to provide further physical insight on the flow, and to guide the improvement, calibration and validation of […] numerical models".

Field tests of wind farms have been, and continue to be, carried out (Barthelmie and Jensen, 2010; Smith et al., 2013; Barthelmie et al., 2015; Zhan et al., 2019, 2020), but such approaches are expensive, difficult and, by their nature, incapable of being completely controlled, unlike lab-scale experiments. Using small-scale models makes it possible to study wind farms in a wind tunnel. Lab-scale experiments are thus helpful in providing a deeper understanding of large scale physics at a range of different conditions, e.g., different incoming flow velocities and turbulence levels (Hearst and Ganapathisubramani, 2017; Li et al., 2020). Multiple small-scale wind farm experiments have already been performed (Theunissen et al., 2015; Camp and Cal, 2016, 2019; Bossuyt et al., 2017; Segalini and Dahlberg, 2020), providing new knowledge of wind farm flows and how to improve wind farm efficiency (Stevens and Meneveau, 2017). However, the complexity of constructing and using numerous rotating turbine models is challenging, which is why, on occasion, simplifications are sought.

The actuator disk is a common simplification of a rotating blade, horizontal-axis wind turbine, used both in experiments and simulations. The simple structure of a static actuator disk is easier to simulate than the blades of a moving rotor, allowing for fewer grid cells, which can have larger dimensions, and hence allowing for larger time steps. In turn, the simulations are not as computationally intensive. Stevens and Meneveau (2014) used actuator disks in simulations to study the effect of wind-input variability on wind farm power fluctuations. Later, Stevens et al. (2014) used actuator disks when simulating and studying row alignment in wind farms. Wu and Porté-Agel (2012) used actuator disk

* Corresponding author.
E-mail address: jason.hearst@ntnu.no (R.J. Hearst).

https://doi.org/10.1016/j.jweia.2020.104485
Received 15 June 2020; Received in revised form 13 November 2020; Accepted 4 December 2020
Available online 23 December 2020

simulations to study atmospheric turbulence effects on wind turbine wakes. Work has been done on testing and further developing the actuator disk as a simulation tool, and comparing the simulations to experimental results (Harrison et al., 2010; Wu and Porté-Agel, 2011; Martínez Tossas et al., 2014; Lignarolo et al., 2016a; Simisiroglou et al., 2017). Static actuator disks are also easier and less costly to manufacture en masse for use in experiments, and often more robust than using moving parts. Blackmore et al. (2013) used actuator disks as a simplification for tidal turbines to study the effect of turbulence on drag force in a water current. Howland et al. (2016) examined the deflection and morphology of wakes behind an actuator disk model of a wind turbine operating in yawed conditions. Bossuyt et al. (2017) used actuator disks to model different wind farm layouts to examine unsteady loading. Theunissen et al. (2015) conducted actuator disk wind farm experiments as a validation, and possible source of improvement, of the actuator disk as a computational tool. While the actuator disk is shown to be a common and convenient simplification, how well actuator disks replicate the behavior of rotating turbines, and how much of an influence the actuator disk geometry has, is still being established.

Actuator disks are typically designed to resemble a specific rotating wind turbine, by matching the diameter of the disk with the diameter of the rotor, and by matching the drag coefficient (sometimes referred to as the "thrust coefficient" in wind turbine literature). Besides that, there are to date no standards in terms of actuator disk design and production. Camp and Cal (2016, 2019), Bossuyt et al. (2017) and Neunaber (2018) used designs with a solidity that decreases with radial coordinate. Aubrun et al. (2013), and later Lignarolo et al. (2014, 2016b), used fine metal meshes with varying porosity at the center of the disk and the outer edge. Blackmore et al. (2013) used a pattern of circular, equally sized holes to maintain approximately uniform porosity across the radius. Sforza et al. (1981) made their actuator disks from perforated metal plates, while Pierella and Sætran (2010) used wooden grids, and Myers and Bahaj (2010) used thin sheets of PVC plastic to create mesh disks. Different actuator disk designs are essentially used interchangeably. Aubrun et al. (2019) conducted a round-robin test of actuator disks, comparing a mesh disk to a non-uniform disk with radially decreasing solidity. They showed that the disks are not overly comparable, and that the variation across facilities is quite large. Theunissen and Worboys (2018) examined the effect of hole topology on the produced drag and near-wake characteristics of actuator disks. With the exception of Aubrun et al. (2019) and Theunissen and Worboys (2018), few comparisons between the different disk design layouts have been conducted, and when actuator disks are used in experiments, the process of actuator disk selection is rarely explicit. The employed disk is simply said to have a certain design, and to match the two previously mentioned criteria of disk diameter and produced drag. Developing a standard actuator disk design which produces the desired wake would be both efficient and practical in order to create uniformity and comparability between experiments. In order to do so, however, more knowledge on the flow field behind actuator disks is needed, which is the focus herein.

After creating an actuator disk that matches the diameter and the produced drag, previous studies have examined the similarity of the flow field behind the actuator disk and the rotating model. The main question has been whether the wake can be properly modeled in the absence of the rotational momentum induced by rotating blades (Neunaber, 2018). Aubrun et al. (2013) used hot-wire measurements, and found that the wake of a rotating model and their porous disk in a modeled atmospheric boundary layer were indistinguishable at 3D downstream. A comparison at low turbulence inflow was also acceptable. Lignarolo et al. (2016b) conducted Particle Image Velocimetry (PIV) measurements in the wakes of both models. They showed that by matching the diameter and drag coefficient, the energy coefficient, velocity, pressure, enthalpy field and wake expansion matched, even in the absence of inflow turbulence. However, differences were found in terms of turbulence intensity and turbulent mixing within their field of view, stretching to 2.18D downstream, due to the presence of tip vortices behind the rotating model. They concluded that the wakes are in good agreement, and suggested the possibility to extend the use of the actuator disk model into the very near wake, given that turbulent mixing is correctly represented. Camp and Cal (2016) found that the mean kinetic energy transport in the far wake is adequately represented by the actuator disk, however in the near wake, significant discrepancies exist in the areas where rotation is a key phenomenon. Additionally, the main difference in the mean velocity in the near wake was the out-of-plane component, resulting from the rotation of the rotor, whereas the mean velocity is nearly the same in regions where rotation is not a critical phenomenon. They do, however, conclude that the results are encouraging for modelers who employ the actuator disk model for simulations of wind farms. Hence, there is a general agreement that the actuator disk is an adequate simplification in the far wake, and that there are certain discrepancies in the near wake, especially in the areas that are strongly affected by rotation when using a rotating model. It is important to note that the compared characteristics are usually mean flow characteristics. Despite a similarity of the mean flows, the instantaneous phenomena in the two wakes might still differ. Current literature examining the instantaneous flows and the fundamental structures constituting the flows is sparse. Camp and Cal (2019) compared a three-bladed rotating turbine model with an actuator disk using PIV. They applied snapshot Proper Orthogonal Decomposition (POD) and examined the invariants of the Reynolds stress anisotropy tensor, discovering discrepancies in the underlying spatial structures and the anisotropic character of the two wakes. While Camp and Cal (2019) have started to explore the issues of structural comparability of the wakes of actuator disks and rotating models, more research is needed to better understand the differences. By gaining more knowledge on how to improve the actuator disk model, it can become an accurate and simple tool for the industry.

The aim of this work is to examine how comparable a well matched actuator disk is to a rotating turbine instantaneously. The process of actuator disk selection is shown in detail, in order to determine how different disk designs and solidities affect the flow field. All actuator disks designed for the selection process are based on designs used in the literature. The results are therefore important to improve the knowledge of the flow physics in wakes of small-scale wind turbine models already used for research. For all the studied flow characteristics, the full streamwise 2D plane up to $x/D = 3.3$ is examined. This differs from the work of Aubrun et al. (2013) and Lignarolo et al. (2016b) who studied smaller fields of view, and Camp and Cal (2019) who conducted their POD analysis within limited sections of the downstream direction of their field of view. Further, the actuator disk whose wake most resembles the wake of the rotating model based on mean flow characteristics is chosen. The instantaneous phenomena and spatial structures in the wake of this actuator disk are examined and compared to the wake of the rotating model, in order to determine the potential similarities and differences of the underlying flow structures.

2. Experimental method

2.1. Facility

The experiments were conducted in the small closed-loop wind tunnel in Strømningslaben at NTNU; the test section measures 1 m × 0.5 m × 7 m (width × height × length). The present study was conducted 3 m downstream of the wind tunnel contraction. The inflow is uniform, with a maximum velocity of 35 m/s and a background turbulence intensity of 0.7%. It is the same facility as used by Skeide et al. (2020).

2.2. Test cases

Small-scale models were used in this study to examine the characteristics of models that are relevant for wind farm experiments, as mentioned in the introduction. The used rotating wind turbine models, hereafter referred to as the rotating models (RM), have two-bladed

plastic rotors connected to a sliding bearing. Magnets are placed at the bottom of the tower to facilitate the mounting. They have a rotor diameter of $D = 45$ mm and a hub height of 65 mm. The tip-speed-ratio ($TSR = \Omega D/2U_h$, where Ω is the angular velocity of the blade tip and U_h is the velocity at hub height) of the freely rotating models is approximately 4.8. This is slightly lower than, but still on the same order of magnitude as, utility scale turbines, which usually operate at $TSR \approx 6 - 8$. The maximum chord Reynolds number is on the order of $Re_c = U_r c/\nu = 2 \times 10^4$. Here, U_r is the local velocity experienced by the airfoil at a certain radius and c is the chord length. At low Reynolds numbers, thin airfoils have been shown to perform better than conventional airfoils (Sunada et al., 1997). Thus, the rotor blades are cambered plates with a thickness of 0.5 mm. The maximum chord length is $c = 8$ mm. The same models were used by Ebenhoch et al. (2017) and Segalini and Dahlberg (2020), and the RMs are thus representative of models used in lab-scale wind farm experiments.

The actuator disks were designed using SolidWorks and then 3D printed using an Ultimaker 2+ with PLA. Using computer-aided design (CAD) and 3D printing implies that the disk designs can easily be shared and reproduced; the CAD files of the geometries can be found in the Supplementary Material of this work. The disks were designed with a diameter of 45 mm to match the rotating turbine, and a thickness of 2.5 mm. Two different actuator disk designs were tested. The first has uniform circular holes and is intended to be similar in style to the mesh actuator disks used by Aubrun et al. (2013) and Lignarolo et al. (2016b). Hereafter, the disks with this design are referred to as Uniform Holes Disks (UHD). The second design has trapezoidal holes that increase in size as the radial coordinate increases, similar to the design employed by Camp and Cal (2016, 2019) and Bossuyt et al. (2017). The solidity of these disks decrease with radial coordinate, matching a characteristic of an actual wind turbine. Disks with this design are referred to as Nonuniform Holes Disks (NHD).

Three different solidities were tested: 35%, 40% and 60%. The disks are named UHD and NHD followed by the number describing their solidity, e.g., NHD35 for the 35% solidity disk with the NHD design. Due to limitations in the 3D printing process, producing 35% solidity with the UHD design proved problematic without letting the holes influence the perimeter of the disk. Hence, a 35% solidity disk with the UHD design is not included in the current work. A solid disk was also made for reference. All the disks can be seen in Fig. 1.

The actuator disks were designed with a small hole in the center in order to connect them to towers. This design resulted in a large solidity in the center of the disks, which can represent the nacelle of a wind turbine (Neunaber, 2018). The tower was designed to match the RM's tower, and a magnet was placed at the bottom of it.

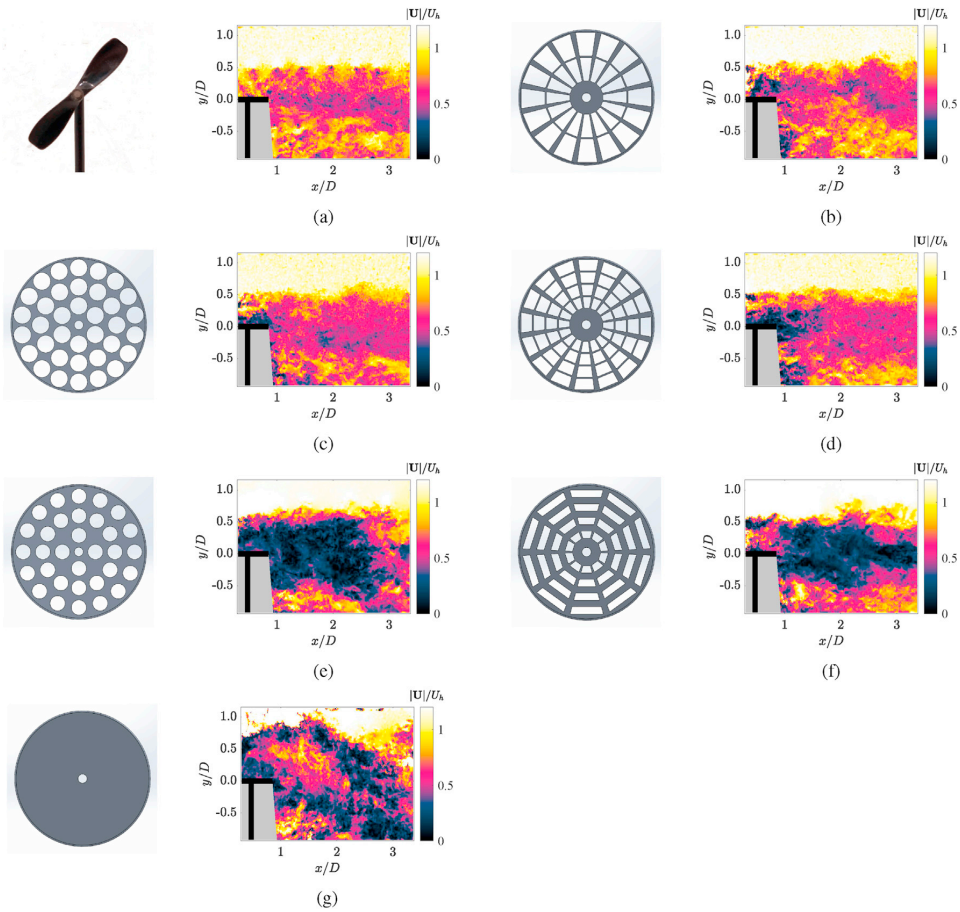

Fig. 1. All actuator disk designs and a picture of the RM, next to an image of the instantaneous total velocity field behind the respective disk and the RM. (a) RM, (b) NHD35, (c) UHD40, (d) NHD40, (e) UHD60, (f) NHD60 and (g) the solid disk.

2.3. Force measurements

Underneath the wind tunnel is a six-component AMTI BP40060HF 1000 force plate, able to measure the force and moment components along the x-, y- and z-axes. Here, x is the downstream, longitudinal direction, y is upwards, and z completes a right-hand system.

A test rig was constructed to measure the forces, consisting of a 0.5 m long magnetic steel bar that stretched along the width of the wind tunnel, on top of an aluminium cylinder that passed through a small hole in the floor of the tunnel. The cylinder was then attached to the force plate underneath the tunnel. The steel bar was lifted about 1 cm above the floor of the wind tunnel, to avoid any contact with the floor that could affect the force measurements, and to place the turbine in a uniform stream uninfluenced by the boundary layer developing on the wind tunnel floor. A sketch of the setup, as well as the defined axes and origin, is shown in Fig. 2.

Three models were placed on the test rig while conducting the drag measurements. This was done to ensure that the drag would be within the load cell range and the small changes in solidity would be measurable. Using three models also averages any small differences that might be present between the models. One model was placed in the center of the steel bar, at $z = 0$, and the other two were placed at a distance of $5D$ from it, i.e., at $z = \pm 5D$. The measured drag coefficient,

$$C_D = \frac{F_D}{\frac{1}{2}\rho U_h^2 A}, \tag{1}$$

where F_D is $\frac{1}{3}$ of the measured drag (because three models were used), and $A = \pi D^2/4$ is the reference area, for the RM in the present study is within $\pm 1\%$ of the C_D reported by Ebenhoch et al. (2017) who used the same turbines. This confirms that the setup is appropriate for this measurement.

The drag force in the x-direction was then measured for five different incoming wind velocities, corresponding to five different incoming Reynolds numbers $Re_D = U_h D/\nu$, where ν is the kinematic viscosity of air based on the measured temperature in the wind tunnel. Drag measurements were also conducted having only the test rig and three towers inside the wind tunnel. Each measurement lasted 60 s with a sampling rate of 1000 Hz. Zero measurements were conducted before and after every measurement, to account for potential drift of the force plate. Measurement noise related to the transducer and the electrical equipment gave rise to some uncertainty. Nevertheless, the signal-to-noise ratio improved with the magnitude of the drag force. The lowest Reynolds number shown in the results was selected based on where the signal-to-noise ratio of the system became acceptable. For the Reynolds numbers presented, the uncertainty in the force measurements ranged

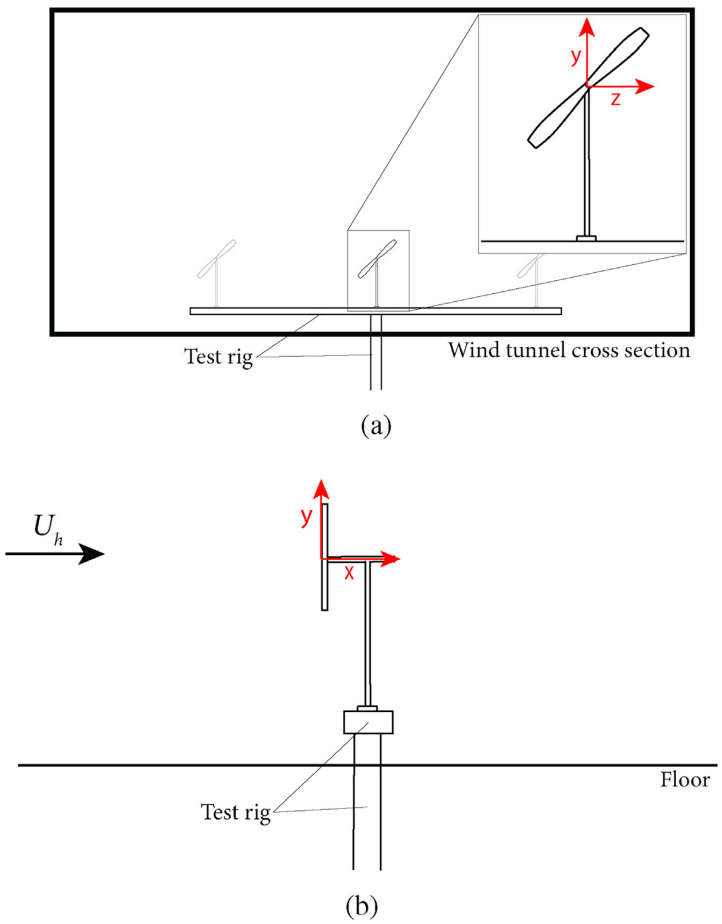

Fig. 2. Sketch of the RMs on the test rig, with the defined axes, (a) from the point of view of the incoming flow and (b) from the side. The grey models were not installed during the PIV acquisition. The sketch is illustrative and not to scale.

from 0.9% to 4%.

2.4. Particle image velocimetry

For the PIV measurements, two LaVision Imager LX 16 megapixel cameras were used, combined with Sigma 180 mm 1:3.5D APO DG Macro lenses. The cameras were mounted outside of the wind tunnel, next to an acrylic window. The first and the second camera had their field of view just upstream and downstream of the turbine rotor, respectively, meaning that the two did not overlap. The first field of view had a range of $-3.01 \leq x/D \leq 0.01$ and $-1.12 \leq y/D \leq 0.92$, while the second had a range of $0.31 \leq x/D \leq 3.33$ and $-0.91 \leq y/D \leq 1.13$. Thus, the near-wake was captured by the second field of view, while the first field of view could be used to quantify the incoming velocity at hub height and to study the characteristics of the incoming flow. In some of the presented results, the data near the upper and lower edge of the field of view have been cropped due to noise arising from particles entering and exiting the domain.

A Litron Nano L200-15 laser, which is a Nd-YAG dual-pulse laser with a measured power of 208 mJ per pulse, was used to illuminate the particles. The laser sheet entered the wind tunnel through an acrylic window in the roof. The particles were seeded using a Martin Magnum 2500 Hz smoke machine and the Martin Rush & Thrill Haze Fluid, producing particles that are approximately 1 μm in diameter. A LaVision PTU X programmable timing unit was used to trigger and synchronize the laser and the cameras. In each measurement, 1000 frames were acquired by each camera. Further acquisition details are provided in Table 1.

The recordings were acquired and processed using LaVision Davis 8.4. Background noise was subtracted from the images by subtracting the minimum value of every pixel over the entire data set, and then over a filter length of 29 image pairs to remove local variations in laser light intensity. Then, the local mean background intensity was filtered out by subtracting the sliding minimum over 20 pixels. The sliding average was calculated over five pixels using a Gaussian profile. Image correction was applied to correct for orthogonality. The processing was then performed with a window size of 96 × 96 pixels and an overlap of 50% for the first pass, while the final window size was 32 × 32 pixels with an overlap of 50%. The resulting uncropped vector field consisted of 307 × 207 vectors.

The 1000 vector fields for each case are independent, and the second-order statistics are converged to within ±8.7% based on the 95% confidence interval. In order to substantially improve this, an order of magnitude increase in the number of samples is required (Cardesa et al., 2012), which is untenable here because of the number of test cases. The uncertainty in the velocity measurement based on the PIV correlation statistics is 2.7% in the high shear, tip-vortex shedding region of the flow where there is high out-of-plane particle movement. This was estimated directly in DaVis using established techniques (Wieneke, 2015; Neal et al., 2015; Sciacchitano et al., 2015). In the rest of the field, the velocity uncertainty is nearer 1.5%.

2.5. Notation

The following notation is used when discussing the results. Each instantaneous velocity, corresponding to one location in one PIV frame, is denoted as $u = u + u'$ and $v = v + v'$ for the velocity in the $x-$ and $y-$directions, respectively, where u' and v' corresponds to the fluctuating parts of the velocity, and u and v are the mean velocities calculated by taking the mean over all 1000 statistically independent PIV measurements. The mean total velocity is $\mathbf{U} = [u, v]$. The measurements are conducted in a 2D plane, and hence the out-of-plane velocity component w is not incorporated into the present analysis. Each characteristic calculated by taking the average over all the PIV measurements is denoted with an overbar.

Table 1
PIV parameters used in data acquisition and processing.

Parameter	Value	Unit
Interframe time	50	μs
Acquisition rate	0.86	Hz
Number of samples	1000	
Field of view ($x \times y$)	3.02 × 2.04	D
Final window size	32 × 32	pixels
Window overlap	50	%
Vectors ($x \times y$)	307 × 207	

3. Drag measurements

Since actuator disks are usually designed to match the drag of a rotating turbine, the first step was to conduct drag measurements. For each model and at each incoming Reynolds number, the average drag force over the 60 s measurement was calculated, and the drag resulting from the test rig and the towers was subtracted. As three models were used during the drag measurements, the drag force was then divided by three, arriving at the drag acting on only one disk or one set of rotating blades. The drag coefficient as a function of Reynolds number is plotted in Fig. 3 for all the models.

Lignarolo et al. (2016b) showed drag coefficients as a function of actuator disk solidity based on the results presented in six different papers, and concluded that the drag coefficient decreases approximately linearly with decreasing solidity. That is also the case for the current measurements. As expected, the solid disk produces a much higher drag coefficient than the RM. The drag coefficient of the solid disk at $Re_D = 3 \times 10^4$ is omitted from the figure, as it deviates from the others by more than 42 standard deviations, and is thus regarded as an outlier.

The drag coefficients seem to concentrate around some mean value, suggesting that the non-dimensional drag is Reynolds number independent over the presented Re range. The average drag coefficient over the different Reynolds numbers was calculated, along with the standard deviation, and is presented in Table 2 for the RM and the actuator disks with 35% and 40% solidity. The NHD35 is the best match compared to the drag coefficient of the RM, with a deviation of 1.8%.

4. Reynolds number dependence of the velocity field

For the RM and NHD35, PIV measurements were conducted at five different incoming Reynolds numbers, relating to five different incoming flow velocities at hub height, U_h. This was done to check whether the normalized velocity in the wake would vary as a function of the incoming Reynolds number, since the non-dimensional drag was Reynolds number independent in this regime. The mean velocity field was calculated and then normalized by U_h. The streamwise velocity component is the dominant component of the total velocity. Hence, Fig. 4 depicts the streamwise velocity component at five downstream locations for all five incoming Reynolds numbers for the RM and the NHD35. The first profile is from shortly behind the end of the model tower, and the last profile is located close to the end of the field of view.

For the actuator disk, the normalized velocity profiles overlap at all the downstream locations. On average, the standard deviation between the measurements as a percentage of the mean value is 2.4% in the entire field of view. Thus, the actuator disks are independent of Reynolds number within the investigated range.

For the RM, the lines illustrating the normalized streamwise velocity generally follow the same pattern and largely overlap as close to the disk as 1D downstream. By 3D downstream, the velocity profiles are in very good agreement. However, it can be seen that the two lowest Reynolds numbers produce a slightly different profile at 1D, e.g., behind the nacelle at $y/D = 0$, implying that the RM's wake is only Reynolds number independent above some threshold Reynolds number. Studying the three highest Reynolds numbers, starting at $Re_D = 3 \times 10^4$, an average standard deviation of 3.3% of the mean value is found.

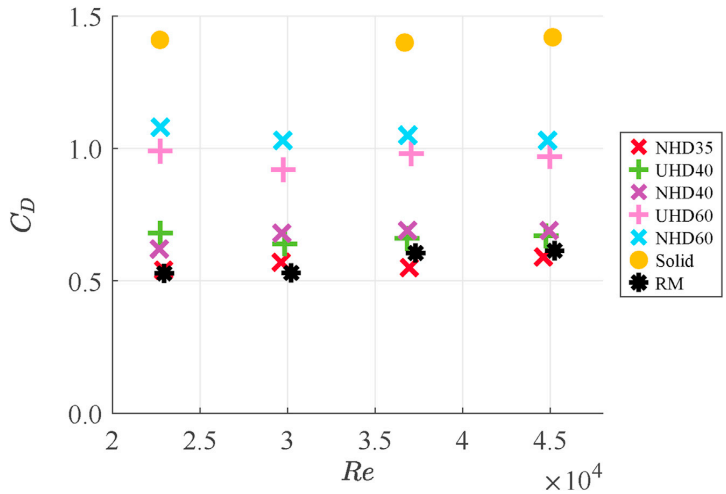

Fig. 3. The drag coefficient as a function of incoming Reynolds number for all turbine models.

Table 2
Average C_D for the RM and the disks with 35% and 40% solidity across measurements taken at different Reynolds numbers, and the associated standard deviation.

Disk type	Average C_D	C_D standard deviation
RM	0.57	0.08
NHD35	0.56	0.05
UHD40	0.66	0.05
NHD40	0.67	0.06

Based on the mean velocity field and drag results, the two lowest Reynolds number cases, $Re_D = 1.5 \times 10^4$ and $Re_D = 2.3 \times 10^4$, illustrate a dependence on the Reynolds number. To avoid Reynolds number effects in the following analysis, the rest of the PIV measurements were performed at the lowest Reynolds number within the Reynolds independent regime, $Re_D = 3 \times 10^4$, in order to limit other detrimental factors, e.g., the models auto-yawing inadvertently during a test; any test where this was observed was repeated such that none of the results presented herein represent yawed turbines.

5. Mean velocity fields

The velocity in the wake is the first characteristic used to compare the RM with the actuator disks. The time averaged total velocity $|\mathbf{U}|$ was normalized by the incoming velocity U_h, and is depicted in Fig. 5 for the RM and each actuator disk. The vectors indicate the magnitude and the direction. A mask has been applied over the model and to the area affected by shadows and laser reflection near the tower. The total velocity up to 1D upstream of the models is also included in Fig. 5.

The total velocity upstream of the actuator disks indicates that the incoming flow slows directly in front of the disks, and that the slowdown increases in magnitude and covers a larger area as the solidity of the disks increase. The slowdown in front of the blades of the RM has a smaller magnitude than what can be seen for the NHD35, showing that the RM imposes less of a blockage to the incoming flow. Although subtle, this result has implications for blockage estimates made for wind farms using either free RMs or actuator disks, which have been demonstrated to have

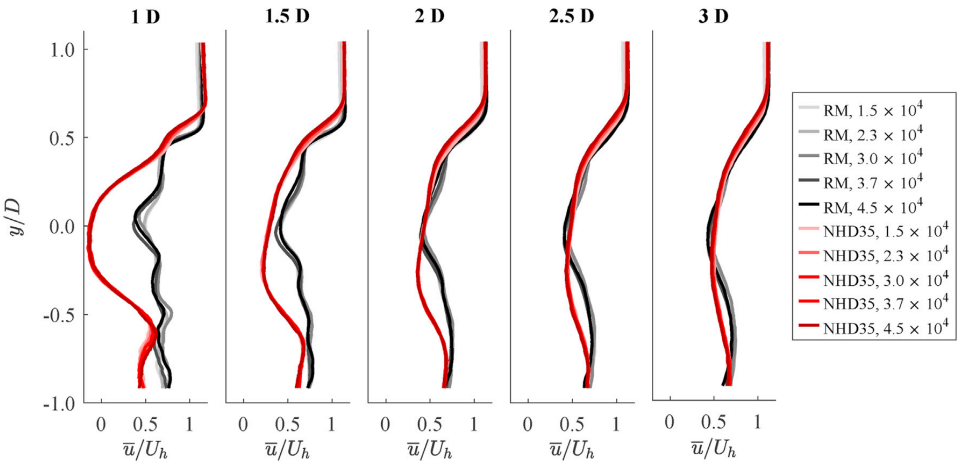

Fig. 4. Normalized u velocity downstream of the RM and the NHD35 actuator disk for different incoming Reynolds numbers.

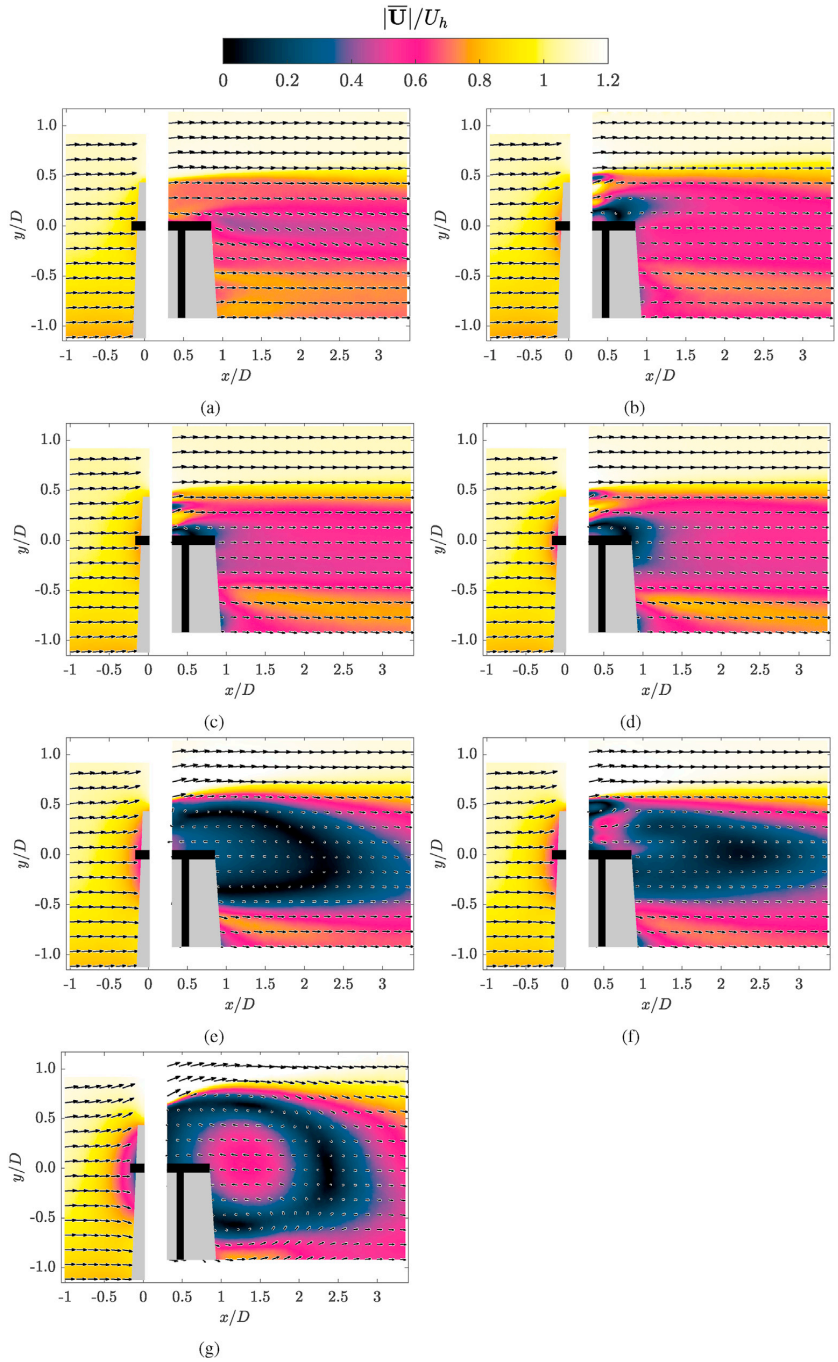

Fig. 5. Normalized total velocity fields for (a) the RM, (b) NHD35, (c) UHD40, (d) NHD40, (e) UHD60, (f) NHD60 and (g) the solid disk.

different blockage effects here.

The solid disk produces a significant recirculation area as a result of its large blockage. The UHD60 also induces a large area of reversed flow, and neither are thus comparable to the RM. The remaining actuator disks have a small recirculation area directly behind the disk, that is only present less than 1D downstream, and thus only affects the comparability of the disks and the RM in the immediate wake.

It is evident that the solid disk and the disks with 60% solidity have

considerable areas of deviation from the RM, which agrees with the drag measurements. Furthermore, the NHD40 deviates more from the RM than the UHD40 and NHD35. UHD40 and NHD35 both show good agreement with the RM, with the main difference being less than 1*D* downstream. The two have similar magnitude of deviation after 1*D*, however, the UHD40 is slightly closer to the RM when averaging the absolute value of the deviations.

Fig. 6 shows the normalized *u* velocity, being the dominant velocity component, at five different downstream locations as well as one upstream location. The tip vortices present at the upper edge of the RM's wake (distinctly visible in Fig. 1a and comparable to those found by Hong et al. (2014)) induce a steep velocity gradient seen at 1*D* downstream. The gradient then flattens as one moves farther downstream and the tip vortices lose strength. The actuator disks show a smoother transition between the freestream and the wake at 1*D* downstream. The velocity variations in the wake of the actuator disks homogenize quickly compared to the RM's wake. This is because the actuator disks transfer kinetic energy in the flow into turbulence which quite quickly decays (Batchelor and Townsend, 1947, 1948a,b). The actuator disks with low solidity have a high velocity gradient region in the same vertical position as the RM, however, this region of high velocity gradient occurs farther from the centre of the disk as the solidity of the disk increases. Overall, Fig. 6 indicates that the magnitude of *u* behind the RM is comparable to the magnitude of *u* generated by NHD35, NHD40 and UHD40 from 1.5*D* downstream.

6. Vorticity

In order to understand the organization of vortical structures in the wake of the RM and the actuator disks, the vorticity is examined. The time averaged out-of-plane vorticity ω_z was normalized using the incoming flow velocity U_h and the disk diameter D. Fig. 7 shows the normalized vorticity for each actuator disk and the RM. The solid disk and the disks with 60% solidity create two distinct areas of high magnitude vorticity, covering large parts of the wake, and thus differ from the lower solidity disks which seem to mainly produce vorticity at the upper and lower edges of the wake. This vorticity seen at the edges of the wake may be caused by vortices created at the disk edges or as a result of the interaction between the wake and the free-stream. Additional vorticity is present directly behind the actuator disks, which is likely caused by the turbulent flow through the holes in the disks, and the interaction of these flows behind the disks (Ertunç et al., 2010; Mazellier and Vassilicos, 2010).

The RM also produces high levels of vorticity along the upper and lower edges of the wake, as a result of tip vortices from the rotor blades. The upper line of vorticity is stronger and preserves its strength for a longer distance downstream than is the case with the low solidity actuator disks. However, towards the end of the field of view, this strong vortex sheet breaks down and the vorticity diffuses. There is also vorticity present in the center of the wake of the RM, possibly representing the root vortex from the hub (Lignarolo et al., 2016b).

A quantitative comparison was made to determine which of the disk

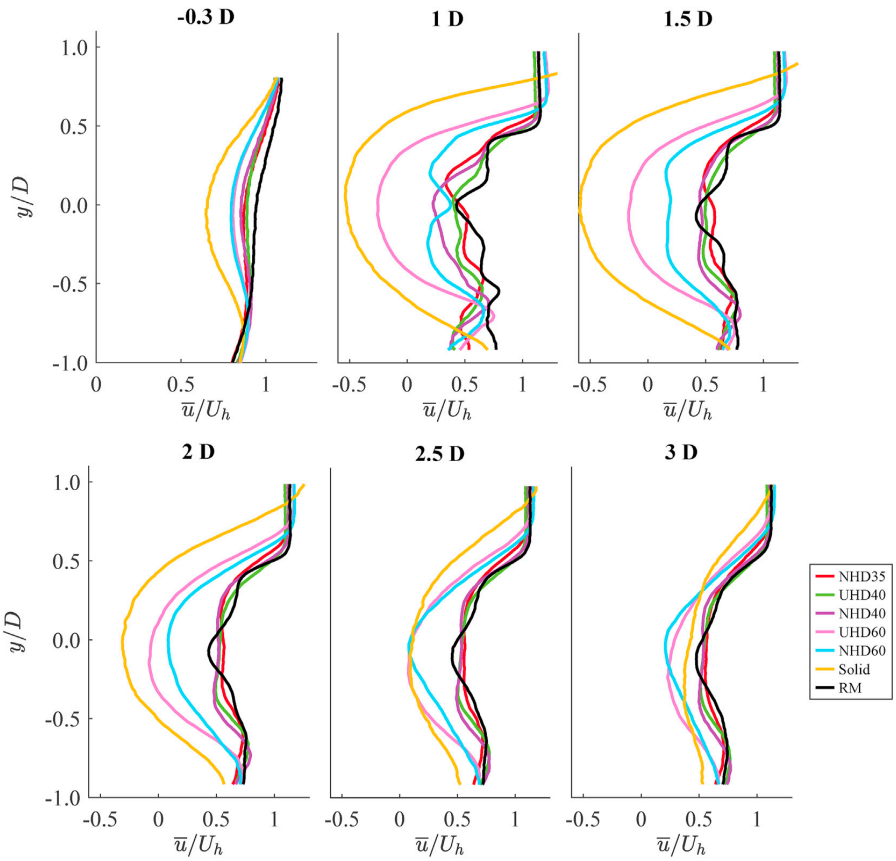

Fig. 6. Normalized *u* velocity at one upstream and five downstream locations for the RM and each actuator disk.

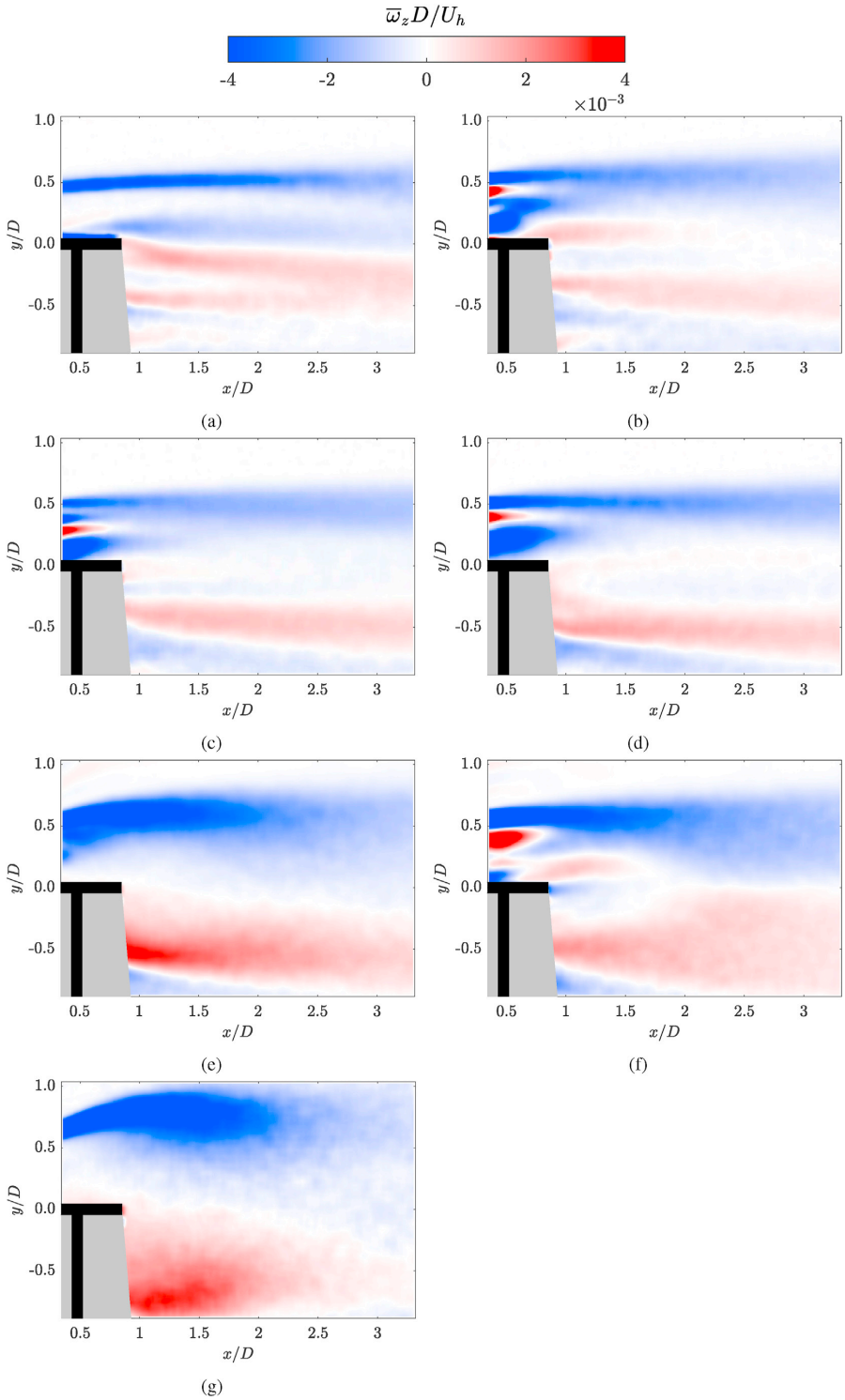

Fig. 7. Normalized vorticity fields for (a) the RM, (b) NHD35, (c) UHD40, (d) NHD40, (e) UHD60, (f) NHD60 and (g) the solid disk.

wakes has the vorticity field that best resembles the vorticity downstream of the RM. Close to the disks, the exact position of the holes is important for the vorticity field. To avoid these effects in the comparison, only the flow field downstream of 1.5D was evaluated. Two metrics have been used to evaluate which of the disks best resembles the RM. First, the magnitude of the average difference between the vorticity vectors of the RM and the disks have been calculated. The 40% and 35% solidity disks resemble the RM the most, with the NHD35 showing the smallest difference. Second, the percentage of vorticity vectors showing the same sign as the RM was counted. The number of vectors with the same sign is similar for most of the disks, with values around 80%. The results for both metrics are shown in Table 3. Using these metrics, the NHD35 is the closest match to the RM downstream of 1.5D.

Going forth, the analysis will be focused on only one actuator disk. Since NHD35 is the closest match in terms of the drag and the mean vorticity field, the remaining analysis will focus on this disk. For completeness, the results for the other disks are provided in the Supplementary Material to this work. The chosen disk is compared to the RM for several mean metrics, in a similar manner to previous actuator disk studies. However, in this case, in order to gain knowledge about the underlying mechanisms of the flow, more than just mean quantities are studied.

The mean vorticity field is a result of instantaneous swirl, and thus, the instantaneous swirl can provide information about the flow structures that cause vorticity in the flow. Swirling strength is defined as the second invariant of the velocity gradient tensor as described by Jeong and Hussain (1995). Fig. 8 shows an image of the instantaneous swirling strength, signed by vorticity, for the RM and the NHD35. These images are representative of the 1000 PIV measurements that were taken. The main difference between the two is the strong, distinct swirl seen at the upper edge of the wake for the RM, caused by tip vortices from the rotor blades. The actuator disk also has some swirl in the upper part of the wake, however it has a significantly lower strength than the distinct vortices from the RM, and it resembles the swirl at the lower edge of the wake and close to the wind tunnel floor. This swirl may be formed by the roll-up of the shear layer produced by the presence of the disk. The actuator disk also has high intensity swirl directly behind the disk, not seen after the RM's blades. As previously mentioned, this swirl is believed to be caused by the turbulent flow passing through the holes in the disk and the interaction of the jets behind the disk.

The important finding here is that even though averaging of the measurements resulted in similar sheets of vorticity at the upper edge of the wake, with an average local difference of less than 5% in the last half of the field of view, the instantaneous vortex structures differ. Many previous studies have used porous style disks which approximately match the drag and mean fields (Lignarolo et al., 2016b; Camp and Cal, 2016; Bossuyt et al., 2017). However, as indicated here when studying the instantaneous fields, the phenomenology in the flows might still be different.

7. Reynolds stresses

Another mean flow characteristic often examined when comparing actuator disks and RMs is the normal and shear Reynolds stresses. The normal Reynolds stresses are investigated here through the time averaged turbulence intensity, expressed as the normalized root of the mean 2D turbulent kinetic energy

$$\frac{\sqrt{k_{2D}}}{U_h} = \frac{\sqrt{\frac{1}{2}(\overline{u'u'} + \overline{v'v'})}}{U_h}, \tag{2}$$

where $\overline{u'u'}$ and $\overline{v'v'}$ are the normal Reynolds stresses in the streamwise and wall-normal directions, respectively. The time averaged turbulence intensity in the wake of the RM and the NHD35 can be seen in Fig. 9.

The RM shows high turbulence intensity at the upper edge of the wake, stemming from the tip vortices. Towards the end of the field of view, the tip vortices start to break down, and the turbulence diffuses. The turbulence intensity at the upper edge of the wake behind the actuator disk indicates that vortices emerging at the disk edge are present in close vicinity of the disk, for $x/D < 1$. However, this turbulent structure quickly diffuses. The actuator disk shows a high concentration of turbulence intensity directly behind the disk, which then slowly diffuses throughout the wake. This highly turbulent region is likely caused by the turbulent mixing of the jets and the small recirculation zone as observed in section 5, akin to grid turbulence (Ertunç et al., 2010). The most evident difference between the two wakes is in this region shortly behind the disk, less than 1D downstream. Downstream of 2D, the average difference between the two fields is 12%.

The mean in-plane Reynolds shear stress, $\overline{u'v'}$, normalized with the incoming velocity squared, is shown in Fig. 10a for the RM and Fig. 10b for NHD35. The shear stress $\overline{u'v'}$ physically represents the vertical flux of momentum, with negative values indicating downward flux and positive values indicating upward flux. Hence, it can be seen that for both models, the upper part of the wake is dominated by negative $\overline{u'v'}$ and the lower part is dominated by positive $\overline{u'v'}$.

Both the RM and NHD35 produce more intense shear stress in the shear layer of the wake, caused by flow entrainment and mixing. For the actuator disk, an increased intensity of shear stress is observed directly downstream of the disk, likely caused by the same phenomena that causes increased normal stresses in this area, i.e., the turbulent mixing of the flow passing through the holes in the disk. The largest difference between the two flow fields is found in this region, for $x/D < 1$. Fig. 11 illustrates the shear stress along three downstream cross-sections. As can be seen, the differences between the shear stress produced by the two models diminishes as one moves farther downstream, and the shear stress is largely of the same order of magnitude. Thus, the mean characteristic of Reynolds stresses is comparable between the static disk and the RM.

8. Proper orthogonal decomposition

As the swirl indicated that the instantaneous phenomena in the wakes differ between the RM and NHD35, the spatial modes that make up the wake were investigated to gain an understanding of the underlying spatial structures in the flows. In order to examine this, POD was applied. POD was first developed for fluid mechanics by Lumley (1967). Sirovich (1987) then developed the method of snapshot POD, where each instantaneous PIV measurement is considered to be a snapshot of the flow. The analysis conducted in this study followed the steps described by Meyer et al. (2007).

Snapshot POD is used to find the spatial modes of the flow. The mean velocity field is considered to be the zeroth mode. The analysis then focuses on the fluctuating parts of the velocity components. The method states that each snapshot can be expanded in a series of POD modes. Thus, if $\mathbf{u}^{*n}$ is a vector containing all the fluctuating u and v velocities in snapshot n, $[u'^{n_1} \ldots u'^{n_M} v'^{n_1} \ldots v'^{n_M}]^T$, where M is the number of positions in the snapshot,

$$\mathbf{u}^{*n} = \sum_{i=1}^{N} a_i^n \boldsymbol{\varphi}^i. \tag{3}$$

Table 3
Comparison of vorticity downstream of $x = 1.5D$.

Disk	$\frac{\overline{\lvert\overline{\omega_{\text{Disk}}} - \overline{\omega_{\text{RM}}}\rvert}}{\max(\overline{\omega_{\text{RM}}})}$	$\frac{\overline{\omega_{\text{Disk}}}}{\overline{\omega_{\text{RM}}}} \geq 0$ [%]
NHD35	0.0519	81.9
NHD40	0.0616	72.0
UHD40	0.0556	81.2
NHD60	0.0745	81.5
UHD60	0.0920	82.4
Solid	0.1205	79.8

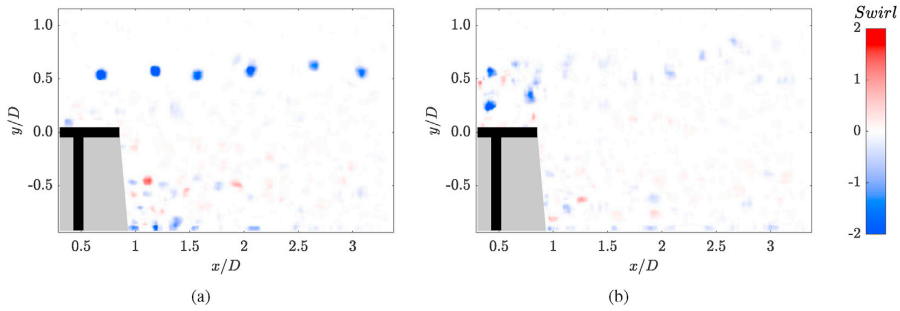

Fig. 8. Representative instantaneous swirling strength fields signed by vorticity for (a) the RM and (b) NHD35.

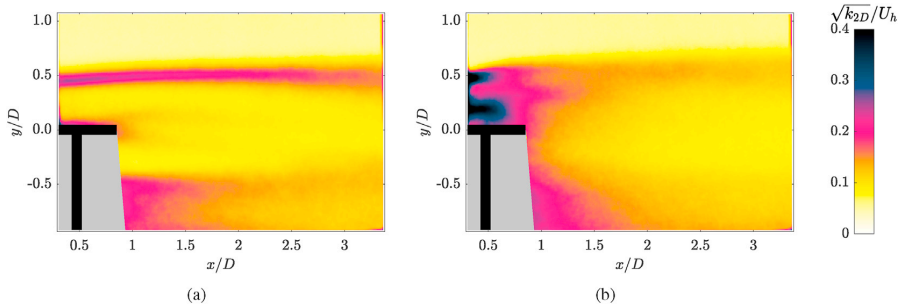

Fig. 9. Turbulence intensity fields for (a) the RM and (b) NHD35.

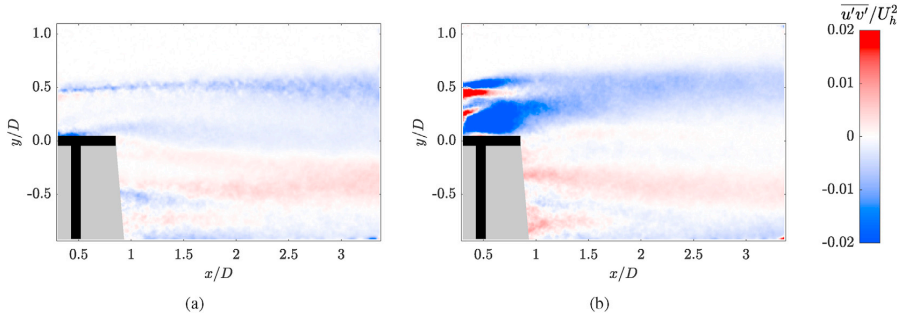

Fig. 10. Normalized Reynolds shear stress fields for (a) the RM and (b) NHD35.

Here, $\boldsymbol{\varphi}^i$ are the POD modes, and a_i^n are the POD coefficients related to snapshot n, determined by projecting the fluctuating part of the velocity field onto the POD modes. The analysis was performed on $N = 1000$ snapshots for each model.

The modes are ordered by their energy content, $[\lambda_1 \ldots \lambda_N]$, with lower numbered modes having higher energy content than higher numbered modes. Fig. 12 displays the cumulative energy of the modes for the RM and all the actuator disks. The NHD35 is the actuator disk which most closely resembles the RM in terms of the magnitude of energy contained in each mode. Additionally, both the RM and the NHD35 seem to have two particularly energetic modes.

Since 1000 vector fields have been used to construct the modes, 1000 modes would be required to capture all the energy in the velocity fluctuations. The number of modes required to capture a certain fraction of the energy can, however, provide some indication on the number of modes required to make a relevant approximation of the fluctuating velocity (van der Kindere and Ganapathisubramani, 2018). It is worth noting at this point that all the actuator disks and the RM require a relatively large number of modes to capture 50% of the energy in the flow, the RM requiring 129 modes and the NHD35 requiring 140 modes. This suggest that even though the few most energetic modes might provide information about the most energetic structures in each flow, the flows are not constructed of a few large, energetic structures. Rather, they seem to be complex flows with large amounts of local fluctuations, requiring many modes to be described.

When high-energy modes are present, these usually represent periodic, large-scale flow structures. However, the amount of energy contained in the modes does not imply anything about the shapes of the modes. Figs. 13 and 14 show the first mode of the fluctuating streamwise (φ_u^1) and vertical (φ_v^1) velocity components, respectively, for the RM and the NHD35. When examining the modes, the absolute values are insignificant, as each mode is coupled with a relative POD coefficient when

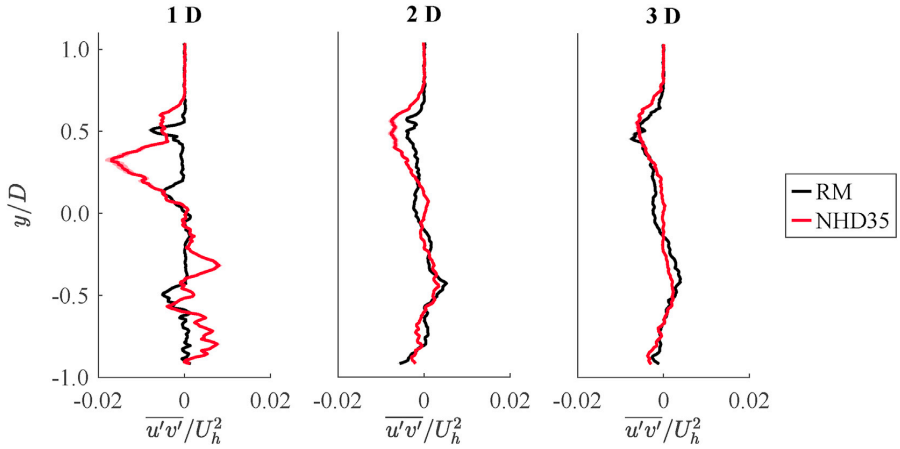

Fig. 11. Normalized Reynolds shear stress $\overline{u'v'}$ at three locations downstream of the RM and the NHD35.

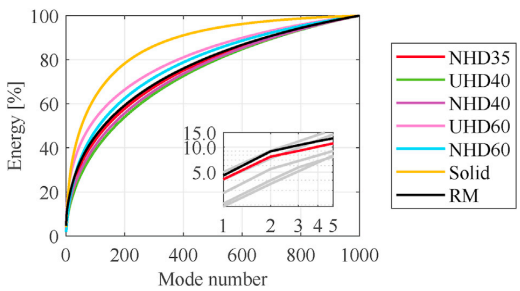

Fig. 12. Cumulative energy of the modes for all actuator disks and the RM. The inset is zoomed in on the five most energetic modes on log-log axes, with RM and NHD35 highlighted.

used to reconstruct the fluctuating velocities in a snapshot. The important factor is the relative values, demonstrating the length scale and location of the velocity fluctuations that contain a certain fraction of the total energy.

The first mode of the RM shows high intensity turbulent kinetic energy at the upper and lower edges of the wake, which seem to represent the kinetic energy in the tip vortices from the blades. These energetic structures start right behind the rotor blades and are still visible at the end of the field of view, but do, however, seem to decrease in intensity farther downstream. As previously mentioned, Camp and Cal (2019) studied the POD modes of actuator disks and RMs in the *xy*-plane. They found a prominent feature near the top tip of the wake in φ_u^1. However, the tip vortices found behind the RM in Fig. 13 are more distinct. Additionally, tip vortices can be observed in φ_v^1 in this case.

The first mode in the wake of NHD35 also demonstrates repeating structures, suggesting a periodic shedding structure is also present for this disk, but with very different dynamics to that in the wake of the RM. There is high intensity turbulent kinetic energy directly behind the disk, suggesting high velocity fluctuations at this location. These fluctuations might be connected to the turbulent mixing of the flow jets passing through the holes in the disk.

Comparing the modes of the RM and the NHD35, it is evident that the most energetic structures in the two flows are fundamentally different. The energetic structures in the modes of the RM are concentrated around the edges of the wake, whereas for NHD35, the energetic structures are to a larger extent present in the center of the wake. A difference can also be seen in terms of the length scale of the structures. The RM indicates small

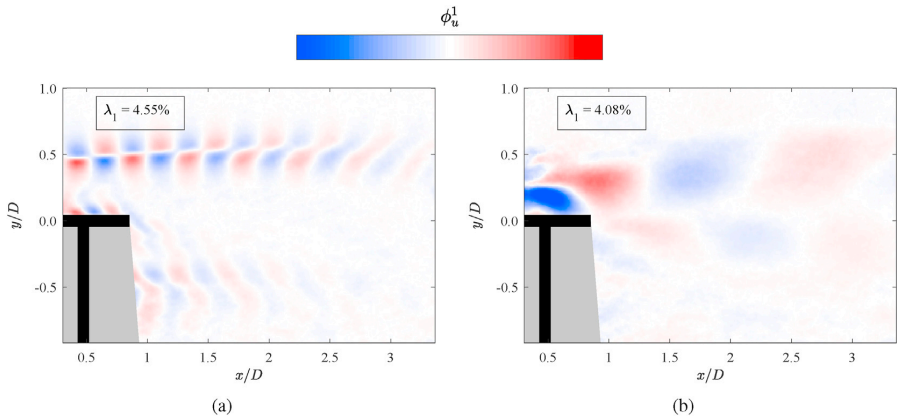

Fig. 13. φ_u^1 for (a) the RM and (b) NHD35. Only the relative values are of importance. λ_1 expresses the percentage of the total fluctuating energy found in the first velocity mode.

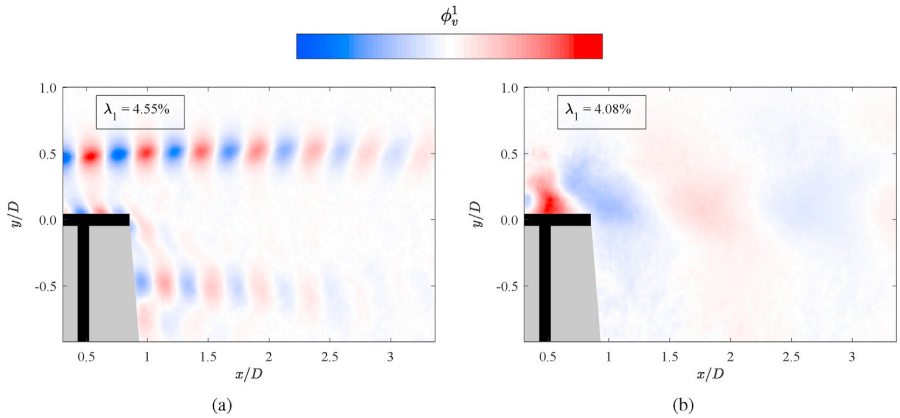

Fig. 14. φ_v^1 for (a) the RM and (b) NHD35. Only the relative values are of importance. λ_1 expresses the percentage of the total fluctuating energy found in the first velocity mode.

energetic structures, with the velocity fluctuations quickly changing direction. The actuator disk illustrates significantly larger, and thus fewer, structures. As previously seen in terms of the instantaneous swirling strength, the tip vortices stemming from the RM are evident, and such strong tip vortices do not appear in the case of the actuator disk. None of the actuator disks showed similar behavior to the RM when studying their modes.

9. Conclusion

The near wake of a lab-scale rotating wind turbine model and multiple actuator disks of the same dimensions were studied experimentally in a wind tunnel with PIV. Actuator disks of two different designs and multiple different solidities were used in order to represent the different designs that have been employed by the existing literature. Both designs, as well as the RM, are representative of lab-scale wind turbine models found in the literature. The process of actuator disk selection, which is often implicit in actuator disk research, is explicitly shown by presenting the results from drag measurements as well as the mean velocity and vorticity fields in the wake.

The normalized total velocity in the wake of the RM and each actuator disk was compared, showing that the high solidity disks had too large blockage, which led to a significant velocity deficit in the wake. The velocity field that developed behind the low solidity disks agreed well with the wake of the RM. Nonetheless, all actuator disks showed a recirculation region that was limited to $x/D < 1$ for the lower solidity disks.

The out-of-plane vorticity in the wakes was subsequently compared. The RM showed increased intensity of vorticity along the upper edge of the wake, induced by tip vortices. The actuator disks also showed increased levels of vorticity along the edges of the wake. The lower solidity disks showed high intensity vorticity directly behind the disks, induced by turbulent mixing of the flow jets passing through the holes of the disks.

The NHD35 actuator disk was the closest match to the RM in terms of drag coefficient and mean wake vorticity, and was thus studied in further detail. In previous studies, the comparison has been limited to mean characteristics. Since the mean vorticity field is a result of instantaneous swirl, the instantaneous swirling strength signed by vorticity was studied in the present work. It illustrated that instantaneous tip vortices were present behind the RM, but not behind the NHD35. Additionally, high intensity swirl was seen directly behind the actuator disk, which again was believed to be related to the mixing of the flow jets through the disk holes.

The normal and shear Reynolds stresses of the NHD35 and the RM were comparable. The difference between the two wakes was limited to the area $x/D < 1$.

POD analysis was conducted to analyze the underlying instantaneous phenomena of the two flows. It showed how the most energetic mode for the RM represented the upper and lower tip vortices, which were not present for the actuator disk. The energetic velocity fluctuations differed both in terms of length scale and location. This implies that the main structures constituting the two flows are different.

Despite having fairly good agreement between the RM and the actuator disk across many mean parameters, including drag, velocity, vorticity and Reynolds shear stress, the modal structure of the flows were still different. The underlying, instantaneous flow phenomena in the near wake of the actuator disk are thus not representative of a RM.

Actuator disks are clearly good for capturing mean flow properties, but as this study has shown, instantaneous phenomena in the wake are not always well captured. Moreover, the upstream blockage effect of the actuator disks and RMs differed. Therefore, as actuator disks will continue to be used, it is important to understand all aspects of their flow behavior. This will contribute to a better understanding in studies in which they are employed, and may also help in the development of different disk designs which better capture higher order and instantaneous flow features.

CRediT authorship contribution statement

Sanne de Jong Helvig: Methodology, Software, Validation, Formal analysis, Investigation, Writing - original draft, Visualization. **Magnus K. Vinnes:** Conceptualization, Methodology, Software, Validation, Investigation, Writing - review & editing. **Antonio Segalini:** Resources, Writing - review & editing. **Nicholas A. Worth:** Conceptualization, Resources, Writing - review & editing, Supervision, Project administration. **R. Jason Hearst:** Conceptualization, Resources, Writing - review & editing, Supervision, Project administration.

Declaration of competing interest

The authors declare that they have no known competing financial interests or personal relationships that could have appeared to influence the work reported in this paper.

Acknowledgements

The authors would like to acknowledge the support of M. Asadi who

participated in and supported the PIV measurement campaign.

Appendix A. Supplementary data

Supplementary data to this article can be found online at https://doi.org/10.1016/j.jweia.2020.104485.

References

Aubrun, S., Bastankhah, M., Cal, R., Conan, B., Hearst, R., Hoek, D., Hölling, M., Huang, M., Hur, C., Karlsen, B., Neunaber, I., Obligado, M., Peinke, J., Percin, M., Saetran, L., Schito, P., Schliffke, B., Sims-Williams, D., Uzol, O., Vinnes, M., Zasso, A., 2019. Round-robin tests of porous disc models. J. Phys. Conf. 1256, 012004 https://doi.org/10.1088/1742-6596/1256/1/012004.

Aubrun, S., Loyer, S., Hancock, P., Hayden, P., 2013. Wind turbine wake properties: comparison between a non-rotating simplified wind turbine model and a rotating model. J. Wind Eng. Ind. Aerod. 120, 1–8. https://doi.org/10.1016/j.jweia.2013.06.007.

Barthelmie, R.J., Churchfield, M.J., Moriarty, P.J., Lundquist, J.K., Oxley, G.S., Hahn, S., Pryor, S.C., 2015. The role of atmospheric stability/turbulence on wakes at the Egmond aan Zee offshore wind farm. J. Phys. Conf. 625 https://doi.org/10.1088/1742-6596/625/1/012002.

Barthelmie, R.J., Jensen, L.E., 2010. Evaluation of wind farm efficiency and wind turbine wakes at the Nysted offshore wind farm. Wind Energy 13. https://doi.org/10.1002/we.408.

Batchelor, G., Townsend, A., 1947. Decay of vorticity in isotropic turbulence. Proc. Math. Phys. Eng. Sci. 190, 534–550. https://doi.org/10.1098/rspa.1947.0095.

Batchelor, G.K., Townsend, A.A., 1948a. Decay of isotropic turbulence in the initial period. Proc. Roy. Soc. Lond. Math. Phys. Sci. 193, 539–558. http://www.jstor.org/stable/98061.

Batchelor, G.K., Townsend, A.A., 1948b. Decay of turbulence in the final period. Proc. Roy. Soc. Lond. Math. Phys. Sci. 194, 527–543. http://www.jstor.org/stable/98265.

Blackmore, T., Batten, W., Muller, G., Bahaj, A., 2013. Influence of turbulence on the drag of solid discs and turbine simulators in a water current. Exp. Fluid 55. https://doi.org/10.1007/s00348-013-1637-9.

Bossuyt, J., Howland, M., Meneveau, C., Meyers, J., 2017. Measurement of unsteady loading and power output variability in a micro wind farm model in a wind tunnel. Exp. Fluid 58. https://doi.org/10.1007/s00348-016-2278-6.

Camp, E., Cal, R., 2016. Mean kinetic energy transport and event classification in a model wind turbine array versus an array of porous disks: energy budget and octant analysis. Phys. Rev. Fluid. 1, 044404 https://doi.org/10.1103/PhysRevFluids.1.044404.

Camp, E., Cal, R., 2019. Low-dimensional representations and anisotropy of model rotor versus porous disk wind turbine arrays. Phys. Rev. Fluid. 4 https://doi.org/10.1103/PhysRevFluids.4.024610.

Cardesa, J.I., Nickels, T.B., Dawson, J.R., 2012. 2D PIV measurements in the near field of grid turbulence using stitched fields from multiple cameras. Exp. Fluid 52, 1611–1627.

Ebenhoch, R., Muro, B., Dahlberg, J.Å., Berkesten Hägglund, P., Segalini, A., 2017. A linearized numerical model of wind-farm flows. Wind Energy 20, 859–875. https://doi.org/10.1002/we.2067.

Ertunç, O., Ozyilmaz, N., Lienhart, H., Durst, F., 2010. Homogeneity of turbulence generated by static-grid structures. J. Fluid Mech. 654, 473–500. https://doi.org/10.1017/S0022112010000479.

Harrison, M., Batten, W., Myers, L., Bahaj, A., 2010. Comparison between CFD simulations and experiments for predicting the far wake of horizontal axis tidal turbines. Renew. Power Generat. IET 4, 613–627. https://doi.org/10.1049/iet-rpg.2009.0193.

Hearst, R.J., Ganapathisubramani, B., 2017. Tailoring incoming shear and turbulence profiles for lab-scale wind turbines. Wind Energy 20, 2021–2035. https://doi.org/10.1002/we.2138.

Hong, J., Toloui, M., Chamorro, L., Guala, M., Howard, K., Riley, S., Tucker, J., Sotiropoulos, F., 2014. Natural snowfall reveals large-scale flow structures in the wake of a 2.5-MW wind turbine. Nat. Commun. 5, 4216. https://doi.org/10.1038/ncomms5216.

Howland, M.F., Bossuyt, J., Martínez-Tossas, L.A., Meyers, J., Meneveau, C., 2016. Wake structure in actuator disk models of wind turbines in yaw under uniform inflow conditions. J. Renew. Sustain. Energy 8. https://doi.org/10.1063/1.4955091.

Jeong, J., Hussain, F., 1995. On the identification of a vortex. J. Fluid Mech. 285, 69–94. https://doi.org/10.1017/S0022112095000462.

Li, L., Hearst, R.J., Ferreira, M.A., Ganapathisubramani, B., 2020. The near-field of a lab-scale wind turbine in tailored turbulent shear flows. Renew. Energy 149, 735–748. https://doi.org/10.1016/j.renene.2019.12.049.

Lignarolo, L., Mehta, D., Stevens, R., Yilmaz, A., Kuik, G., Andersen, S., Meneveau, C., Ferreira, C., Ragni, D., Meyers, J., van Bussel, G., Holierhoek, J., 2016a. Validation of four LES and a vortex model against stereo-PIV measurements in the near wake of an actuator disc and a wind turbine. Renew. Energy 94, 510–523. https://doi.org/10.1016/j.renene.2016.03.070.

Lignarolo, L., Ragni, D., Ferreira, C., van Bussel, G., 2014. Kinetic energy entrainment in wind turbine and actuator disc wakes: an experimental analysis. J. Phys. Conf. 524, 012163 https://doi.org/10.1088/1742-6596/524/1/012163.

Lignarolo, L., Ragni, D., Ferreira, C., van Bussel, G., 2016b. Experimental comparison of a wind-turbine and of an actuator-disc near wake. J. Renew. Sustain. Energy 8, 023301. https://doi.org/10.1063/1.4941926.

Lumley, J.L., 1967. The Structure of Inhomogeneous Turbulent Flows.

Martínez Tossas, L., Churchfield, M., Leonardi, S., 2014. Large eddy simulations of the flow past wind turbines: actuator line and disk modeling. Wind Energy 18. https://doi.org/10.1002/we.1747.

Mazellier, N., Vassilicos, J.C., 2010. Turbulence without Richardson–Kolmogorov Cascade. Physics of Fluids 22. https://doi.org/10.1063/1.3453708.

Meyer, K.E., Pedersen, J.M., Özcan, O., 2007. A turbulent jet in crossflow analysed with proper orthogonal decomposition. J. Fluid Mech. 583, 199–227. https://doi.org/10.1017/S0022112007006143.

Myers, L., Bahaj, A., 2010. Experimental analysis of the flow field around horizontal axis tidal turbines by use of scale mesh disk rotor simulators. Ocean. Eng. 37, 218–227. https://doi.org/10.1016/j.oceaneng.2009.11.004.

Neal, D.R., Sciacchitano, A., Smith, B.L., Scarano, F., 2015. Collaborative framework for PIV uncertainty quantification: the experimental database. Meas. Sci. Technol. 26, 074003.

Neunaber, I., 2018. Stochastic investigation of the evolutoon of small-scale turbulence in the wake of a wind turbine exposed to different inflow conditions. Ph.D. thesis. Carl von Ossietzky Universität Oldenburg.

Pierella, F., Sætran, L., 2010. Effect of initial conditions on flow past grids of finite extension. In: 17th Australasian Fluid Mechanics Conference 2010.

Porté-Agel, F., Bastankhah, M., Shamsoddin, S., 2019. Wind-turbine and wind-farm flows: a review. Boundary-Layer Meteorol. https://doi.org/10.1007/s10546-019-00473-0.

Sciacchitano, A., Neal, D.R., Smith, B.L., Warner, S.O., Vlachos, P.P., Wieneke, B., Scarano, F., 2015. Collaborative framework for PIV uncertainty quantification: comparative assessment methods. Meas. Sci. Technol. 26, 074004.

Segalini, A., Dahlberg, J.Å., 2020. Blockage effects in wind farms. Wind Energy 23, 120–128. https://doi.org/10.1002/we.2413.

Sforza, P., Sheerin, P., Smorto, M., 1981. Three-dimensional wakes of simulated wind turbines. AIAA J. 19, 1101–1107. https://doi.org/10.2514/3.60049.

Siemens, 2019. The socioeconomic impacts of wind energy in the context of the energy transition. https://www.siemensgamesa.com/explore/journal/socioeconomic-report-wind-energy-2019. Online; accessed 12-December-2019.

Simisiroglou, N., Breton, S., Ivanell, S., 2017. Validation of the actuator disc approach using small-scale model wind turbines. Wind Energy Sci. 2, 587–601. https://doi.org/10.5194/wes-2-587-2017.

Sirovich, L., 1987. Turbulence and the dynamics of coherent structures. i - coherent structures. ii - symmetries and transformations. iii - dynamics and scaling. Q. Appl. Math. 45 https://doi.org/10.1090/qam/910463.

Skeide, A.K., Bardal, L.M., Oggiano, L., Hearst, R.J., 2020. The significant impact of ribs and small-scale roughness on cylinder drag crisis. J. Wind Eng. Ind. Aerod. 202 https://doi.org/10.1016/j.jweia.2020.104192.

Smith, C., Barthelmie, R., Pryor, S., 2013. In situ observations of the influence of large onshore wind farm on near-surface temperature, turbulence intensity, and wind speed profiles. Environ. Res. Lett. 8 https://doi.org/10.1088/1748-9326/8/3/034006.

Stevens, R.J.A.M., Gayme, D., Meneveau, C., 2014. Large eddy simulation studies of the effects of alignment and wind farm length. J. Renew. Sustain. Energy 6. https://doi.org/10.1063/1.4869568.

Stevens, R.J.A.M., Meneveau, C., 2014. Temporal structure of aggregate power fluctuations in large-eddy simulations of extended wind-farms. J. Renew. Sustain. Energy 6. https://doi.org/10.1063/1.4885114.

Stevens, R.J.A.M., Meneveau, C., 2017. Flow structure and turbulence in wind farms. Annu. Rev. Fluid Mech. 49 https://doi.org/10.1146/annurev-fluid-010816-060206.

Sunada, S., Sakaguchi, A., Kawachi, K., 1997. Airfoil section characteristics at a low Reynolds number. J. Fluid Eng. 119, 129–135. https://doi.org/10.1115/1.2819098.

Theunissen, R., Housley, P., Allen, C., Carey, C., 2015. Experimental verification of computational predictions in power generation variation with layout of offshore wind farms. Wind Energy 18. https://doi.org/10.1002/we.1788.

Theunissen, R., Worboys, R., 2018. Near-wake observations behind azimuthally perforated disks with varying hole layout and porosity in smooth airstreams at high Reynolds numbers. J. Fluid Eng. 141 https://doi.org/10.1115/1.4041614.

van der Kindere, J., Ganapathisubramani, B., 2018. Effect of length of two-dimensional obstacles on characteristics of separation and reattachment. J. Wind Eng. Ind. Aerod. 178, 38–48. https://doi.org/10.1016/j.jweia.2018.04.018.

Veers, P., Dykes, K., Lantz, E., Barth, S., Bottasso, C., Carlson, O., Clifton, A., Green, J., Green, P., Holttinen, H., Laird, D., Lehtomäki, V., Lundquist, J., Manwell, J., Marquis, M., Meneveau, C., Moriarty, P., Munduate, X., Muskulus, M., Wiser, R., 2019. Grand challenges in the science of wind energy. Science eaau2027. https://doi.org/10.1126/science.aau2027.

Wieneke, B., 2015. PIV uncertainty quantification from correlation statistics. Meas. Sci. Technol. 26, 074002.

Wu, Y., Porté-Agel, F., 2011. Large-eddy simulation of wind-turbine wakes: evaluation of turbine parametrisations. Boundary-Layer Meteorol. 138 https://doi.org/10.1007/s10546-010-9569-x.

Wu, Y., Porté-Agel, F., 2012. Atmospheric turbulence effects on wind-turbine wakes: an LES study. Energies 5, 5340–5362. https://doi.org/10.3390/en5125340.

Zhan, L., Letizia, S., Iungo, G., 2019. LiDAR measurements for an onshore wind farm: wake variability for different incoming wind speeds and atmospheric stability regimes. Wind Energy. https://doi.org/10.1002/we.2430.

Zhan, L., Letizia, S., Iungo, G., 2020. Wind LiDAR measurements of wind turbine wakes evolving over flat and complex terrains: ensemble statistics of the velocity field. J. Phys. Conf. 1452 https://doi.org/10.1088/1742-6596/1452/1/012077.

Article IV

The flow in the induction and entrance regions of lab-scale wind farms

Magnus K. Vinnes, Nicholas A. Worth, Antonio Segalini, R. Jason Hearst

Under consideration for publication in:
Wind Energy

This paper is under consideration for publication and is therefore not included.